DAYEM BRIDGE BASED NANOSQUID FOR HIGH SENSITIVE NANOSCALE APPLICATIONS

A thesis Submitted to

DEPARTMENT OF PHYSICS
UNIVERSITY OF NAPLES 'FEDERICO II', NAPLES, ITALY
FOR THE DEGREE OF
DOCTOR OF PHILOSOPHY
IN
"NOVEL TECHNOLOGIES FOR MATERIALS, SENSORS AND IMAGING"

By

PRAVIN SOPANRAO WALKE

November 2010

PhD Coordinator: Prof. Antonello Andreone

UNIVERSITY OF NAPLES 'FEDERICO II'

Department of Physical Science

International PhD Program on Novel Technologies

for Materials, Sensors and Imaging

(XXIII Cycle)

Title: **Dayem Bridge Based NanoSQUID for High Sensitive Nanoscale Applications**

Author: **Pravin Sopanrao Walke**

Department: **Physical Sciences**

Degree: **Ph.D.**

The research activities described in this thesis are performed at *Istituto di Cibernetica 'E.Caianiello'* (ICIB) of *Consiglio Nazionale delle Ricerche* (CNR), Pozzuoli, (Napoli) Italy.

Research Guides

Dr. Carmine Granata

Dr. Emanuela Esposito

Doctorate Coordinator

Prof. Antonello Andreone

Date: **30th November 2010**

Dedicated to My Parents Papa and Aai

To raise new questions, new possibilities, to regard old problems from a new angle, require creative imagination and marks real advance in science.

..... Albert Einstein

Dream is not what you see in sleep, is the thing which does not let you sleep.

..... A.P.J. Abdul Kalam

Acknowledgements

I have spent an exciting and pleasant three years at ICIB-CNR, mostly due to the amazing people that I had the good fortune to associate with. There are so many people, whose support, encouragement and inspiration are very much obligatory to accomplish major achievements in life.

I am grateful to my advisor Dr. Carmine Granata for his advice, encouragement, and support over these years. His enthusiasm for new ideas is infectious that has helped to widen my interest in physics; timely criticism and continual guidance have lead me to convey my dream to reality. I have enjoyed learning from him and very much honored to work under his esteemed guidance. He is very patient, understanding and above all is very helpful to others; this naturally makes him my Idol.

In this respect, I must mention that I would also like to offer my sincere gratitude to my second advisor Dr. Emanuela Esposito for all her help, support, suggestion and advice during the course of this study especially electron beam lithography technique.

I wish to thank Dr. Maurizio Russo, the Director, ICIB-CNR for giving me an opportunity to work and use all infrastructural facilities of the Institute. I am also grateful to Prof. Giancarlo Abbate, Prof. Antonello Andreone former and present Chairman of TIMSI PhD program for their constant encouragement and allowing me to use all the available facilities in the divisions.

It gives me great pleasure to thank Dr. Antonio Vettoliere and Dr. Roberto Russo for their fruitful suggestions, encouragements and help in accomplishing such difficult experiments. Special thanks are to Dr. Ciro Nappi for his helpful and valuable guidance to make superconductivity research platform in the beginning of this thesis work as well as to perform theoretical and simulation study.

My heartfelt gratitudes are to Dr. Roberto Cristiano, Dr. E. Sarnelli, Dr. Dino Ruggiero, Dr. Misha Lisitskiy, Dr. C. Camerlingo for their support and help. I am highly indebted to my former research supervisors Dr. K. Vijayamohanan, Dr. I. S. Mulla, Prof. S. V. Bhoraskar, Dr. Qiquan Qiao, Dr. Sanjay Chakane for their constant encouragements, guidance and support that stimulate me to PhD study. I wish to extend my sincere gratitude to Dr. Niranjan Ramgir, Dr. Datta Late, Dr. Bhaskar Sathe and Dr. Bhalachandra Kakade for their love, constant encouragement and timely help. I also take this opportunity to thank Mr. Guido Celentano, (Secretary, Physics Department) for his help concerning not only administrative, bureaucratic documentation but also personal assistance during my stay and study in Napoli. I would like to

thank, Dr. Maharajan for his kind personal help, constant support and guidance. Further, CNR is gratefully acknowledged for the financial support.

I wish to thank all my colleagues in ICIB-CNR, Dr. Alessandro Bruno, Dr. Alessandro Casaburi, Dr. Maria Adamo, Dr. Sara Rombetto. I want to share this great moment in my life with all my friends in the world, without their help and support this work would surely not have been possible; Sanjay, Dhanraj, Amar, Mariyappan, Dasharath and Ravi my home mates, who have helped me to maintain stability in my last year's life; Naresh and friends, my study, travel and spiritual mate, who has inspired and supported me throughout our studies and spare time in Napoli; Atul, Priya, Somu, Ankita, Ankush, Raju and Chaitali are few among them.

I find no words to express my feelings for my parents, whose moral support, love and constant encouragements have helped me to complete this journey. Their patience and sacrifice are always a main source of my inspiration and will remain throughout my life, motivating me to pursue still higher goals. I thank my elder brother 'Santosh Bhau', *wahini* 'Rekha', my sister 'Poonam' and *daji* 'Sandeep', who always encouraged me during my doctoral course. The presence of the little angels 'Samruddhi' (Sonu) and Sayi was always refreshing, making me feel relax and comfortable. I wish to extend my sincere gratitude to all my relatives for their blessings.

Finally, heartfelt thanks to all of them who are directly and indirectly helped me to reach this stage.

It would be great satisfaction, if my efforts are ever to be of any use for the society welfare and the improvement in science and technology.

Pravin S. Walke

Contents

Useful Constants **i**
Introduction 1

Chapter -1: Josephson Effects and DC-SQUID's **(3-31)**
1.1 Josephson Effect:
1.1.1. Superconducting Tunnel Effect 4
1.1.2 Josephson Effect 8
1.1.3 Resistively shunted model 14
1.2 DC-SQUID:
1.2.1 Flux quantization in a superconducting ring 18
1.2.2 DC- SQUID 20
1.2.3 Thermal Noise in DC-SQUID 26
1.2.4 Low frequency noise in DC-SQUID 27
References 30

Chapter -2: Dayem Bridge Based SQUID **(32-59)**
2.1 Introduction 33
2.2 Josephson Dayem Bridges: 36
2.2.1 Fabrication Aspect and preparation methods 37
2.2.2 Physics of Dayem Bridges 38
2.3 SQUID Based on Nb Dayem Bridges: 42
$(I_C - \Phi)$ characteristics as function of L / ξ ratio 43
2.4 Techniques to attach nano-particles to nano-SQUID 44
2.5 Spin Sensitivity Simulation of nanoSQUID
2.5.1 Simulation Scheme 45
2.5.2 Magnetic flux distribution 49
2.5.3 Spin sensitivity 52
References 55

Chapter -3: Nanoscale DC-SQUID Fabrication **(60-84)**
3.1 General E-Beam lithography system 60
3.1.1 Technical EBL Set up 61
3.1.2 Electron interaction with matter 65
3.1.3 Resolution Capability 67

3.1.4 Proximity effect 68
3.2 Design norms and Circuit layout 70
3.3 Fabrication of Bilayer Device 73
3.3.1 DC-Magnetron Sputtering 74
3.3.2 Resist deposition and E-beam patterning 76
3.3.3 Liff off and Reactive ion etching 77
3.3.4 Integration of coil and wiring 78
3.3.5 Passivation 81
3.4 Fabrication of Single layer device 81
References 84

Chapter -4: Characterization of NanoSQUID and Preliminary Nanoparticle Magnetization Measurements (85-111)
4.1 Characterization of SQUID 86
4.2 Comparison between Hysteretic and Non-Hysteretic SQUID 89
4.3 Experimental Performances:
4.3.1 Non-hysteretic SQUID 90
- Current voltage measurements 90
- Responsivity i.e. V-Φ and I- Φ characteristics 91
- Noise Measurement 93

4.3.2 Hysteretic SQUID 96
- Current voltage measurements 96
- Current Measurement techniques 98
- Switching current probability P (I) distribution 100
- Responsivity i.e. I- Φ characteristics 101

4.4 Preliminary iron oxide nanoparticle magnetization measurements 105
Iron oxide nanoparticle magnetization measurements 107
References 110

Conclusions 112
List of Publications 114
Abbreviations 116

Useful Constants

$k_B = 8.617 \times 10^{-5}\ eV / K$	**Boltzmann's constant**
$\Phi_0 = \frac{h}{2e} = 2.07 \times 10^{-15}\ Wb$	**Flux quantum**
$h = 4.125 \times 10^{-15}\ eV.s$	**Plank's constant**
$\hbar = \frac{h}{2\pi} = 6.582 \times 10^{-16}\ eV.s$	
$\mu_0 = 4\pi \times 10^{-7}\ N / A^2$	**Magnetic vacuum permeability**
$\mu_B = 9.27 \times 10^{-24} J / T$	**Bhor Magneton**

Introduction

Superconducting quantum interference devices (SQUIDs) are highly sensitive magnetometers suitable for measuring magnetic signals from micron and nanometer sized particles. SQUID devices are being used to detect and measure a vast range of different physical parameters such as magnetic field, magnetic field gradient, current, voltage or displacement which can be converted into a magnetic flux. Since their discovery, SQUIDs have been applied in several applications, ranging from the detection of human brainwaves to the observation of single atomic spin flips. Among the several applications of the SQUID, in the recent years, many efforts have been devoted to the detection of the magnetic moment of micrometric size particles and the single atomic spin-flip. For this application, the device sensitivity scales as the side length of the SQUID loop, therefore in the recent years there is a growing interest in the development of SQUIDs having a sub-micrometric loop diameter (100-200nm). In such a way, it has been possible to reach a spectral density of magnetic moment noise as low as few $\mu_B/\mathrm{Hz}^{1/2}$ (μ_B is the Bohr magneton) making such nano-sensors ideal for local magnetic measurements.

A nano-SQUID sensor requires Josephson junctions having a deep sub-micron size. Due to the limits of the fabrication process, tunnel Josephson junctions cannot be employed in such nano-SQUIDs. A good alternative to more reliable tunnel type junctions is the Dayem nano-bridges (nano-constriction of a superconducting film) fabricated using Electron Beam Lithography (EBL) or Focused Ion Beam (FIB) having a length and a width of less than one hundred nanometers. Furthermore, with respect to the tunnel junctions, Dayem Bridges are insensitive to the magnetic field applied in the plane of the SQUID loop. The lack of sensitivity to a high field applied in the SQUID plane is a essential for the measurement of the nanoparticles magnetization.

The nanoSQUID having a better sensitivity in term of Bohr magnetons, gives the opportunity to investigate the physical properties of objects having a submicron size as the magnetization reversal measurement of small cluster of atoms or nanoparticles. This thesis focuses on nanoSQUID magnetic sensitivity improvement and their

employment towards magnetization study of magnetic nanoparticles. In this work, we have designed, fabricated and characterized both the hysteretic and non-hysteretic nanoSQUIDs for magnetization investigation of nanoparticles. Furthermore preliminary measurements of iron oxide nanoparticle magnetization have been made.

The thesis is organized in the following chapters.

In the first chapter, the superconducting tunneling and two macroscopic quantum effects, such as flux quantization in a superconductive ring and Josephson effects are briefly introduced. The SQUID working principles and the physical theory concerning noise is also described.

The second chapter is devoted to requirement of nanoSQUID and its performance towards detection of small spin cluster. The short overview on physics of Dayem Bridges and properties of SQUID based on Nb Dayem Bridges is presented. The spin sensitivity simulation results are reported in order to understand the spin sensitivity performance of nano-SQUID as function of its position inside SQUID loop.

In the third chapter, the details regarding electron beam lithography techniques and its operation in fabrication of device is presented. Also other techniques involved in the fabrication like the DC-magnetron sputtering for thin film deposition; lift off, reactive ion etching process are briefly described. Our fabrication process of a single niobium layer device and niobium-aluminum bilayer devices are reported.

In the last chapter, the experimental performances of both non-hysteretic and hysteretic nanoSQUIDs are described, in order to employ it for nanoparticle magnetization detection. The preliminary measurements of iron oxide nanoparticles magnetization using hysteretic nanoSQUID have described to attest the capability of our devices.

CHAPTER 1

Josephson Effects and DC-SQUID

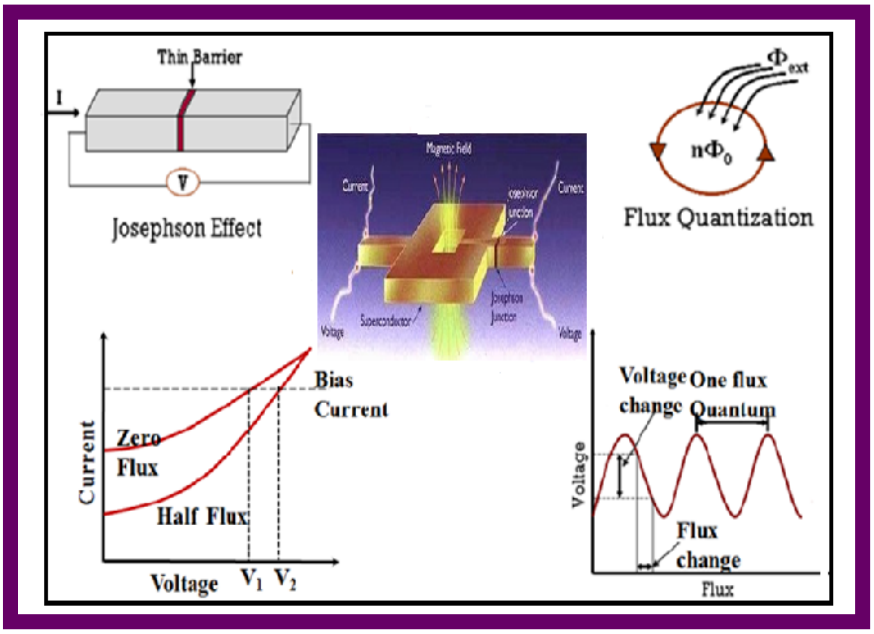

This chapter presents physical phenomena which govern the operation of **S**uperconducting **QU**antum **I**nterference **D**evices such as flux quantization in a superconductive ring and the Josephson Effect. This chapter has been presented in two separate sections for better insight. In the first section, short description of superconducting tunnel effects and Josephson effects has been reported. Subsequently RSJ model has been introduced briefly. In the Second section, we particularly emphasized on working principle of SQUIDs and physical theory concerning thermal and low frequency noise describing the source of noise.

1.1 General Aspects and Josephson Effects:

Superconductors are materials that exhibit zero resistance behavior when cooled below a certain temperature near absolute zero. The English physicist Brian D. Josephson predicted the flow of electric current between two pieces of superconducting material separated by a thin layer of insulating material in 1962 on the basis of the BCS theory of superconductivity [1-5].

BCS theory states that superconductivity is outcome of the correlated motion of electrons in the superconducting solid. Such correlation is the formation of pairs of electrons called Cooper pairs. Under certain circumstances, these Cooper pairs transfer from one to the other superconductor across the thin insulating barrier. Such motion of pairs of electrons or copper pair constitutes the Josephson current, and the process by which the pairs cross the insulating layer is called Josephson tunneling. The presence of magnetic fields near the superconductors influences the Josephson Effect, allowing it to be used to measure very weak magnetic fields. In this section, we describe superconducting tunnel effect, Josephson effects and resistively shunted model.

1.1.1. Superconducting Tunnel Effect:

There are many conflictions in quantum mechanical phenomena's; perhaps the tunneling is the most prominent among them. In 1957, Esaki's invention of tunnel diode was conveyed attention towards tunneling effect [6]. The initial measurements on superconducting tunneling were performed by Giaever in 1960s [7, 8, 9] and Nicol et al. [10] when they measured the current-voltage characteristics of a normal metal-insulator-superconductor (SIS) sandwich. They observed that as soon as one of the metals becomes superconductive, the junction resistance is drastically increased. They elucidated the result by taking into account the superconducting energy gap which reduced the electron flow by not accepting electrons with small excitation energies. It was a simple experiment giving a large amount of the information. The following different cases are shortly described by considering energy diagrams and current-voltage (I-V) characteristics.

Energy Diagram and I-V Characteristics of Superconducting Junctions:

(A) Normal Metal-Insulator-Superconductor Junctions (N-I-S):

The energy diagram of a normal metal-superconductor separated by a thin insulating barrier called junction is shown in fig.1.1 (like semiconductor representation). At absolute zero temperature all the states are filled up to E_F-Δ and no filled states above the gap. At finite temperature there are electrons above the gap and holes below the gap.

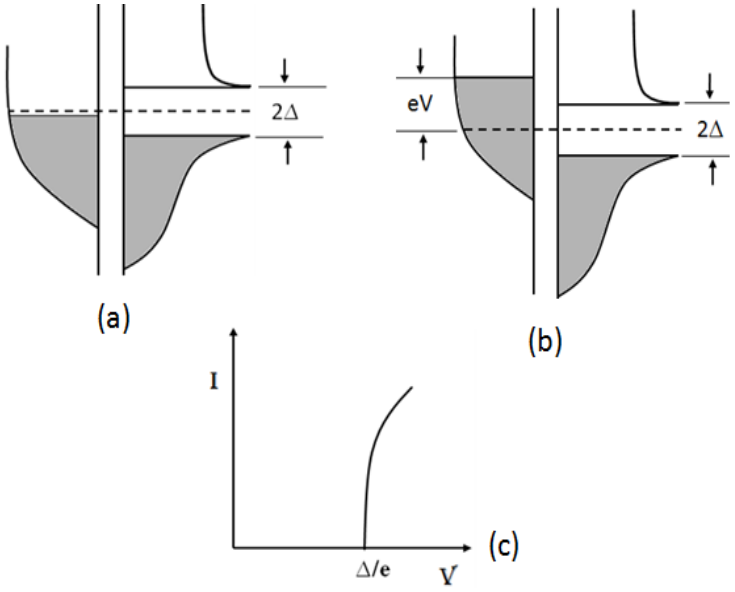

Fig.1.1 The energy diagram of an N-I-S junction in the semiconductor representation; (a) V=0, (b) V>Δ/e, (c) The I-V characteristics at T=0 [1].

The Fermi energies must match at thermal equilibrium. If voltage V< Δ/e is applied, due to absence of empty state on the left, current cannot flow as shown in fig. 1.1(a). At V=Δ/e there is sudden rise in current. There are two main reasons for the sudden rise in current; one the electron may tunnel from left to right and second the density of the electrons is large. The empty states become available at voltage V>Δ/e for tunneling as shown in fig.1.1(b), so the current increases as result of tunneling shown in fig.1.1(c).

For finite temperature, a very small voltage is sufficient for the current to start flow but any appreciable rise in current must again occur around V=Δ/e.

(B) Superconductor-Insulator-Superconductor Junctions(S-I-S):

The fig. 1.2 shows the energy diagram for $T=0^0K$ of two identical superconductors separated by thin insulating barrier.

In thermal equilibrium, all energy levels are filled up to E_F-Δ as shown in (fig.1.2(a)). Hence there is no current flow. Even after applying voltage V< 2Δ/e (fig.1.2(b)), the electron below the gap on the left have no access to empty state on right. So, current cannot flow. After applying voltage V=2Δ/e, current flows as showed by the corresponding I-V characteristic in fig.1.2(c).

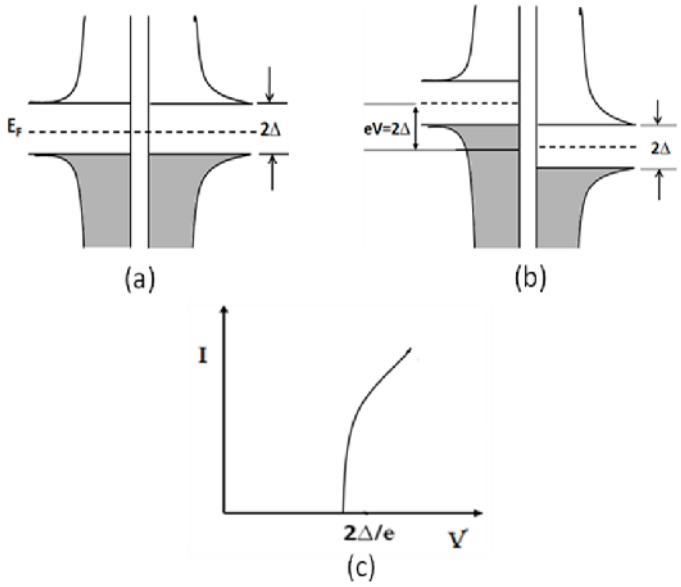

Fig. 1.2 The energy diagram of an S-I-S junction; (a) V=0, (b) V=2Δ/e, (c) The I-V characteristics at T=0 [1].

(C) Superconductor-Insulator-Superconductor Junction (S_1-I-S_2):

Similar to previously discussed case of the identical superconductors at T= 0^{O}K, no current flow until the applied voltage $V = |\Delta_1 + \Delta_2| / e$ is sufficiently large to bring the bottom of the gap on the left line with the top of the gap on the right as shown in fig.1.3(a). A current flow has been shown by the corresponding I-V characteristic in fig.1.3(b).

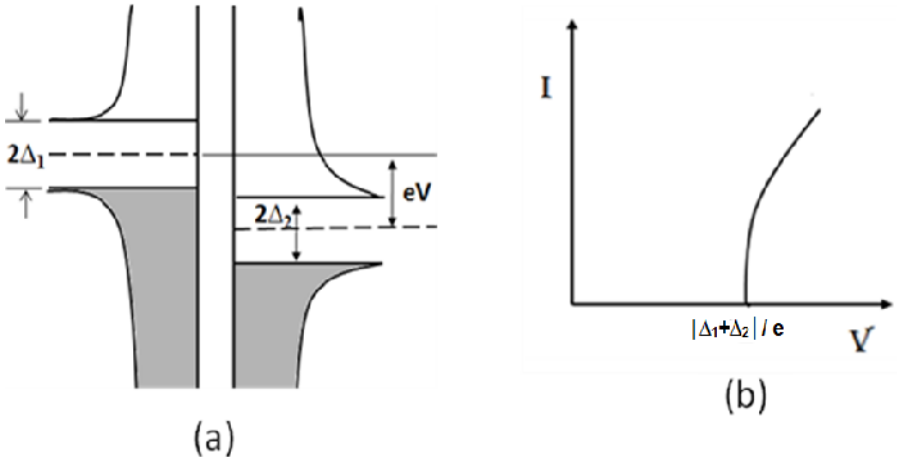

Fig. 1.3 Energy diagram and I-V characteristics of an S_1-I-S_2 junction at T=0 [1].

At finite temperature and at thermal equilibrium, the normal electron states above the large gap are empty but there are some thermally excited normal electrons in

the similar gap semiconductor as shown in fig.1.4(a). By applying a voltage, suddenly the current will start to flow and will increase with increasing voltage upto $V = |\Delta_1 - \Delta_2|/e$ as shown in fig.1.4(e). The energy diagram for this case is shown in fig.1.4(b). At this stage all the electrons above the gap on the left can tunnel across into empty state to right. Even by further increasing voltage, the number of the electrons capable to tunnel across is still the same but they face a smaller density of the states, as shown in fig.1.4(c) hence the current decreases until $V = |\Delta_1 + \Delta_2|/e$, at this point as shown fig 1.4(d) electrons from below the gap on the left gain access to empty states on the right and current increases. Thus the current voltage characteristics of shown in fig.1.4(e) exhibits a negative resistance in the region

$$\frac{|\Delta_1 - \Delta_2|}{e} < V < \frac{|\Delta_1 + \Delta_2|}{e} \qquad (1.1)$$

Nicol et al. [10] and Giaever [9] have reported the appearance of a negative resistance. A very convincing characteristic have presented by the later authors for Al-Al_2O_3-Pb junction is shown in fig.1.5.

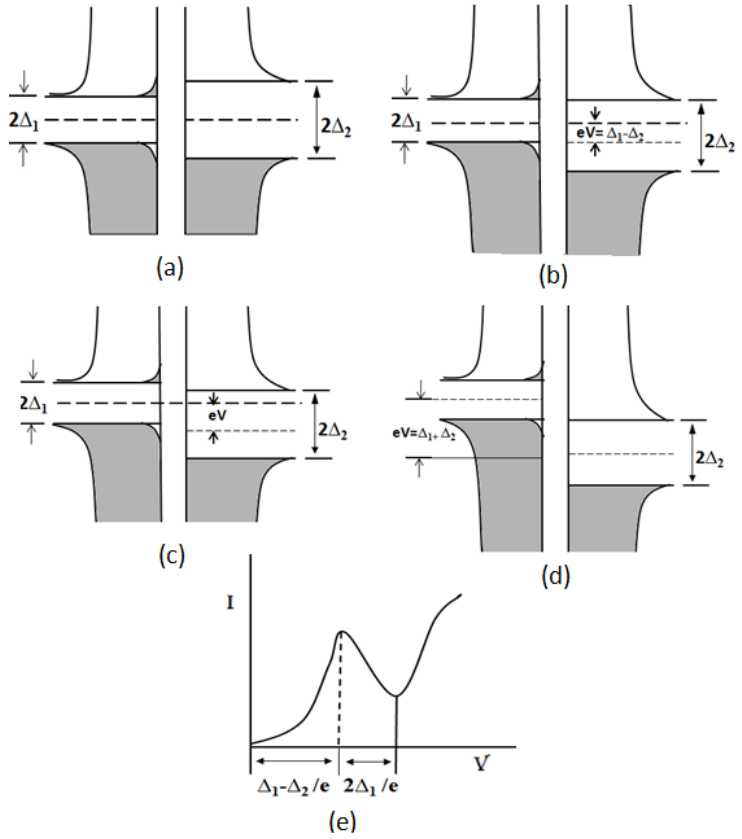

Fig. 1.4 The energy diagram and I-V characteristics of an S_1-I-S_2 junction at finite temperature; (a) V=0, (b) V= $(\Delta_1-\Delta_2)/e$, (c) $(\Delta_1-\Delta_2)/e < V < (\Delta_1+\Delta_2)/e$, (d) V= $(\Delta_1+\Delta_2)/e$, (e) the I-V characteristics [1].

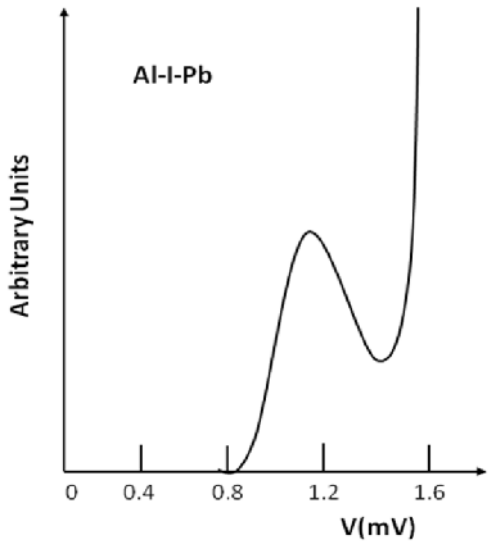

Fig.1.5 The I-V characteristic of an Al-I-Pb junction, both Al and Pb superconducting [10].

1.1.2 Josephson Effect:

In 1962, B. Josephson was published a theoretical paper [11] predicting the existence of two fascinating effects into superconducting tunnel junctions. The basic idea of the first effect was that a tunnel junction should be able to sustain a zero-voltage current (supercurrent). Secondly, the critical value of supercurrent was depending on the external magnetic field in a very unusual way. If the current exceeds its critical value, which is a characteristic of a particular junction, the junction begins to generate high-frequency electromagnetic waves. This is the AC Josephson effect.

Both effects were thoroughly verified by experiments published in ref. [11-13]. Moreover, soon after it became clear that the Josephson effects exist not only in tunnel junctions, but also in other kind of the junctions so-called dayem bridges, that is, short constriction of superconducting film where the critical current is substantially suppressed [14,15].

a) The DC Josephson Effect:

A sufficiently small current can pass through a weak link (Josephson junction) without dissipation. In other words, small amount of current can pass through the weak link without generating voltage across the junction.

If two superconducting regions are kept totally isolated from each other, the phases of the electron-pairs in the two regions are uncorrelated. However, if the two regions are brought close enough so that electron-pairs may tunnel across the

barrier, the two electron-pair wave functions will become coupled. This means a supercurrent can flow in spite of the presence of the tunnel barrier as predicted by B.D. Josephson and this phenomenon is known as Josephson tunneling [11].

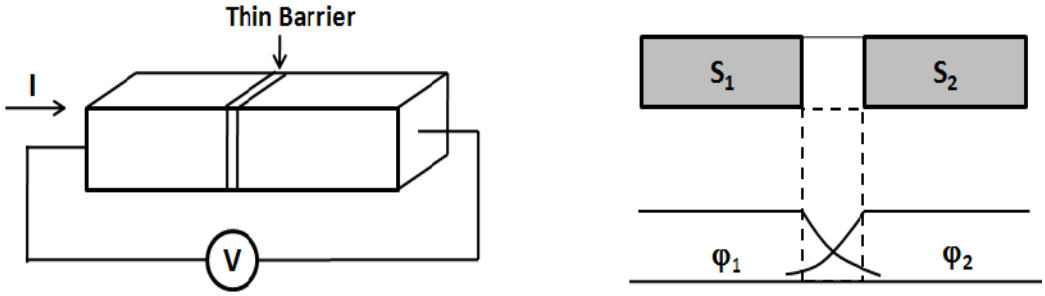

Figure 1.6: A Josephson junction may be represented by superconductor's S_1 and S_2 interrupted by a thin insulating layer. The applied current I controls the difference $\varphi = \varphi_1 - \varphi_2$ between the phases of the complex order parameters of the two superconductors according to the dc Josephson's relation (eq. 1.2).

Thus, a Josephson junction is a superconductor interrupted by a thin insulating layer, where superconductive properties are weakened, as shown in figure 1.6. In the Josephson formulation, the phase difference between two superconductors is a well defined physical quantity and it obeys to the relation (dc Josephson effect)

$$I = I_c \sin\varphi \qquad (1.2)$$

Equation 1.2 describes the relationship between the supercurrent I passing across the junction, the difference between the phases φ_1 and φ_2 macroscopic wavefunction associated to the superconducting electrodes and the critical current, I_C i.e. the maximum current capacity of the junction without developing any voltage across it.

A Simple Quantum Mechanical Approach: According to Feynman [16], the time evolution of a quantum-mechanical system is described by a wavefunction $\psi(t)$ throughout the solution of the Schrodinger equation:

$$i\hbar\frac{\partial\Psi}{\partial t} = H\Psi \qquad (1.3)$$

where H is the Hamilton operator.

If the system is allowed only discrete states ψ_α where α is a series of indices each characterizing a given state, its wavefunction can be expanded in a series

$$\Psi(t) = \sum_\alpha C_\alpha(t)\psi_\alpha \tag{1.4}$$

Substitution of (1.4) in (1.3) gives

$$i\hbar \frac{\partial \sum_\alpha C_\alpha(t)\psi_\alpha}{\partial t} = \sum_\alpha H\, C_\alpha(t)\psi_\alpha \tag{1.5}$$

Multiplying both side by ψ_β

$$i\hbar \frac{\partial \sum_\alpha C_\alpha(t)\psi_\alpha\psi_\beta}{\partial t} = \sum_\beta (H\, C_\alpha(t)\psi_\alpha)\psi_\beta \tag{1.6}$$

being $\psi_\alpha \psi_\beta = \delta_{\alpha\beta}$

So, equation becomes $$i\hbar \frac{dC_\beta}{dt} = \sum_\alpha C_\alpha(t)\, H_{\beta\alpha} \tag{1.7}$$

Here $H_{\alpha\beta} = \left\langle H\psi_\alpha \middle| \psi_\beta \right\rangle = \int H\psi_\alpha \psi_\beta^* \, dV = \int \psi_\beta^* \, \bar{H}\psi_\alpha dV$

The function $C_\alpha(t)$ represents the amplitude of the state ψ_α and $|C_\alpha|^2$ gives the probability of finding the system in the state ψ_α.

If the current flowing through the junction exceeds the value of critical current, voltage appears across the junction as a result of Josephson tunneling. Following Feynman [16], a system of superconducting electrons or Cooper pairs are considered as a two-level quantum-mechanical system. We suppose that an electron pair with charge 2e can occupy either level 1 or level 2. Then its energy will be either H11 or H22, respectively, where H11 = eV and H22 = -eV. The transition from level 1 to level 2 is governed by the matrix element H12 = H21= K. Then (1.7) becomes

$$\begin{aligned} i\hbar \frac{dC_1}{dt} &= eV\, C_1(t) + KC_2(t) \\ i\hbar \frac{dC_2}{dt} &= KC_1(t) - eV\, C_2(t) \end{aligned} \tag{1.8(a))}$$

Here C_1 is the amplitude of the pair state at level 1 and $|C_1|^2$ is normalized in such a way that $|C_1|^2 = n_S$, where n_S is the superconducting electron density in the junction electrodes. For the sake of simplicity, we assume that both electrodes are made of the same material. Expressing the amplitudes C_1 and C_2 as

$$C_1 = \sqrt{n_s}\, e^{i\varphi_1} \qquad and \qquad C_2 = \sqrt{n_s}\, e^{i\varphi_2} \qquad \text{(1.8 (b))}$$

Substituting these in (1.8(a)), and separating real and imaginary parts, we obtain

$$\begin{aligned} \frac{dn_s}{dt} &= \frac{2Kn_s}{\hbar}\sin(\varphi) && (a) \\ \frac{d\varphi_1}{dt} &= \frac{-K}{\hbar}\cos(\varphi) - \frac{eV}{\hbar} && (b) \\ \frac{d\varphi_2}{dt} &= \frac{-K}{\hbar}\cos(\varphi) + \frac{eV}{\hbar} && (c) \end{aligned} \qquad (1.9)$$

where $\varphi = \varphi_1 - \varphi_2$.

The current through the tunnel junction is proportional to dn_S / dt. In fact, as soon as the current is switched on, the superconducting electron density starts to vary at the rate dn_S / dt thereby giving rise to a current $I_C = dn_S / dt$. From (1.9) we can obtain the equation (1.2) for the DC Josephson effect (where $I_C = \frac{2Kn_S}{\hbar}$).

b) The AC Josephson Effect:

The AC Josephson effect predicts the relationship between voltage across Josephson junction and phase difference. This second fundamental Josephson relation can be obtained by subtracting the equation 1.9 (c) and 1.9 (b) as follows,

$$2eV = \hbar\frac{\partial\varphi}{\partial t} \qquad (1.10)$$

where $\varphi = \varphi_2 - \varphi_1$

If a constant voltage V is maintained across the junction, then

$$V = \frac{\hbar}{2e}\frac{\partial\varphi}{\partial t} \;\rightarrow\; \varphi(t) = \frac{2e}{\hbar}Vt + const. \qquad (1.11)$$

Substituting the equation 1.11 in the 1.2, we obtain

$$I = I_C \sin\left(\omega t + const.\right) \tag{1.12}$$

where $\omega = \frac{2e}{\hbar} V$. For a 1μV, frequency ω = 2e/*h* ≈ 483.6 MHz is obtained and the junction behaves as a frequency-voltage transducer.

c) Current- Voltage Characteristics and I_C Vs External Magnetic Flux:

As the current across the junction is increased from zero, for $I<I_C$ the phase difference has the value constant in time, so that the voltage across the junction remains zero (V=0). When the current exceeds the critical current $I>I_C$, the phase difference evolves according equation 1.11 and there is a voltage (V≠0) across the junction.

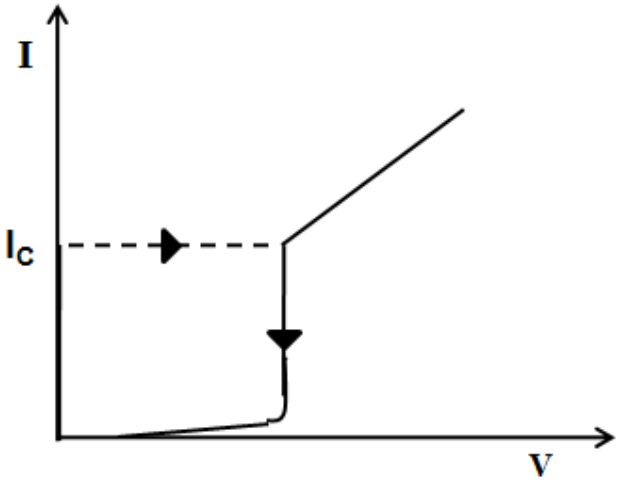

Figure 1.7: I-V characteristic of hysteretic junction.

The I-V curve shows that if the junction is biased with a constant current source, lower than the critical current I_C, there will be no voltage drop across the junction, although the passage of the current through the device will introduce a phase difference across it. When the bias current exceeds I_C, a voltage will appear and the phase differences become time-dependent.

Just one year after the discovery of Josephson tunneling, Anderson and Rowell [17-18] made the first observation of the DC Josephson effect, using a thin-film Sn-SnOx-Pb junction cooled in liquid helium [19]. They showed that the current voltage characteristic of a Josephson junction, due to the capacitance associated with the structure, was strongly hysteretic (see figure 1.7). This hysteresis can be eliminated by shunting the Josephson junction with a normal ohmic resistor R. The detail of resistively shunted junction (RSJ) model has been discussed subsequently in this

chapter. For DC-SQUID realization, one uses typically resistively shunted junctions with a single valued current voltage characteristic.

The dependence of the critical current on the applied magnetic field is shown in figure 1.8. Rowell predicted [18] that a magnetic field B applied to the junction caused a modulation of the critical current according to the relation

$$I_{\max} = I_c \left| \frac{\sin(\pi\Phi / \Phi_0)}{\pi\Phi / \Phi_0} \right| \qquad (1.13)$$

The period of oscillations is given by the field required to generate one flux quantum. Thus, the maxima critical current occur at $\Phi/\Phi_0 = 0, \pm1, \pm2 \ldots \pm n$.

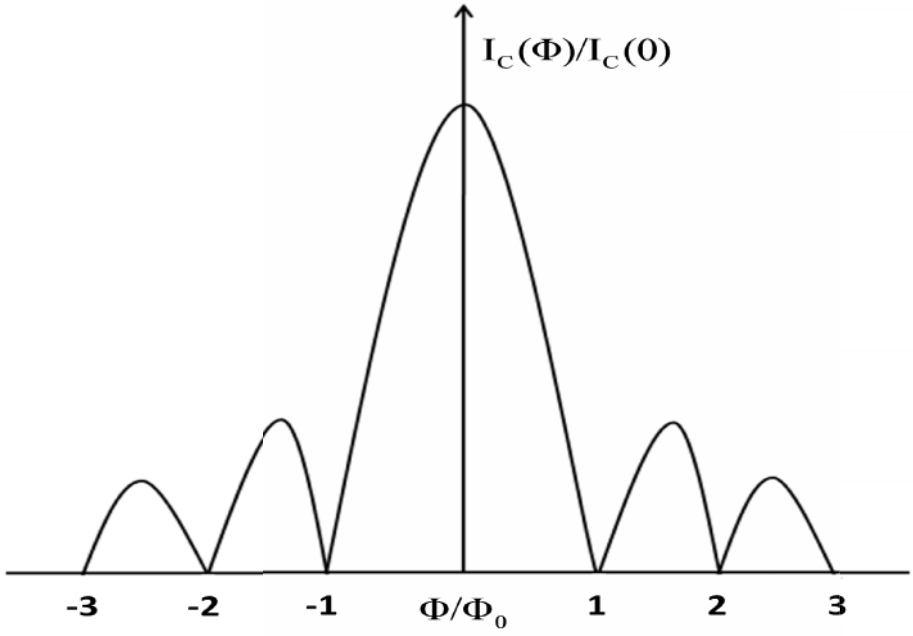

Figure 1.8 Josephson current vs. magnetic field applied parallel to the plane of the junction showing Interference effects.

Thus, the critical current becomes zero for Φ equal to integer units of the flux quantum $\Phi_0 \approx 2.07 \times 10^{-15}$ Wb. The observation of this Fraunhofer-like result, which is analogous to the diffraction of monocromatic coherent light passing through a slit, is a validation of the sinusoidal current phase relation. The junction is completely unstable at magnetic flux Φ equal to integer units of the flux quantum Φ_0. On the other hand it is more stable at half integral multiple of flux enclosed in the junction.

1.1.4 Resistively Shunted Model:

In some applications, the junctions operating schemes are based on resistively shunted junctions to eliminate hysteresis on its I-V characteristics. A high-quality tunnel junction has a hysteretic current–voltage (I–V) characteristic by increasing the bias current from zero, the voltage switches abruptly to a nonzero value when bias current I exceed critical current I_0, but returns to zero only when I is reduced to a value much less than I_0.

The resistively and capacitively shunted junction model (RCSJ) leads directly to the resistively and capacitively shunted the Josephson junction [20] in which the Josephson junction, a normal resistance (R) and capacitance (C) are connected in parallel as shown in fig. 1.9(a). The resistance R builds in dissipation within the finite voltage regime, without affecting the lossless dc regime, while C reflects the geometric shunting capacitance between the two electrodes, not the capacitance of the electrodes to "ground [21].

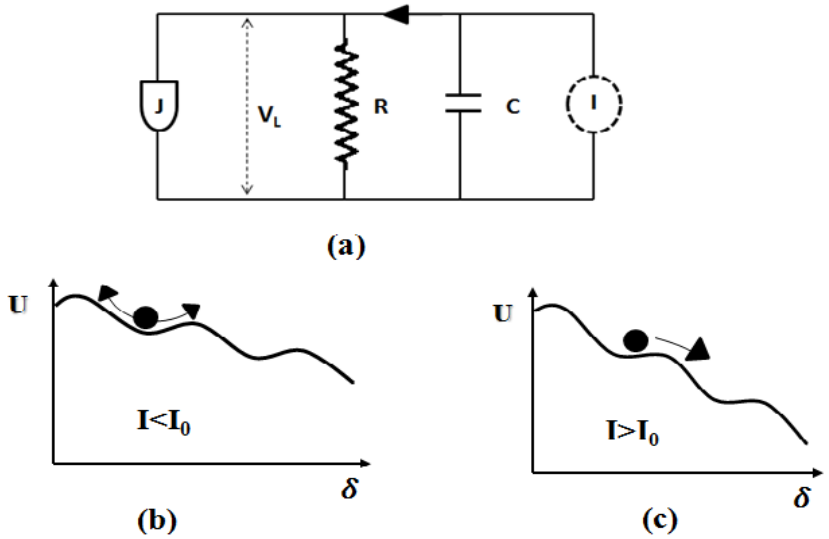

Fig. 1.9 (a) Equivalent circuit of the resistively and capacitively shunted Josephson junction; (b) and (c) show the tilted washboard potential for $I < I_0$ and $I > I_0$.

The time dependence of the phase φ in the presence of an externally supplied bias current can be derived by equating the bias current I to the total junction current from the three parallel channels. Using Kirchhoff's law we obtain:

$$I = I_0 \sin\varphi + V/R + C\frac{dV}{dt} \qquad (1.14)$$

where $C\,\partial V/\partial t$ is the displacement current through capacitor, V/R is current through the resistor.

Rewriting above balance equation by using the second Josephson equation gives

$$I - I_0 \sin\varphi = -\frac{2e}{\hbar}\frac{\partial U}{\partial \varphi} = \frac{\hbar}{2e}\frac{1}{R}\frac{d\varphi}{dt} + \frac{\hbar}{2e}C\frac{d^2\varphi}{dt^2} \qquad (1.15)$$

where $$U = -\frac{\Phi_0}{2\pi}\left(I\varphi + I_0\cos\varphi\right) \qquad (1.16)$$

The above equation provides the dynamics of the junction which is similar to the motion of a ball moving on the "tilted washboard" potential U.

In the static case, for $I < I_0$, the particle is confined to one of the potential minima as specified in fig.1.9(b), where it oscillates back and forth at the plasma frequency

$$\omega_P = \omega_{P0}\left(1 - (I/I_0)^2\right)^{1/4} \quad \text{with}$$

$$\omega_{P0} = \left(\frac{2\pi}{\Phi_0}\frac{I_0}{C}\right)^{1/2} \qquad (1.17)$$

The average phase φ is constant and hence the time averaged dc voltage V is zero.

As the current I exceeds I_0, the local minima in the washboard potential disappear (fig.1.9(c)), and the phase difference evolves in time. A finite dc average voltage V across the junction increases with increasing bias current.

As soon as bias current reduces than I_0, the particle becomes trapped in one of the wells of the washboard at a current which depends on the capacitance of the junction. The β_C is a frequently used damping parameter introduced by Stewart and McCumber

$$\beta_c = \frac{2\pi I_0 R^2 C}{\Phi_0} \qquad (1.18)$$

In the absence of noise, we should consider the two limiting cases:

(i) β_C <<1 (strongly overdamped limit) and (ii) β_C >1 (strongly underdamped limit)

(i) Overdamped Junction:

As (β_C <<1), the inertial term in (1.15) is negligible, which corresponds to a negligible junction capacitance. It means that with reducing the bias current from above I_0, the particle gets trapped instantly in one of the minima of the washboard potential at $I = I_0$, which results in non-hysteretic I–V characteristics. Solving (1.15) with β_C=0 one finds for the normalized time dependent voltage $u = V / I_0 R \quad and \quad i = I / I_0$.

$$\begin{aligned} u &= 0 && for\ I < 1 \\ u(t) &= \frac{i^2 - 1}{i + \cos \omega t} && for\ I > 1 \end{aligned} \qquad (1.19)$$

$$\omega = \omega_C \sqrt{i^2 - 1}\ ; \qquad \omega_C = \frac{2\pi I_0 R}{\Phi_0}$$

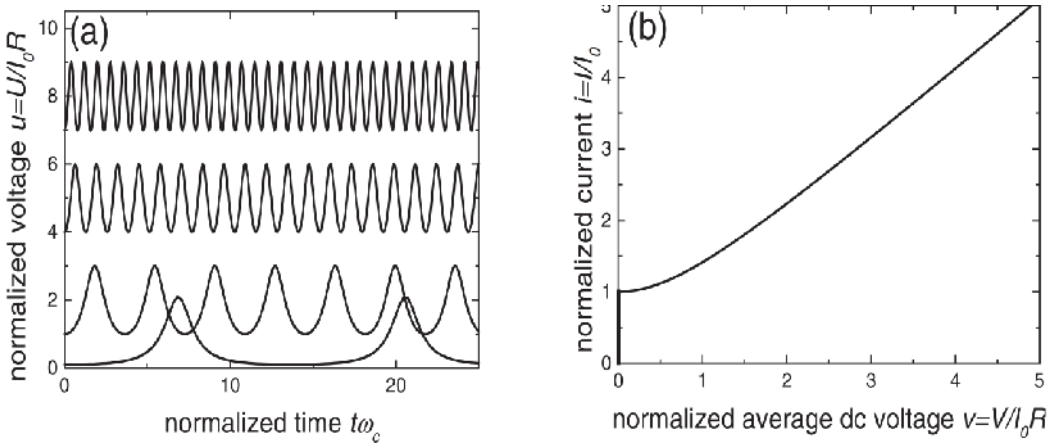

Fig. 1.10 Characteristics for a strongly overdamped junction calculated within the RSJ model: (a) Normalized voltage vs. time [from (for a d.c. current bias I_{dc}/I_0 = 1.2 (A), I_{dc}/I_0 = 4(B); (b) normalized current vs dc voltage [28].

As shown in fig. 1.10(a) for $i > 1$, the voltage u oscillates with frequency ω, which increases with increasing bias current. The normalized time averaged voltage $v = \overline{V} / I_0 R$ is zero for $i < 1$ and increases also with increasing i according to

$$v = \sqrt{i^2 - 1} \qquad for\ \ i > 1, \qquad (1.20)$$

as shown in fig. 1.10(b).

(ii) Underdamped Junctions:

When C is large enough, so that β_C > 1, the I-V curve become hysteretic as shown in fig. 1.11. In the absence of thermally activated processes, upon increasing I, from zero, (V = 0) until I_0, at which point V jumps discontinuously up to a finite voltage V, corresponding to a "running state" in which the phase difference φ increases at the rate $2eV/\hbar$. (In the washboard analog, this corresponds to the mass point sliding steadily down the inclined washboard.)

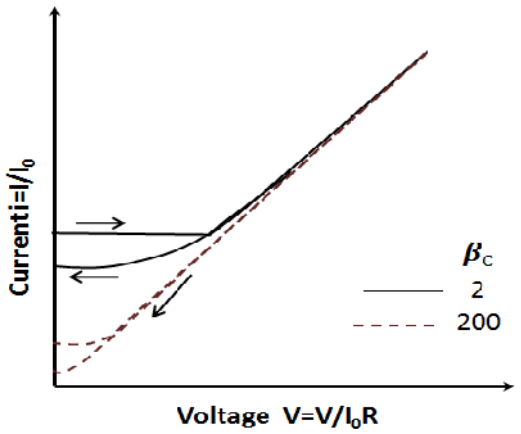

Fig.1.11 Hysteretic current voltage characteristics, calculated within the RCSJ model for various values of β_C (arrows indicate direction of bias current sweep)[28].

In the simple RCSJ model, this $V \approx I_0 R$, but in an ideal tunnel junction at $T << T_C$, the voltage jumps up to near the energy gap voltage $V_g = 2\Delta / e$. If I is reduced below I_0, V does not drop back to zero until a "retrapping current" $I_{r0} = 4I_0 / \pi\beta_C^{1/2}$ is reached. (In the analog, this hysteresis reflects the effect of the inertia of the moving mass, which with light damping can carry it up and over a barrier which would have stopped it, if damping were heavy.) Figure 1.11 shows the hysteretic $I-V$ characteristics for various values of β_C.

1.2 Superconducting Quantum Interference Device (SQUID)

The Superconducting quantum interference devices (SQUID) are the most sensitive detectors of magnetic field and magnetic flux. Any physical quantities that can be converted into a magnetic flux such as magnetic field, magnetic field gradient, current, voltage are measured by these sensors. These devices consist of superconducting loop interrupted by two Josephson junctions and its operational basic principle is based on two physical effects: the Josephson Effect and the quantization of magnetic flux in a superconducting ring. In particular, low critical temperature SQUID magnetometers having an area less than 1cm^2 are able to detect values of magnetic fields as low as a few fT/Hz$^{1/2}$. Due to their peculiar characteristics, these sensors are widely used in several applications such as biomagnetism [26,27], magnetometers and susceptometers [28], nondestructive evaluation [29], geophysics [30], scanning SQUID microscope [31], and nuclear magnetic resonance [32] etc. In this section, brief description of direct current SQUID i.e. dc-SQUID and its working principle is presented. Also physical theory concerning thermal and low frequency noise is described to recognize promising source of noise.

1.2.1 Quantization of Magnetic Flux:

The quantization of magnetic flux was first predicted by London [22], and observed experimentally by Deaver and Fairbank [23]. By lowering the temperature below Tc, superconductor loop undergoes a normal-superconductor phase transition. In the presence of an external magnetic field, a residual magnetic flux may remain in the loop even after the external magnetic field has been switched off. This flux is produced by the persistent supercurrent generated in the loop and outstandingly, it has only integer multiple values of the fundamental flux quantum $\Phi_0 = h/2e$ = 2.07 × 10^{-15} Wb, thus it is quantized.

$$\Phi = n\,\Phi_0 \qquad (1.21)$$

where n is an integer.

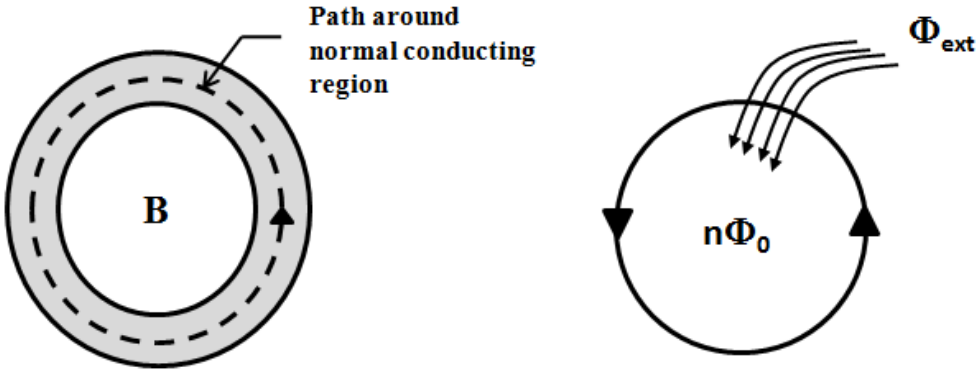

Fig 1.12 Schematic representation of flux quantization in superconducting ring in presence of external magnetic field.

The quantization of magnetic flux in a superconducting ring is a direct consequence of the fact that the macroscopic wave function ψ, describing the macroscopic quantum state relative to the condensation of Cooper pairs into a single state that must be single valued.

$$\psi(\vec{r},t) = \left|\psi(\vec{r},t)\right| e^{i\varphi((\vec{r},t))} \; ; \quad n_S = \left|\psi(r,t)\right|^2 \tag{1.22}$$

This means that in the absence of applied magnetic fields, the macroscopic superconducting phase $\varphi(r,t)$ takes the same value for all Cooper pairs throughout the superconductor. The phase of this wave function is dependent on the supercurrent density $\vec{j}_S$ and the magnetic vector potential *A*. This relationship can be described by [3]:

$$\vec{\nabla}\varphi = \frac{2\pi}{\Phi_0}\left[\frac{m}{2n_s e^2}\vec{J}_s + A\right] \tag{1.23}$$

The superconducting electron density is denoted by n_S. To ensure the single–valuedness of the complex wave function the phase difference across an arbitrary closed path can only vary by an integer times 2π. This gives the fluxoid (Φ') quantization condition:

$$\int \vec{\nabla}\varphi.d\vec{l} = 2\pi\left[\frac{2e}{h}\frac{m}{2n_s e^2}\int \vec{J}_s d\vec{l} + \frac{2e}{h}\int \vec{A}\,d\vec{l}\right] = 2\pi n \tag{1.24}$$

Rearranging this equation and applying the theory of Stokes gives:

$$\left(\frac{m}{n_s e^2}\int_l \vec{J}_s d\vec{l} + \int_s \vec{B}\,d\vec{A}\right) = \Phi' = n\frac{h}{2e} = n\Phi_0 \tag{1.25}$$

First integral on the left side of (1.25) can be neglected, if we consider the path is far away from the surface where $\vec{j}_S = 0$. Hence

$$\int_s \vec{B}.d\vec{S} = \Phi' = n\Phi_0 \tag{1.26}$$

The magnetic flux frozen in a superconducting ring can assume only quantized values because the supercurrent circulating in the ring generates the magnetic flux, which is quantized. This condition is schematically shown in fig.1.12. The current can assume only those values that yield an integral number of wavelengths of the superconducting wavefunction over the ring length. This situation is exactly analogous to the quantization of electron orbits in the Bohr atom.

1.2.2 The DC- SQUID:

In 1964, the dc-SQUID was developed by Robert Jaklevic, John J. Lambe, Arnold Silver and James Mercereau in Ford Research Labs [19]. This device consists of two parallel Josephson junctions interrupting a superconducting loop, as shown in fig.1.13. The dc-SQUID is extensively used as a magnetic flux-to-voltage transformer.

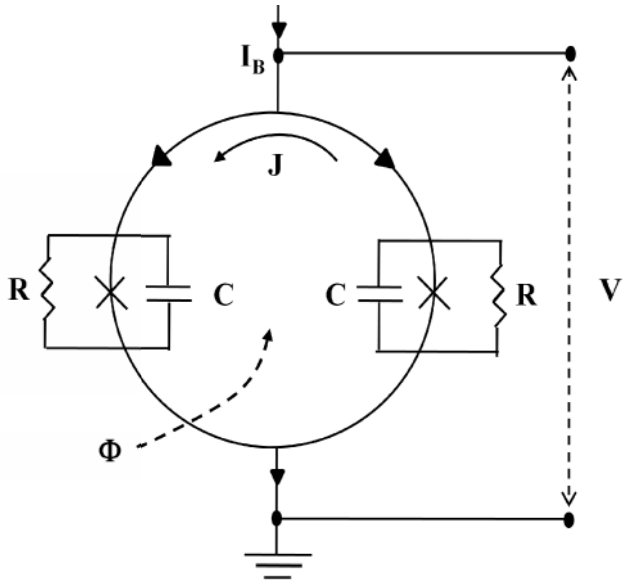

Fig.1.13 Schematic representation of a dc SQUID. Two Josephson junctions represented by the two crosses interrupt a superconductive loop. A bias current can be feed in both junctions through the parallel connection. A dc SQUID is operated by constant biasing current I_B, a variation of the voltage V is achieved when the externally applied magnetic flux changes. The two shunt resistances R and the capacitance C of each junction are also shown.

A quantitative description of a dc-SQUID operation, containing two junctions, symmetrically incorporated into the SQUID loop can be easily obtained by using the RCSJ model for the currents flowing through the two Josephson junctions. In addition, one needs Kirchhoff's laws and an equation relating the phase differences φ_L and φ_R of the two junctions, the flux is penetrating the SQUID loop and the currents circulating around the loop. We refer to the notation of fig.1.13. The current through left junction can be written as half the bias current I plus the circulating current J, $I_L = I/2 + J$. Similarly, we can write the current through right junction as $I_R = I/2 - J$. Equating these currents to the sum of supercurrent, quasiparticle current through each junction, as in the RCSJ model, we can obtain by neglecting the capacitance:

$$\frac{I}{2} \pm J = I_0 \sin\varphi_k + \frac{\Phi_0}{2\pi R}\dot{\varphi}_k \tag{1.27}$$

where the L and R refer to the two junctions. The phase differences φ_L and φ_R are related by

$$\varphi_L - \varphi_R = \frac{2\pi}{\Phi_0}(\Phi_a + LJ) = \frac{2\pi}{\Phi_0}\Phi_T \tag{1.28}$$

The flux Φ_T is the total flux through the SQUID loop having contributions from the applied magnetic field and from the circulating current J. The first contribution may be written as $\Phi_a = B.A$, where A is the loop area. The contribution from the circulating current J can be written as LJ where the SQUID inductance L has a geometric contribution as well as a kinetic contribution can play a role, if the film thickness is comparable to or smaller than the London penetration depth λ_L and the linewidth of the superconducting structures is small.

If we neglect the SQUID inductance, we have:

$$\varphi_L - \varphi_R = \frac{2\pi}{\Phi_0}\Phi_a \tag{1.29}$$

By adding the 1.27 equations, it is possible to obtain

$$I_C = 2I_0 \cos\frac{\pi\Phi_a}{\Phi_0} \sin\left(\frac{\varphi_L + \varphi_R}{2}\right) \tag{1.30}$$

So the maximum critical current of a dc SQUID is

$$I_C = 2I_0 \cos\frac{\pi\Phi_a}{\Phi_0}. \tag{1.32}$$

Each junction is resistively shunted to eliminate any hysteresis on the current-voltage characteristic as expressed in RCSJ model with the intention that the I-V characteristics appear as sketched in figure 1.15 (a).

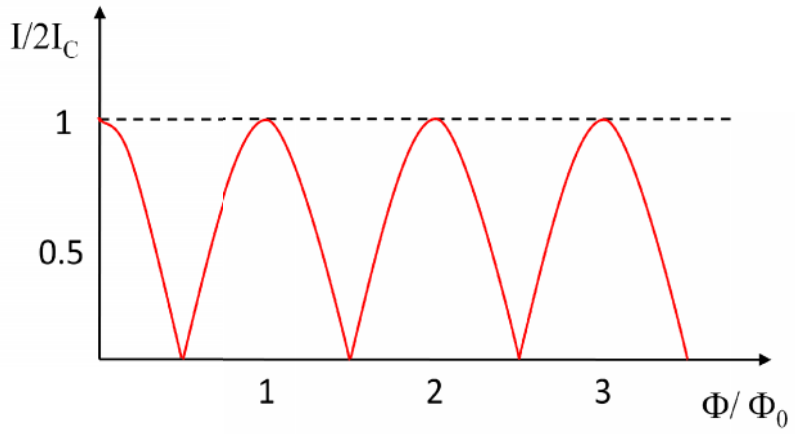

Fig.1.14 Schematic representation of Change in the total magnetic flux through SQUID interior is periodic with respect to the maximum supercurrent through the two-junction.

The effect of the screening current J flowing around the SQUID loop is the reduction of the critical current of the SQUID from $2I_C$ to $(2I_C - 2J)$. In fact, this circulating current adds and subtracts respectively itself to the bias current flowing in the two branches of the loop containing the junctions, so that the critical current of the junction is reached at $I/2 + J = I_C$. Thus the SQUID switches to the voltage state at $I > 2I_C - 2J$. Since I_C is a periodic function of the externally applied flux (fig. 1.14)

.

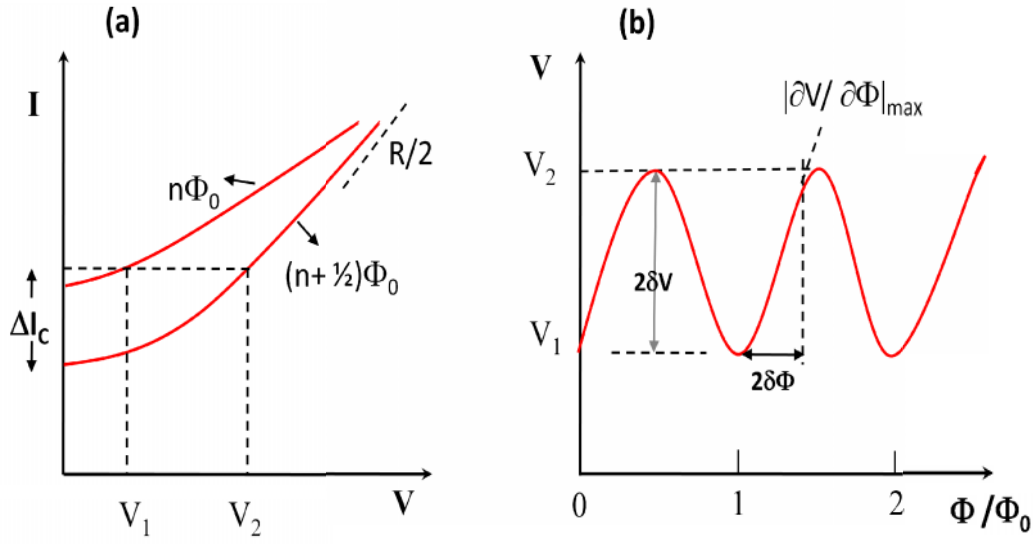

Fig.1.15 (a) Schematic representation of the current–voltage (IV) characteristic of DC SQUID as a function of the applied magnetic flux. The two limiting situations, occurring for $\Phi=n\Phi_0$ and $\Phi=(n+1/2)\Phi_0$ are shown. (b) DC SQUID voltage modulation characteristic as a function of applied magnetic field, measured at a constant bias current [24].

As a consequence of these considerations, if the SQUID is biased with a current slightly larger than $2I_C$, the output voltage of the SQUID turns out to be periodic function of the magnetic flux applied perpendicular to the plane of the SQUID loop, as shown in figure 1.15(b). The SQUID device thus works as a transducer of magnetic flux producing measurable voltage, which changes its output for small changes of the applied magnetic flux.

In case of identical current and very low inductance junction, the critical current of the dc SQUID modulates between $2I_C$ and 0 (see fig. 1.14). A reduction of the modulation depth occurs for nonzero values of the screening parameter $(\beta_L = 2LI_0/\Phi_0)$ as shown in Fig. 1.16(b). For $\beta_L = 1$ the critical current modulates by fifty percentage, and for $\beta_L >> 1$, $\Delta I_C / I_{C\max}$ decreases as $1/\beta_L$. The reason for the $1/\beta_L$ decrease can be understood in the following way. When the applied flux is $\Phi_0/2$ the largest circulating current required to lift the total flux to an integer number is of the order of $J = \Phi_0/2L \; or \; J/I_0 = 1/\beta_L$. The minimum critical current is of the order of $2(I_0 - J)$ and

$$\Delta I_C = I_C - I_m = 2I_0 - 2(I_0 - J) = 2J = \frac{2I_0}{\beta} \quad \text{Hence} \quad \frac{\Delta I_C}{I_C} = \frac{1}{\beta} \tag{1.32}$$

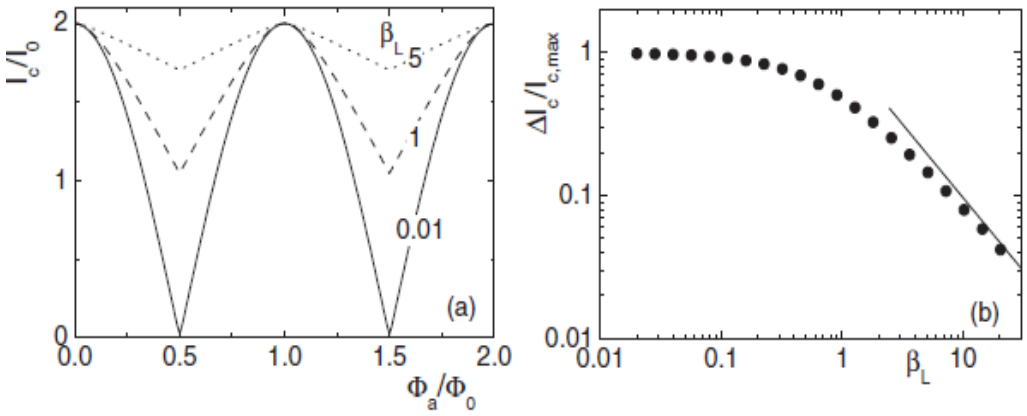

Fig.1.16. (a) Critical current of the dc SQUID vs. applied flux for 3 different values of the screening parameter β_L. Junction parameters are assumed to be identical. (b) Modulation depth $\Delta I_C/I_{C\,max}$ vs. β_L. Solid line in (b) is function β_L^{-1}[25].

An important parameter characterizing the efficiency of SQUID operation is the flux to-voltage transfer coefficient V_Φ. In fact, the maximum responses to a small flux change $\delta\Phi << \Phi_0$ is obtained by choosing the bias current so that it maximizes the amplitude of the voltage modulation and sets the external flux at

$\Phi_a \approx (2n+1)\Phi_0/4$, where the transfer coefficient $V_\Phi = \left|(\partial V/\partial\Phi_a)\right|$ is a maximum. The resulting voltage change $\partial V = V_\Phi \partial\Phi_a$ is approximately linear in this regime.

The maximum value V_Φ can be obtained observing that, as the flux varies by $\Phi_0/2$, the critical current variation is Φ_0/L, and the corresponding voltage variation is $\Delta V = (\Phi_0/L)R/2$, where R/2 is the parallel resistance of the two shunts. This gives the value $V_{\Phi,\max} \approx \Delta V/(\Phi_0/2) \approx R/L$.

Consider the zero voltage case where $\beta_L << 1, \beta_C << 1$ and junction parameters are identical. By means of these normalizations the dc SQUID equations of the Langevin type transform reduces to

$$\frac{I}{2}+J=I_0\sin\varphi_L+\frac{\Phi_0}{2\pi R}\dot{\varphi}_L \quad \text{and}$$
$$\frac{I}{2}-J=I_0\sin\varphi_R+\frac{\Phi_0}{2\pi R}\dot{\varphi}_R \qquad (1.33)$$

Adding 1.33 and from 1.28, we obtain

$$I=2I_0\left[\cos\frac{\pi\Phi_a}{\Phi_0}.\sin\gamma+\frac{\Phi_0}{\pi R}\dot{\gamma}\right] \qquad (1.34)$$

where $\gamma=(\varphi_L+\varphi_R)/2$.

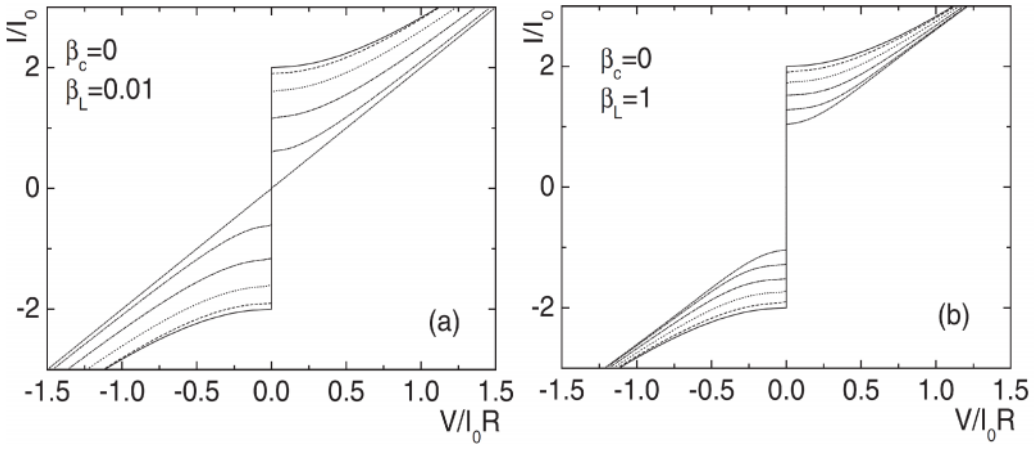

Fig.1.17. Current voltage characteristics of dc SQUIDs for β_L= 0.01, 1 and βc = 0. Applied flux is increased from 0(solid line) to $\Phi_0/2$ (short dashed line) in steps of $0.1\Phi_0$ [25]. These curves have been obtained by numerically solving dc SQUID equations of the Langevin type transform. Thus the modulation in I_C directly shifted into a modulation of V.

This equation is identical to the RCSJ equation of a single junction, if a parallel resistance R/2 of the two junctions, a capacitance 2C and a critical current $2I_C \cos\pi\varphi_L$ are considered. Taking into account, the voltage appear across SQUID where the $\beta_L << 1$, the current–voltage characteristic for $I > I_C$ is given by

$$V = \frac{R}{2}\sqrt{I^2 - I_C^2}$$
$$I_C = 2I_0 \cos\frac{\pi\Phi_a}{\Phi_0} \qquad (1.35)$$

Thus the dc voltage oscillates with flux by a period of one flux quantum, by means of minima at integer multiples of Φ_0. For the slope $\partial V / \partial\Phi_a$ we get

$$\frac{\partial V}{\partial\Phi_a} = -2\pi.\frac{I_0 R}{\Phi_0}.\frac{I_0.\sin\pi\Phi_a/\Phi_0 \,.\, \cos\pi\Phi_a/\Phi_0}{(I^2 - I_C^2)^{1/2}} \qquad (1.36)$$

The expression (1.36) actually diverges for $I = I_C$. However, in the presence of thermal fluctuations, $\partial V / \partial\Phi_a$ becomes finite for all currents, with a maximum value near its divergence in the noise-free case. Thus we can define the SQUID transfer function $V_\Phi = \max(|\partial V / \partial\Phi_a|)$ where maximization is with respect to bias current and flux.

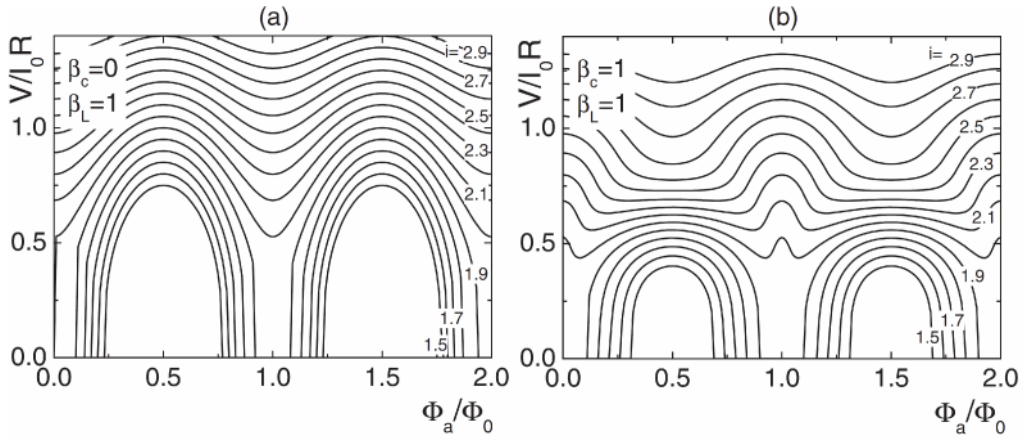

Fig. 1.18 dc-SQUID modulation V(Φ_a) for several values of normalized bias current from 1.5 to 1.9 calculated for strongly overdamped (a) and intermediately damped (b) junctions [25].

From (1.35) we can also see that the peak-to-peak-modulation in $V(\Phi_a)$ is given by

$$V = V(\Phi_a = \Phi_0/2) - V(\Phi_a = 0) = I_0 R\left[\frac{I}{2I_0} - \sqrt{(\frac{I}{2I_0})^2 - 1}\right] \qquad (1.37)$$

which for $I = 2I_0$ reaches its maximum value $I_0 R$. When the SQUID inductance is taken into account the modulation of both I_C and V decreases (fig. 1.17(b)).

1.2.2 Thermal Noise in DC SQUID:

A very essential issue in connection with the SQUID operation is the thermal fluctuations which generate voltage noise and affects the SQUID performances. Obviously, one must keep noise as low as possible to obtain comprehensible outcome. The major source of noise is related to the presence of shunt resistance in the junctions constituting the SQUID. Resistors are affected by voltage noise because of the thermal fluctuation of the electron density, the so called Nyquist noise.

The dominant noise source in dc-SQUIDs based on resistively shunted junctions is Johnson noise, which can be described by the following voltage noise spectral density $(S_V^{1/2})$ [33]:

$$S_\upsilon^{1/2} = \gamma 2 k_B T R \qquad (1.38)$$

Here $\gamma\,(\approx 8)$ is a factor associated with down-mixing of Johnson noise generated at the Josephson frequency and *R* is the shunting resistor of a single junction.

When $I >> I_0$, the resistive shunt has an associated Nyquist noise current with a spectral density $S_I(f) = 4k_B T/R$, where k_B is Boltzmann's constant. This noise has two effects.

1) First, it rounds the I–V characteristic, namely "noise rounded" at low voltages and reduces the apparent critical current.
2) Second, the noise current induces a voltage noise across the junction at nonzero voltages.

One can distinguish the two regimes of small and large thermal fluctuations in SQUIDs. In the regime of small thermal fluctuations, both the noise parameter (Γ as the ratio of the thermal energy over the Josephson coupling energy) and the normalized inductance are much less than 1. In contrast, the regime of large thermal fluctuations is reached when either Γ or normalized inductance is comparable to one or even larger.

The effect of the fluctuating current on the I-V characteristics has clearly demonstrated in the representation of the tilted washboard potential. For $I < I_0$ the fluctuating tilt may cause the total current $I + I_N(t)$ to exceed I_0, which facilitated the particle to roll out of the potential minimum to the next. In overdamped junction this produces a series of voltage pulses randomly spaced in time. Hence, the time averaged dc voltage V becomes finite, even for $I < I_0$, as a results the I–V characteristics are "noise rounded" at low voltages.

The noise currents are implemented as Gaussian distributed random numbers [33]. Due to the thermal noise, (zero voltage state) value of the critical current is reduced simultaneously with increasing value of Γ. In case of a finite junction capacitance, the hysteresis in the I-V curve is suppressed. Obviously, the thermal fluctuations "destroy" the Josephson coupling if Γ is large enough or I_0 is small enough.

To maintain a reasonable degree of Josephson coupling, Josephson coupling energy $(I_0\Phi_0 / 2\pi)$ should be more than $k_B T$. ($I_0\Phi_0 \gg k_B T$) is required. This inequality is conveniently written as $\Gamma = 2\pi k_B T / I_0\Phi_0 \ll 1$.

Nyquist noise in the shunt resistors imposes an upper limit on the SQUID inductance; $\Phi_0^2/2L \gg 2\pi k_B T$ this criterion must satisfy to obtain the quantum interference. The Nyquist noise in the shunt resistors introduces a white voltage noise across the SQUID with a spectral density $S_V(f)$, which turns into the flux noise spectral density as

$$S_\Phi(f) = S_v(f)/V_\Phi^2 \qquad (1.39)$$

Since the latter parameter takes into account the dimension of the SQUID loop [33], it is often useful to characterize SQUIDs in terms of their noise energy

$$\varepsilon(f) = S_\Phi(f)/2L \qquad (1.40)$$

The noise energy becomes a good parameter to compare different SQUIDs.

1.2.3 Low Frequency Noise in DC SQUID:

In several practical applications, thermal fluctuations (the white noise of Josephson junctions) limit the sensitivity of SQUIDs over a wide frequency range. However, a few applications, such as biomagnetism and geophysical require operation at low frequencies down to 0.1Hz or less. The SQUID measurements at the low frequencies, the 1/*f* noise ("flicker" noise) starts to play an important role with involvement to the total noise. At least three separate sources of 1/*f* noise can be distinguished in dc-SQUIDs based on SIS resistively shunted junctions [34].

1) The first is associated with the trapping of electrons into the defects available in the junction tunnel barriers [34].
2) It is also caused by the motion of flux lines which are trapped in the SQUID. [35,36]
3) Recently Koch and Clarke [34, 37] reported that it has also been associated with the magnetic moments of electrons trapped in defect states in the superconductor.

In the tunneling process, an electron gets trapped on a defect in barrier and released subsequently. The local change in height of barrier subsequent the trapped electron changes the critical current density of same region. At low frequencies, the spectral density of this process is a Lorentzian,

$$S(f) \propto \frac{\tau}{1+(2\pi f\tau)^2} \tag{1.41}$$

where τ is mean time between pulses and falling off as $1/f^2$ at frequencies above $1/2\pi\tau$. Trapping process is thermally activated in many cases so τ is of the form

$$\tau = \tau_0 \exp(E/k_B T) \tag{1.42}$$

Normally several traps in junction having individual characteristic time occur, assuming all are statistically independent, we obtain a spectral density [38]

$$S(f) \propto \int dE\, D(E)\left[\frac{\tau_0 \exp(E/k_B T)}{1+(2\pi f\tau_0)^2 \exp(2E/k_B T)}\right] \tag{1.43}$$

where D(E) is distribution of activation energies. The term in bracket is a peak function of E. Thus traps having energy with a range $k_B T$ of E involves to the noise. In case of broad peak, eq. can rearrange by taking D (E) outside the integral, we obtain

$$S(f,T) \propto \frac{k_B T}{f} D(\tilde{E}) \tag{1.44}$$

Thus 1/f like spectrum can be obtained for few traps only. The magnitude of 1/f noise in critical current depends on the quality of the junction which can be measured by the current leakage at voltage below the energy of the two superconductors. These traps will trouble electrons to tunnel in the low voltage range creating leakage current as well as 1/f noise. Thus junctions with low subgap leakage currents will have low 1/f noise. Another vital source of noise is motion of flux lines trapped in body of the SQUID. Hence the level of 1/f noise strongly

depends on the microstructures of the thin films. The instant way to reduce low frequency noise arises due to trapping of vortices is to make the superconducting films sufficiently narrow [39].

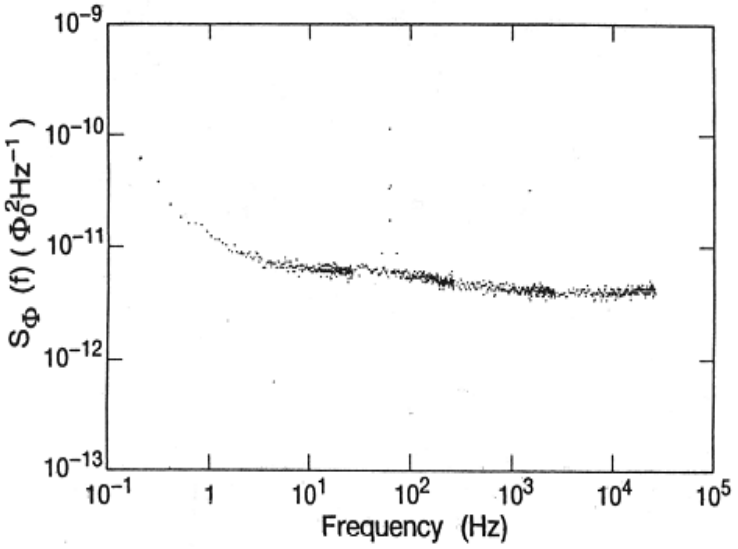

Fig.1.19 Spectral density of equivalent flux noise of the dc SQUID: L=0.2 nH, R=8 and T=4.2K [38].

An important practical difference between two sources of 1/f noise is the critical current noise can be reduced by a suitable modulation scheme, whereas flux noise cannot. One can find the spectral density of the 1/f noise across the SQUID at constant current bias is given by following formula:

$$S_v(f) \approx \frac{1}{2}\left[(\partial V / \partial I_0)^2 + L^2 V_\Phi^2 \right] S_{I_0}(f) \qquad (1.45)$$

In the above equation, we assumed symmetric junctions with spectral density S_{I0}. The presences of two terms inside a bracket are specific sense. First term represents the "*in phase mode*" where both junctions produce fluctuation of same polarity and the second represents "*out of phase mode*" where both junctions are of opposite polarity. In phase mode, noise can be illuminated by the conventional flux modulation scheme provided modulation frequency is much higher than 1/f noise frequency. Out of phase mode results in a current around the SQUID loop. At $V_\Phi = 0$, the flux noise vanishes but cannot be reduced. The two critical currents contributed to the measured noise only in-phase fluctuations, while out-of-phase fluctuations which generated current noise around the SQUID loop. Fascinating scheme which will reduce both fluctuation terms (in phase mode and out of phase mode) was established by Koch et al. [37]. But no bias scheme can remove the 1/f noise formed by motion of flux.

References:

1. L. Solymar: “Superconductive Tunneling and Applications” (Chapman and Hall, London) (1972)
2. A. Barone and G. Paterno, “Physics and Applications of the Josephson Effect” (Wiley-Interscience Publication)(1982)
3. M. Tinkham, Introduction to Superconductivity 2nd Ed. (McGraw-Hill, Inc.)(1996)
4. V.V. Schmidt, “The Physics of Superconductors: Introduction to Fundamentals and Applications”, P. Mfiller A.V. Ustinov (Eds.) (1997)
5. J. Bardeen, L.N. Cooper and J. R. Schrieffer, Phys. Rev. 108, 1175 (1957)
6. L. Esaki, Phy. Rev. 109, 603 (1957)
7. I. Giaever, LT7, p-327
8. I. Giaever, Phys. Rev. Letts. 5, 147(1960)
9. I. Giaever, Phys. Rev. Letts. 5, 464(1960)
10. J. Nicol, S. Shapiro and P. H. Smith, Phys. Rev. Letts. 5, 461(1960)
11. B.D. Josephson: Phys. Letts. 1,251 (1962)
12. I.K.Yanson, V.M. Svistunov, I.M. Dmitrenko: Zh. Ep. Tr. Fiz. 48, 976 (1965) English transl.: Soy. Phys. JETP 21,650 (1965)
13. S.Shapiro: Phys. Rev. Letts. 11, 80 (1963)
14. K. K. Likharev, Rev. Mod. Phys.51, 101(1979)
15. K.K. Likharev, B.T. Ulrich: “Systems with Josephson Junctions. The Basics of the Theory” (Moscow State Univ. Press, Moscow) (1978)
16. R.P. Feynman, R.B. Leighton, M. Sands: “The Feynman Lectures on Physics.3: Quantum Mechanics” (Addison-Wesley, Reading, MA) (1965)
17. P. W. Anderson and J. M. Rowell. Phys. Rev. Letts. 10,230–232 (1963)
18. J. M. Rowell. Phys. Rev. Letts., 11,200–202 (1963)
19. R.C. Jaklevic, J. Lambe, A. H. Silver, and J. E. Mercereau. Phys. Rev. Letts., 12(7), 159–160(1964)
20. W. Buckel and R. Kleiner; “Superconductivity”, Wiley –VCH Verlag CmbH & Co. KGaA, Germany (2004)
21. A.M. Kadin; “Introduction to Superconducting Circuits”, John Wiley & Sons inc, USA(1999)
22. F. London and H. London; Proc. Roy. Soc. A149, 71 (1935)
23. B. S. Deaver and W. M. Fairbank. Phys. Rev. Lett., 7:43–46, (1961)

24. John Clarke and Alex I. Braginski (Eds.), "The SQUID Handbook, Vol-I Fundamentals and technology of SQUIDs and SQUID system", (WILEY-VCH- 2004)
25. Harold Weinstock (Eds.), "SQUID Sensors: Fundamentals, Fabrication and Application", (Kluwer Academic Publisher, 1996)
26. Pizzella V, Penna, Gratta, Romani, Supercond. Sci. Technol. 14: R79, (2001)
27. Granata C, Vettoliere A, Rombetto S, Nappi C, Russo M, J. Appl. Phys. 104:073905, (2008)
28. Ketchen M B, Kopley T, Ling H, Appl. Phys. Lett. 44: 1008–10, (1984)
29. Jenks W G, Sadeghi S S H, Wikswo Jr J P, J. Phys. D. Appl. Phys. 30:293, (1997)
30. Clarke J, IEEE Trans. Magn. 19: 288-294, (1983)
31. Kirtley J R, Ketchen M B, Stawiasz K G, Sun J Z, Gallagher W J, Blanton S H and Wind S J, Appl. Phys. Lett. 66:1138, (1995)
32. Greenberg Ya S, Rev. Mod. Phys. 70: 175-222, (1998)
33. Tesche, C.D. and Clarke, J., J. Low Temp. Phys.27, 301–331, (1977)
34. R.H. Koch, J. Clarke, W.M. Goubau, J.M. Martinis, C.M. Pegrum and D.J. van Harlingen; J. Low Temp. Phys. 51, 207 (1983)
35. Hansma, P.K., J. Appl. Phys. 44, 4191–4194, (1973)
36. Rifkin, R., Vincent, D.A., Deaver, B.S. and Hansma, P.K., J. Appl. Phys. 47, 2645–650, (1976)
37. R.H Koch, D.P. DiVicenzo and J. Clarke; Phys. Rev. Lett. 98, 267003 (2007)
38. Wellstood, F.C., Urbina, C. and Clarke, J. Appl. Phys. Letts. 54, 2599-2601(1989)
39. Wellstood, F.C., Urbina, C. and Clarke, Appl. Phys. Letts. 85,22,5296-5298 (2004)

CHAPTER 2

Dayem Bridge Based SQUID

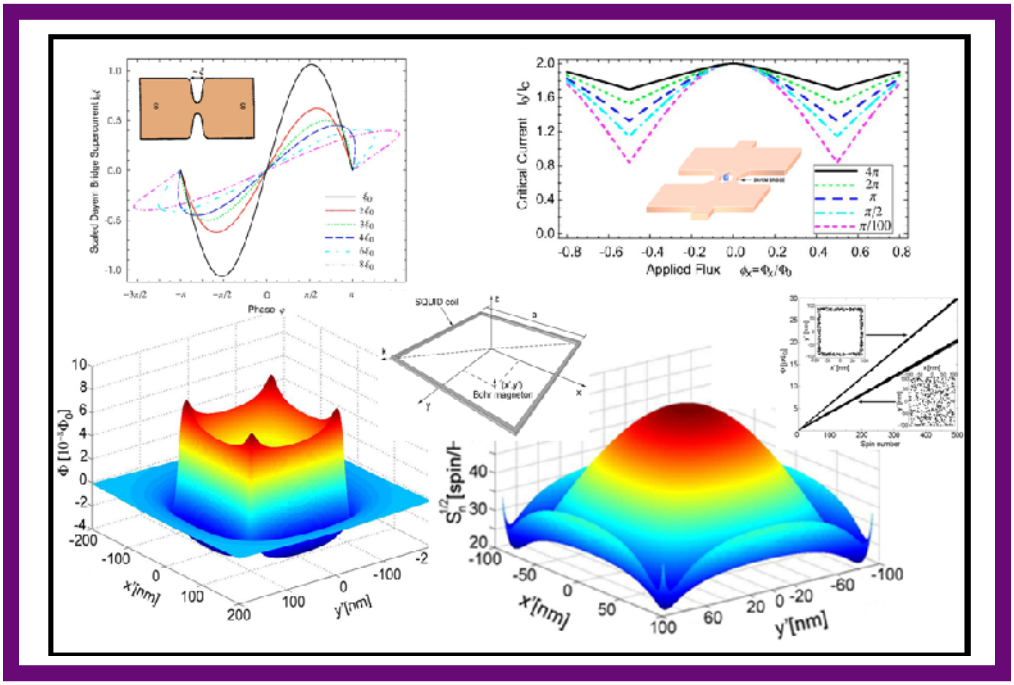

Research and development in science and industry insist on constantly smaller systems as represented by spin-based quantum information processing, spintronics and nano-electromechanical system, where single electronic spin detection poses a grand challenge. Such applications required very sensitive measurements with nanoscale SQUIDs, though it has yet to be effectively applied to nanoscale measurements. This chapter primarily deals with fundamentals of nano-SQUID, along with brief description of physics of dayem bridges and properties of SQUID based on Nb dayem bridges. Detailed $(I_C - \Phi)$ characterization of SQUID elucidates the role of dayem bridge dimension (L/ξ) has been described. The modern progress in nano-SQUID for magnetic nanoparticle detection has existing with novel ideas towards particle attachment into sensor area. The spin sensitivity simulation results, in order to understand the spin sensitivity performance of nano-SQUID as function of its position inside SQUID loop has been described. Also the magnetic flux distribution of spin clusters in different configuration and its statistical study with spin number has been illustrated.

2.1 Introduction:

Nanoscale superconducting quantum interference devices (nanoSQUID) are the branch of the emerging research due to their incredible applications during recent years [1-4]. In the early 1990s, the development in the micro-SQUID techniques [5,6], allowed the study of magnetization reversal in magnetic nanostructures [6]. The primary systems studied were micrometer-sized particles containing about 10^{10} magnetic moments. During the succeeding years, interest to measure smallest systems by improving the micro to nano-SQUID technique has increased. In 2000, possibility of clusters containing about 10^3 magnetic moments was studied. These achievements build attention to further improvements towards single magnetic moment study might be possible.

A challenge is the measurement of a single magnetic moment which could be achieved either by using shunted SQUIDs [7] or by reducing section of the nanobridges [8,11]. Nanofabrication improvements initiate nano-SQUIDs successful achievement. [7-11]. The nano-SQUIDs lead to a significant improvement concerning the detection of magnetization switching of individual magnetic particles or molecules. Therefore, nano-SQUIDs are very promising for quantum information processing based on spin systems [15, 16] such as the manipulation and measurement of single spins [17]. Hence, one need to build a reliable and scalable magnetization measurement scheme, sensitive at the single spin level (i.e. a nanoscale single Bohr magnetometer integrated at the solid state). Among all competing magnetometry techniques [18-19], the direct transduction from a single spin state to a measurable electrical quantity—charge, voltage or current—(a principle driving the growing field of quantum spintronics) are appearing a promising route [20]. The SQUIDs are the most sensitive magnetometers and gradiometers available which are extremely well suited for classical and quantum reversal studies in nanometer-sized particle and cluster magnetization measurements. However the demonstration of a SQUID magnetometry down to the single molecule has yet to be achieved.

2.1.1 Why Nano-SQUID?

In a SQUID, the magnetic detection is performed through inductive coupling of the loop to a local external magnetic field. Therefore, it emerges apparent that the device geometry has a direct influence on the magnetometry performance. Around 25 years ago, Ketchen *et al* [21] illustrated an idea of reducing the SQUID magnetometer size to improve their inductive coupling to small samples. Interestingly, the trend towards the miniaturization of nano-SQUIDs was also motivated by other very diverse objectives such as improving spatial resolution in scanning SQUID microscopy [22,23], implementing new kinds of superconducting qubits [24,25] or measuring persistent current mesoscopic normal rings [26].

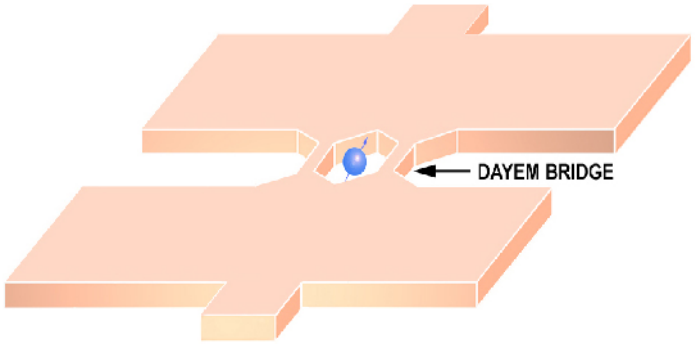

Fig. 2.1 Scheme of single spin detection where the single spin is placed at the center of Dayem Bridge based SQUID.

Ketchen *et al. have* calculated [27] the spin sensitivity S_n *(in term of number of spins)* for the peculiar geometry of *an assembly of spins placed at the SQUID loop center (see fig.2.1)*:

$$S_n = \frac{2a\,\Phi_{ns}}{\mu_B\,\mu_0} \qquad (1)$$

where Φ_{ns} is the SQUID flux noise, *a* is the SQUID loop radius, $\mu_B = 9.27\times10^{-24}\,J/T$ is the Bohr magneton and μ_0 is the vacuum permeability.

Thus, the spin sensitivity is linearly depending on the SQUID loop size. More recently Gallop *et al* [28,29] investigated in detail the detection limits of such miniaturized devices and concluded that single-spin detection (*Sn* < 1) could be achieved providing that the SQUID would be operated near the quantum limit.

On the experimental side, the Ketchen prediction has initiated a global trend towards miniaturization of the SQUID loop that showed the growing interest in quantum spintronics [16]. In most studies, it was concluded that, taking into account the actually measured flux noise in the best cases, the spin sensitivity S_n in the geometry proposed by Ketchen *et al* [27] would be limited to values in the range of 100–1000 number of spins.

2.1.2 Nano-SQUID Applications:

The nanoSQUID became important due to its various applications involving detection of tiny magnetic signal from small object as mentioned earlier. Some of the very interesting and widely used applications are briefly summarized.

The nano-SQUID was primarily convincing to be use as a magnetic flux detector for magnetization switching of the magnetic moment of a single molecule or atomic spin which was dream of the pioneering work of N´eel [30,31]. The first magnetization measurements of individual single-domain nanoparticles and nanowires at very low temperatures were presented by Wernsdorfer *et al* [6, 32]. An important feature of the nanoSQUIDs like CNT-SQUID is concerning the ability to tune the coupling between the detector and sample which provide a new generation of ultrasensitive magnetometers of nanometer-sized samples. Being able to position a small magnetic system on a nanoSQUID created a range of potential applications based on the magnetization studies of nanoparticles.

Most exciting application proposed for the nanoSQUID is a qubit based on nanometre-scale magnetic particles [33] where the quantum behavior of magnetic systems and non-interacting ensembles could be used as qubits and gates for a quantum computer. Thus the nano-SQUID is a very strong tool to contribute on the development of spintronics and spin-qubit. Various three-terminal devices based on nanoSQUIDs in both all Nb [11] and hybrid Nb–carbon nanotubes [12] are developed recently. The hybrid carbon nanotube three terminal devices use gate-tunable carbon nanotubes (CNTs) for the Josephson junctions where presence of combine features of single-electron transistors with typical properties of a SQUID interferometer. The gate tunability of the CNT junctions enhances the sensitivity of the device which is able to detect the spin of a single molecule. Recently, Giazotto et al. [34] has introduced the new kind of transistor device based on proximity effect between normal metal and superconducting metal incorporated in SQUID format so called SQUIPT that is superconducting quantum interference proximity which significantly increase the sensitivity with small magnetic moments.

Using the Single Photon Detector (SPD) consisting of the SQUID containing absorbing material inside the loop, it is feasible to convert a device into a transition edge detector due to isolated absorber, low thermal mass and strong coupling to the nanoSQUID. The response of the SQUID to the absorber temperature change is dependent on the differential T_c between the SQUID and the absorber materials [35,36]. Such detectors are important for synchrotrons due to increased sensitivity and spatial resolution offered by nanoSQUIDs. Nuclear magnetic resonance (NMR) of nanoparticles and macromolecules are used to analyze the chemistry of nanoparticle versus bulk particle, nanoparticle identification and characterization. NanoSQUIDs could also be used for the detection of macromolecules with masses >200 amu [36].

In Scanning SQUID microscopes (SSMs), used to image the local magnetic structures with the pick-up loops of sensor reducing the effective area of the SQUID, hence improving the resolution [38]. Best example is the imaging of the current flow in looped CNTs [37]. NanoSQUIDs positioned on the end of cantilever AFM tips can be used for imaging magnetically as well as topographically [38].Use arrays of micro/nano-SQUIDs

as a magnetometer for macroscopic samples is as privilege [39,40]. Three applications of particularly interest are crystals of magnetic molecular clusters [41], nucleation and depinning of magnetic domain walls in thin films [42] and arrays of magnetic dots [3].

2.2 Josephson Dayem Bridges:

The Josephson effect is not only the characteristic of "classical" superconductor-Insulator–superconductor (S-I-S) tunnel junctions but also a variety of superconducting weak links.

A superconducting weak link can be defined as a structure with reduced critical current separating two relatively bulky superconducting electrodes where a weak contact adequately play the role of a perturbation, not to change radically the electron states of the two pieces. A new wavefunction will then emerge for the superconductor as a result of interference between the wavefunctions from the two pieces. We are paying attention on the special kind of weak link called Dayem Bridge or nano-bridge. It is represented as the Josephson junction in a superconducting film formed by a short narrow constriction with length and width on the order of a few micro/nanometers or less as shown in fig.2.2.

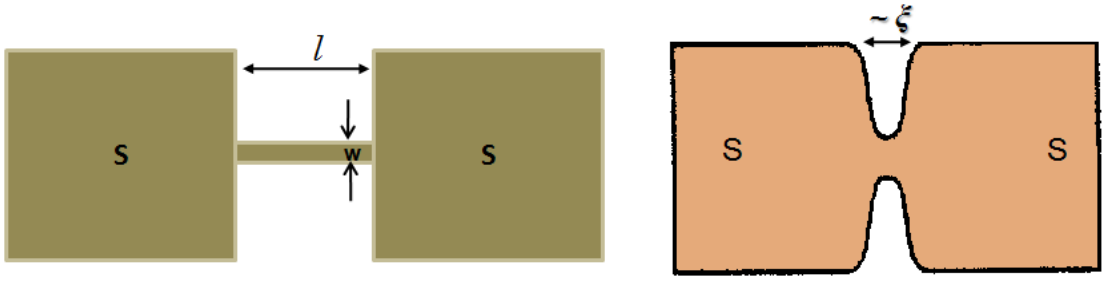

Fig.2.2 Schematic drawing of Dayem Bridge or nanobridge

In 1964, the Josephson effects [43] into the nanobridge junction were predicted by Anderson and Dayem [44]. An important class of Josephson weak links is employing planar configurations with single step thin film technology i.e. a single superconducting thin film is separating two relatively large superconducting regions (electrodes) by a short narrow constriction (Dayem bridge). The dimensions of the bridge should be smaller than or at least comparable with the temperature dependent coherence length of the bridge $\xi(T)$. In other words, a single valued and 2π periodic relationship exists between supercurrent I_S and phase difference (φ) of electrode only when the dimensions of weak link are comparable to coherence length. The restriction on the dimension of bridge in order to employ as Josephson link is due to its physical properties.

2.2.1. Fabrication Aspects:

The Dayem-bridge provides inherent advantages over other weak links such as point contacts or sandwich structures in terms of reproducibility, stability, and resistance to thermal cycling, especially if the bridges are made of a hard and chemically resistant material. Superconducting nanobridges are suitable structures for practical experiments, because hypothetically they can be created without facing the complexities such as several depositions, alignment and patterning steps associated with multi–layer thin film devices.

We often use the symbol l to indicate the physical length of the bridge (spacing between the electrodes) although the actual parameters may be some effective length l_e larger than the geometrical length because of the extension modifications of the order parameter into the electrodes, which can be due to link-electrode proximity effects and due to currents flowing in the electrodes.

In fact, besides geometrical ones, the lengths that characterize these weak link structures as follows:

1) The effective length of the link l_e, 2) The coherence length $\xi(T)$, 3) The electron mean free path ℓ and 4) The magnetic field penetration $\lambda(t)$ etc.

The relation between l_e and $\xi(T)$, i.e $l_e < \xi(T)$, and $l_e \geq \xi(T)$ provides a classification of "short" and "long" links respectively, whereas $\ell << l_e$ and $\ell \geq l_e$ define "dirty" and "clean" structures.

In a dayem bridge Josephson link, the conditions to be satisfied is that both length and width of the bridge should be smaller than or comparable to the coherence length, that is $l \approx \max[l, w] \leq \xi$ [14,45-47]. The condition required for the coherent transmission of Cooper pairs from one region to the other is roughly given by: $l \leq \xi$. To achieve this condition, the advanced technological procedures are needed to fabricate the links with both planar dimensions (up to few nm), comparable to the coherence length.

Nowadays, most successful and convenient nanoscale fabrication techniques available are electron beam lithography and focus ion beam milling etc. These techniques allows direct fabrication of reliable nanobridge as well as SQUID loop with dimensions of a few tens to hundreds nanometer from various materials like Al, Nb and Pb [48, 7-14]. The advantage of the electron beam lithography (EBL) techniques to fabricate high quality Nb nanobridge dc-SQUID is its high resolution [6, 9, 11]. It is important to make the SQUID out of a very thin layer to prevent flux trapping. Another technique useful for preparing devices is focused ion beam (FIB) fabrication [13, 8]. This technique has

presents some poverty of the device performance as a result of Nb contamination by the Ga ions used in the ion beam. The Ga can slowly diffuse into the Nb and make it unstable over time. The fabrication of the lowest noise devices is possible by using a W protective film during the ion beam milling process [13].

Apart from these two techniques, many novel ideas being introduced into fabrication techniques such as nanolithography incorporated with microscopy allows suitable device fabrication [49] where local anodization of thick Nb strip lines under the voltage-biased tip of an atomic force microscope (AFM). Nanobridge junctions and SQUID loops were obtained by oxidation of the Nb layer. The AFM-made SQUIDs proposed new features for example selective position fabrication, allowing an optimized coupling to magnetic signals and expecting an increased intrinsic sensitivity. In the case of small magnetic clusters which are placed very close to the nano-bridge junctions, an improvement of the sensitivity of one to two orders of magnitude might be achieved due to the reduction of the nano-bridge size. Also it is possible to fabricate nanoSQUID without lithography. Recently, Al SQUID fabricated on tip of quarts tube has reported by Amit Finkler et al [50]. Each fabrication technique has some advantage over other and also showing some limitations. The limitations are mainly due to contamination, imperfect chemical processing, thin film quality etc. Cleuziou et al. [12] designed a new SQUID with molecular Josephson junctions made up of a single-walled carbon nanotube (CNT) is the landmark achievement in SQUID research. Owing to the geometrical aspects of CNTs, such SQUIDs are also very promising to study the spin states of an individual magnetic molecule.

The nanoSQUID's enlightened in the present thesis has been fabricated using e-beam lithography which is elaborately described in the subsequent chapter.

2.2.2 Physics of Dayem Bridges:

The definition of a superconducting weak link, which is given by Likharev [46] states three properties that the Josephson junction must comprise:

- The Josephson junction supercurrent-phase relationship $I_0(\varphi)$ is 2π periodic so that $I_0(\varphi+2\pi)=I_0(\varphi)$
- The supercurrent in the Josephson junction is zero when the phase difference across the junction is an $n\pi$ (for any integer *n)*.
- The Josephson-junction supercurrent- phase relationship is anti-symmetric. So that $I_0(-\varphi)=-I_0(\varphi)$.

There are many factors involved directly or indirectly in Josephson behavior of dayem bridges; Such as geometrical factors, fabrication deficiencies and exact dimensions

etc. As referred in the earlier statements, the dimensions play an important role in the physical properties of the Dayem Bridges. Changing the dimensions is cost deviation into Josephson behavior. This deviation varies depending on whether the dayem bridge material is a superconducting or normal metal. Here we are paying attention to study the current phase relationship and temperature dependent properties of dayem bridges.

The Current Phase Relationship (CPR) in Nanobridges/Dayem Bridges:

An Important characteristic of superconducting structures is the relationship between the supercurrent through and the phase difference across the structure. The Josephson prediction and its experimental verification [43-45] of periodical current-phase relationships (CPR's) in (S-I-S) superconductor–insulator–superconductor tunnel junctions has generated the interest in research on Josephson devices. As well, applications based on the Josephson-like characteristics of superconducting nanobridges are explored widely [46,47]. Most theoretical studies are available on the exact nature of the CPR in nanobridge structures.

In this section, brief description about the origin of the CPR in superconducting nanobridges is introduced. More detailed observations are reported by Likharev [46] and Golubov, Kupriyanov and Il'Ichev [47].

Bridge Length Dependent CPR (at T≈T_C):

Likharev and Yakobson initially considered the effect of an increasing weak link length on the CPR for structures where the temperature is close to the critical temperatures of both the electrodes (Tc) and the nanobridge (Tc') [53]. Their model describes a deformation of the CPR from sinusoidal to saw tooth-like as a function of increasing bridge length [51]. Such deformation of the CPR is experimentally verified in 1980 by Pei et al [54] into the Indium microbridges.

Additionally, the nature of the CPR is predicted to become multi-valued at a critical length $l_C \geq 3.5\xi(T)$. In this limit, superconductivity is suppressed above the critical current by the nucleation of phase slip centers in the structure. The critical current (I_0) of the structures revealed that, at first, I_0 decreases with increasing weak link length. Then it saturates to a constant value for lengths larger than $8\ \xi(T)$ approximately.

The shape of the CPR changes from single–valued to multi–valued for lengths larger than a critical length (l_C) of approximately $3.5\ \xi(T)$. This variation is shown for different weak link lengths as shown in figure 2.3. The unstable branch of the phase function joining the point $I = I_0$ to the point $I = 0$, $\varphi = \pi$ corresponds to sharp drop

of order parameter in the middle of weak link i.e. nucleation of "phase-slip center" of length $\sim \xi$. In the long weak links, phase-slip center is determined at narrowest part of link structure. If the length of weak link increases further, the Josephson effect become depairing effect.

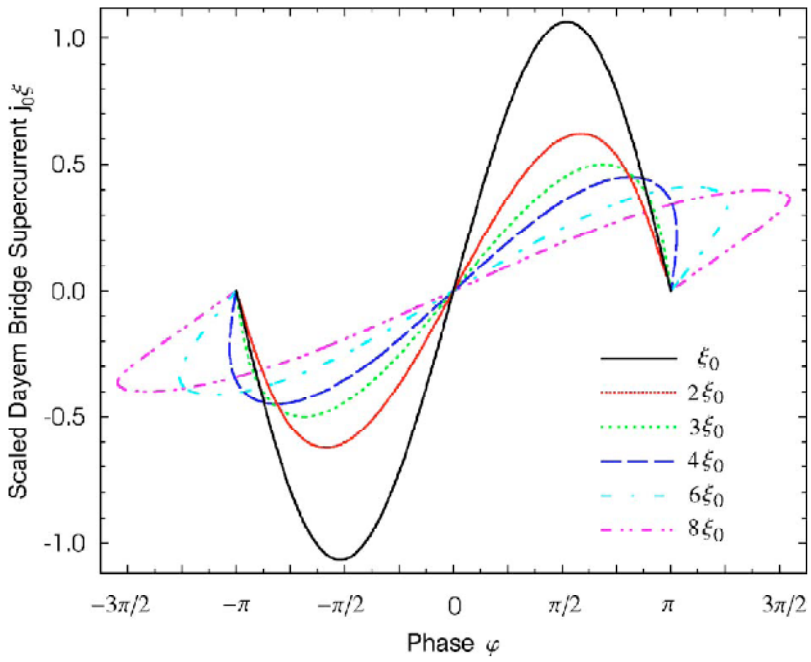

Fig.2.3 Supercurrent-phase relation for Dayem bridge junctions of varying length. The bridge lengths are shown in the diagram with respect to the coherence length [69].

The supercurrent phase relationship moves markedly away from the sinusoidal shape, it still satisfies the three principles defined for Josephson-junction weak-link behavior. As the length is increased up to $8\xi(T)$ the maximum of the supercurrent- phase relationship decreases to a constant value. This constant value is the depairing critical-current density [58, 59].

CPR in Weak Links with Increased Width:

The origin of the current–phase relationship in S-S'-S weak links is dependent on the width of the structures only when the weak link lengths are larger than the critical length $(l_C \approx 3.5\xi(T))$. This dependence was described by Likharev [46] as schematically shown in figure 2.4.

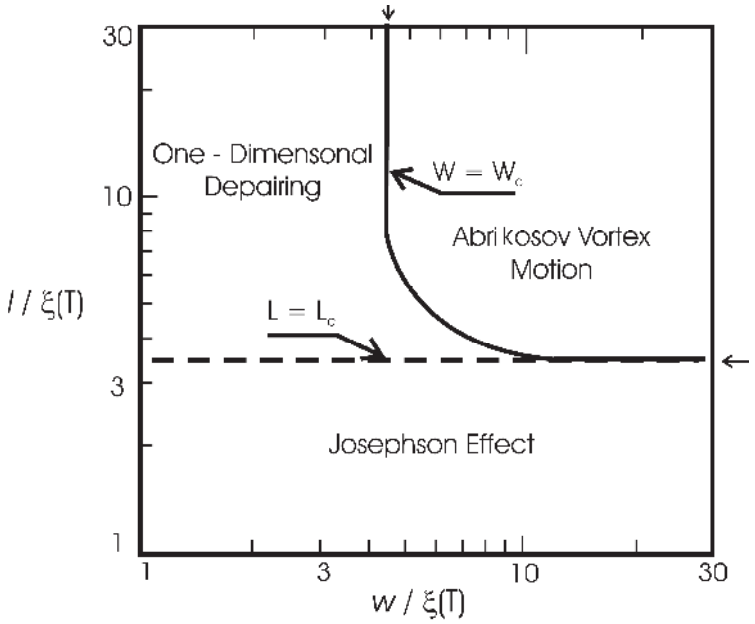

Fig.2.4 The origin of the current–phase relationship in weak links of different dimensions [4].

The physical nature of the current phase relationship in longer bridges $(l_e > 3.49\xi(T))$ depends on the width of the structures.

Bridge Parameters	*Expected CPR related Results*
1] Lengths smaller than 3.49 $\xi(T)$ i.e. $(l_e < 3.49\xi(T))$	Ideal Sinusoidal and single-valued CPR
2] Smaller width than 4.44 $\xi(T)$ i.e. $(w < 4.44\xi(T))$	One dimensional (1D) depairing associated with the nucleation of phase slip centers in the structure.
3] Larger width than 4.44 $\xi(T)$ *but smaller than penetration depth* λ_e *i.e.* $(4.44\xi(T) < w < \lambda_e)$	The coherent motion of vortices allows the growing phase difference across the weak link to relax by multiples of 2π, thus preserving long–range order [5].
4] Wider bridge	Not expected to exhibit coherent vortex motion. Obliviously, no periodic CPR.
5] Effective critical length increase with decreasing width	Vortices cannot exist in the center of strip in width at any length.

2.3 SQUID Based on Nb Dayem Bridges:

The basic working properties of the SQUID based on Nb dayem bridges are well understood [60-68]. The tunnel junctions have low critical current densities which mean that in low inductance limit of the small looped micro SQUID, they do not satisfy criteria of $\beta_L \sim 1$ for optimum performance; whereas the large critical current densities of the dayem bridge junction are suitable to fulfill it.

SQUID based on Nb dayem bridge is ultimate for making local magnetic measurements that can discriminate from the in-plane background magnetic fluctuations and convenient because of its single step fabrication. Although it has two disadvantages:

- They have typical hysteretic current-voltage characteristics;
- They possess relatively low modulation depths in their critical current flux characteristics.

The theory regarding CPR of superconducting bridges i.e. dayem bridges as described earlier are associated to the origin of hysteretic I-V characteristics of the SQUID. In case of all the devices having $\beta_C \leq 1$, the onset of hysteresis is determined by the transition from single to multivalued CPRs in the nanobridges and not by the resistive and capacitive shunts.

The hysteretic characteristics are mainly due to

- Superconducting dayem /nano-bridges exhibiting 1-D depairing
- Phase slippage in structure causes both intrinsic and thermal hysteresis.

I_C - Φ Characteristics as a Function of $L / \xi(T)$ Ratio

The SQUID based on Nb dayem bridges shows non ideal I_C - Φ characteristics which occur because of the dayem bridge properties. A SQUID with nonsinusoidal or multivalued current–phase $I_C(\varphi)$ relationship affects the critical current versus flux interference patterns [69,70], it is due to the dimensions of dayem bridge i.e. $L / \xi(T)$.

Tesche and Clarke [71] predicted that the modulation of critical current is function of $\beta(T) = 2\pi L I_C(T) / \Phi_0$. $\beta(T)$ is depend on inductance (L) and critical current (I_C) where inductance is purely geometric.

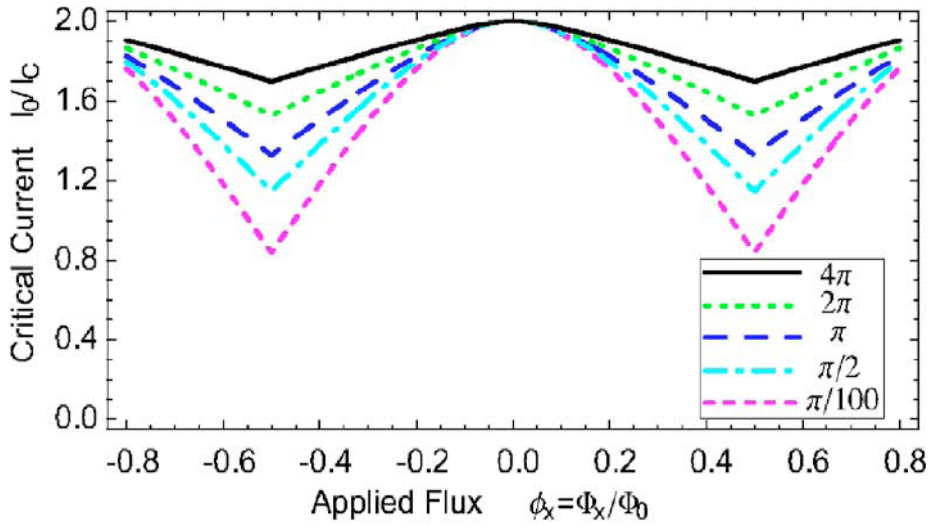

Fig.2.5 The plots of micro-SQUID critical-current oscillations curve correspond to β values of 4π, 2π, π, π/2, and π/100 (in order from top to bottom and represented by the line styles in the digram), which contain Josephson-junction Dayem bridges of length $4\xi_0$ [69]

In case of dayem bridge based SQUIDs, Claassen et al. [66] have explored a fact that the total inductance (L) dominate by contribution of the kinetic inductance of the bridges. The kinetic inductance of the nanobridges spread in the properties of SQUID is given by

$$L_k \approx \frac{1}{\pi}\left[\frac{\Phi_0 \ell}{2\pi I_c \xi(T)}\right] \qquad (2)$$

Where ℓ is bridge length and $\xi(T)$ is temperature dependent coherence length

Hence $\beta(T)$ raised with increasing the bridge length i.e. increasing the ratio $L/\xi(T)$. As discussed in the previous chapter, the increasing $\beta(T)$ diminishes the current modulation. The short coherence length in Nb leads to more highly nonsinusoidal current phase relationship in micro/nano SQUID. Thus the fig 2.5 shows the long dayem bridge and a value of $\beta = 4\pi$ critical current oscillation departs from the sinusoidal shape and becomes more triangular [69, 70].

The similar characteristic was predicted by Hasselbatch [70] using Ginzburg-Landau theory [52]. Their analysis shows that suppression of superconducting order parameter ψ by the reduced dimensions of the nanobridge junctions extend into the SQUID loop and no more confined to the junction. Hence the effective length becomes longer than geometrical one.

If the nanobridge dimensions become larger than critical length, the current modulation significantly diminishes. Further increase in bridge dimensions will demonstrate the triangular oscillation of current with small modulation depth; it is the consequence of nonsinusoidal current phase relationship of longer bridges. This is applicable to micro/nano SQUID based on Niobium due to its short coherence length relative to dayem bridge's effective length which offers larger bridges.

2.4. Techniques to Attach Nano-Particles to Nano-SQUID Sensing Area:

In order to place nanoparticles inside the SQUID, several methods are available. The simplest method consists dispersing the particles in solvent like ethanol by ultrasonication and then placing a drop of this liquid on SQUIDs. After drying the drop, the nanoparticles stick on the chip due to van-der-Waals forces. Flux coupling between SQUID and particle is strong only when a nanoparticle falls on a nanobridge of the SQUID loop. *Atomic force Microscopy* is convenient tool to determine the exact position and shape of the nanoparticles, it is also able to reposition the nanoparticles [1, 74].

In order to improve the flux coupling and to protect the nanoparticles against oxidation, the nanoparticles can directly embed in the nanobridge junction. A laser vaporization and inert gas condensation source may be useful to produce an intense supersonic beam of nanosized particles. It can be deposited in various matrices in UHV conditions [75]. The niobium matrix simultaneously deposited from a UHV electron-gun evaporator, leading to continuous films with a low concentration of embedded clusters [78,76]. These films would be used to pattern planar nanobridge-DC-SQUIDs by electron beam lithography. However, the desired sensitivity can only achieved for clusters embedded in the nanobridges where the magnetic flux coupling is high enough. Indeed they are clearly different in intensity and orientation because of the random distribution of the easy magnetization directions.

A promising *in situ* technique to deposit magnetic molecules onto the SQUID is a *spray (or electrospray) technique*. This method has been used to generate nanoparticles and quantum dots, to deposit ultra-thin films of inorganic, organic and biological materials, to sort nanoparticles according to their sizes, and to help with the dispersion and delivery of nanomaterials.

Another possibility could be the *chemical self assemble monolayer on to the substrate containing devices.* Finally, a novel procedure *combining monolayer self-assembly* with electron beam lithography has developed for attaching ferritin nanoparticles to nano-SQUIDs [2]. After opening a window in the PMMA resist, organic linker molecules are used to attach ferritin to the exposed parts of the gold overlayer of an Nb nano-SQUID. This allows the magnetic nanoparticles to be located optimally as far as magnetic coupling to the nanoSQUID are concerned.

2.5 Spin Sensitivity Simulations:

Here, I have been described the simulation results examined in our research group at ICIB-CNR; the information provided at this point is extremely valuable to optimize the sensor performance in view of most nano-magnetism applications [55].

The study of the magnetic coupling between the nano-objects or spins and the nanoSQUID is very useful for the nanomagnetism applications [79, 11]. In this section, the performances of nanoSQUIDs have been investigated in consideration of their employment in the detection of small spin populations. In particular the magnetic flux output and spin sensitivity of the nanoSQUID are computed for a bohr magneton (single spin) as a function of the position within loop and for the two different configuration of spin clusters with their statistical error contribution.

2.5.1 Simulation Scheme:

Let us consider a single spin or a magnetic nanoparticle having a magnetic moment equal to the Bohr magneton ($\mu_B = 9.3\times10^{-24}\, J/T$) positioned in a generic point $P(x', y', z')$ within a square coil with a side length '*a*' (fig. 2.6). The analysis has been focused on nano-SQUID sensors having a square geometry (with a side length of 200 nm) as the best approximation of the real situation.

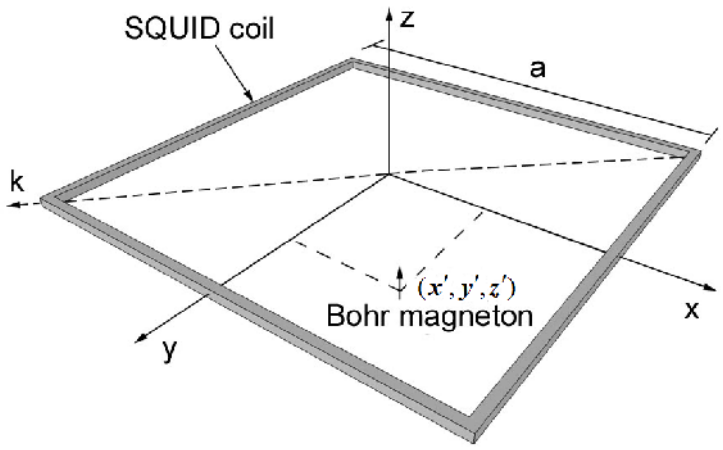

Figure 2.6 Scheme of a square detection coil of a SQUID including a unit magnetic moment (Bohr magneton) located in a generic position of the sensor plane.

We have supposed that the magnetic moment is oriented along the z-axis and its distance from the coil's plane is much smaller than 'a', at least of a ratio z'/a =0.05, so

that the particle can be reasonably considered in the plane of the loop and no field divergence arises in correspondence of the loop edges. In this case, there is no lack of generality since tilting the magnetic moment from a direction normal the coil surface toward a direction parallel to it, there are no contributions to the magnetic flux threading the loop from the magnetic moment components parallel to the plane.

The components of the magnetic vector potential A(r) at position r(x,y,z), relative to a Bohr magneton oriented along the z-direction are:

$$A_x = -\frac{\mu_0 \mu_B}{4\pi}\frac{(y-y')}{r^3}; \qquad A_y = -\frac{\mu_0 \mu_B}{4\pi}\frac{(x-x')}{r^3} \tag{3}$$

Here μ_0 is the magnetic vacuum permeability, and r, the distance between the source and an arbitrary point P(x,y,z), is given by $r = [(x-x') + (y-y') + (z-z')]^{1/2}$.

The total magnetic flux threading the loop is given by:

$$\Phi = \oint_C \vec{A}.d\vec{s} \tag{4}$$

where the integral is considered along the closed line counter C of the SQUID loop.

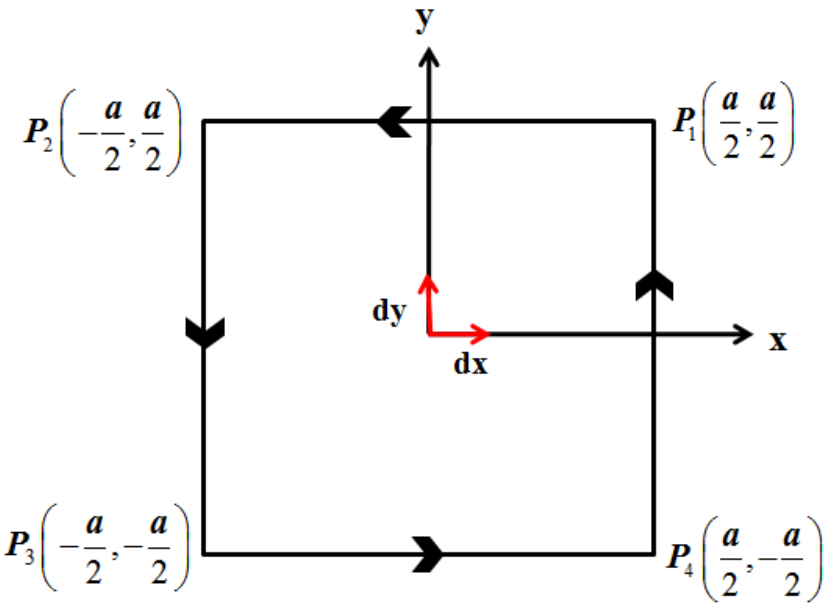

Fig.2.7 The contribution of four sides namely P_1P_2, P_2P_3, P_3P_4, P_4P_1 of square loop to total flux threading loop by considering current moving anticlockwise through loop and it's the boundary conditions.

The flux expression can be simplified as follows

$$\Phi = \oint_C A_x\, dx + A_y\, dy \tag{5}$$

where close contour *C* is consisting of four sides, namely A(P_1P_2), B(P_2P_3),C(P_3P_4), D(P_4P_1) of the loop.

If we introduce the coordinates of the points: $P_1\left(\frac{a}{2},\frac{a}{2}\right)$, $P_2\left(-\frac{a}{2},\frac{a}{2}\right)$, $P_3\left(-\frac{a}{2},-\frac{a}{2}\right)$, $P_4\left(\frac{a}{2},-\frac{a}{2}\right)$; the resultant flux has four contributions, one for each side (as shown in fig. 2.7)

Hence, we can get flux contribution values of a side A (y=a/2, -a/2<x<a/2, Z=0) and a side B (x=a/2, -a/2<y<a/2, Z=0) as follows:

$$A = -\int_{a/2}^{-a/2} dx \frac{(a/2 - y')}{[(x-x')^2 + (a/2 - y')^2 + z'^2]^{3/2}}$$

$$B = -\int_{a/2}^{-a/2} dy \frac{(a/2 + x')}{[(a/2 + x')^2 + (y-y')^2 + z'^2]^{3/2}} \tag{6}$$

Similarly we can obtain the flux contribution values of side C and D as follows.

$$C = +\int_{-a/2}^{a/2} dx \frac{(a/2 + y')}{[(x-x')^2 + (a/2 + y')^2 + z'^2]^{3/2}}$$

$$D = +\int_{-a/2}^{a/2} dy \frac{(a/2 - x')}{[(a/2 - x')^2 + (y-y')^2 + z'^2]^{3/2}} \tag{7}$$

where furthermore the square loop is assumed to lay entirely in the xy plane (z=0).

So, the total flux as function of spin position inside loop is result of flux contributions due to four sides of the loop which can be calculated as:

$$\Phi(x', y', z') = \frac{\mu_0 \mu_B}{4\pi}\{A + B + C + D\} \tag{8}$$

The addition of the integrals (6 and 7) into the eq. (8) and its solution analytically provides the magnetic flux threading the loop produced by a single spin as a function of its position within the loop.

We have performed the solution of integrals by setting the side length of the loop a=200 nm and z'=10 nm as shown in fig. 2.8 predicting the magnetic flux distribution of a Bohr magneton. The resultant figure provides evidence of the magnetic flux stronger dependence with the spin position inside the loop.

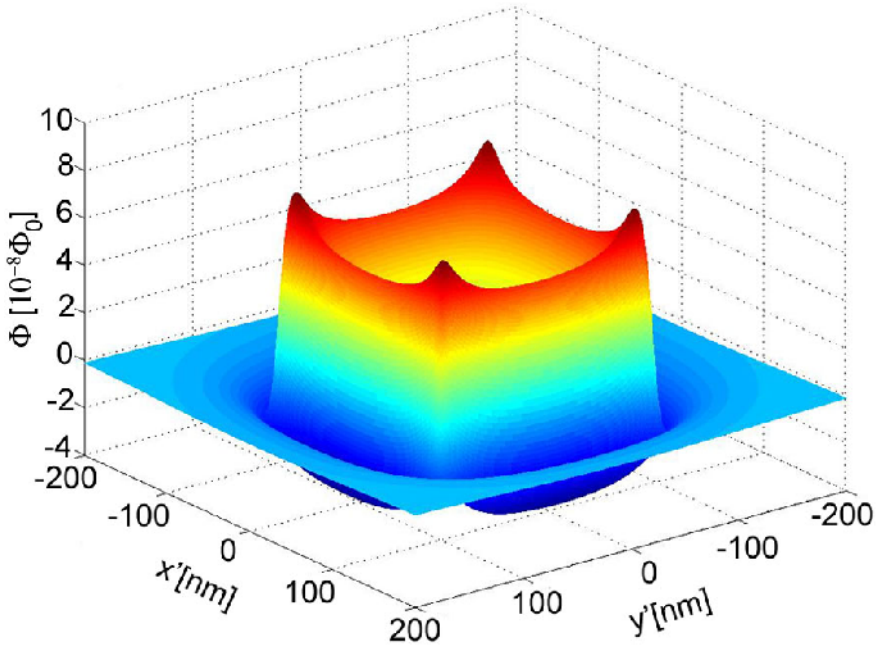

Fig. 2.8 Magnetic flux distribution threading the sensor square loop produced by a single Bohr magneton (spin) as a function of its position within the sensor's capture area. The side length of the loop a=200 nm and the distance of the spin from the sensor plane is z'=10 nm.

It is predicted that the highest values are obtained, when the spins are located close to sensor edges reaching the maximum values close to the corners of the ring. Decreasing the z'value the positions corresponding to the highest values tends toward the edge ring. In the more favorable case, the magnetic flux produced by the single spin (about 0.08 $\mu\Phi_0$) is smaller than the typical flux sensitivity of available nano-SQUIDs (1-2 $\mu\Phi_0$ per band unit in the low frequency regime).

These calculations have been performed neglecting the increase of the flux effective area due to the Pearl penetration depth [80]. For a circular loop, such increase can be approximately evaluated as $A_{eff} = A_g[1+\Lambda(T)/a]^2$ where $\Lambda(T) = \lambda^2(T)/d$ is the two-dimensional Pearls screening length and $\lambda(T)$ is the London penetration depth

[80]. With typical values of loop radius and film thickness employed in nano-SQUIDs fabrication as expressed in the next chapter, the correction factor cannot be neglected. However, this effect does not appreciably affect the behavior of the flux within the sensor loop, so we can consider the area of the sensor under investigation as an effective area. If the spin is positioned at the center of the ring and it lies in the coil's plane (z'=0) the resulting magnetic flux is $\Phi = \mu_0 \mu_B 8\sqrt{2} / (4\pi a)$ which is almost equal (within 4%) to the case of a circular SQUID coil having the same area ($\Phi = \mu_0 \mu_B / 2r$, r is the coil radius) [81].

2.5.2 Magnetic Flux Distribution by Spin Cluster Configuration:

Magnetic flux distributions by spin cluster have been calculated, taking into account the above result of flux distribution as function of single spin position. The flux produced by spin clusters have been evaluated, considering different spin distributions within the SQUID hole. In particular, we have considered two different configurations, one with cluster of spins (up to 500) randomly distributed within the sensor area (configuration A) and another with the same spin numbers having a distribution within a frame of the sensor highest flux value area i.e. located near to the edge of SQUID loop (configuration B).

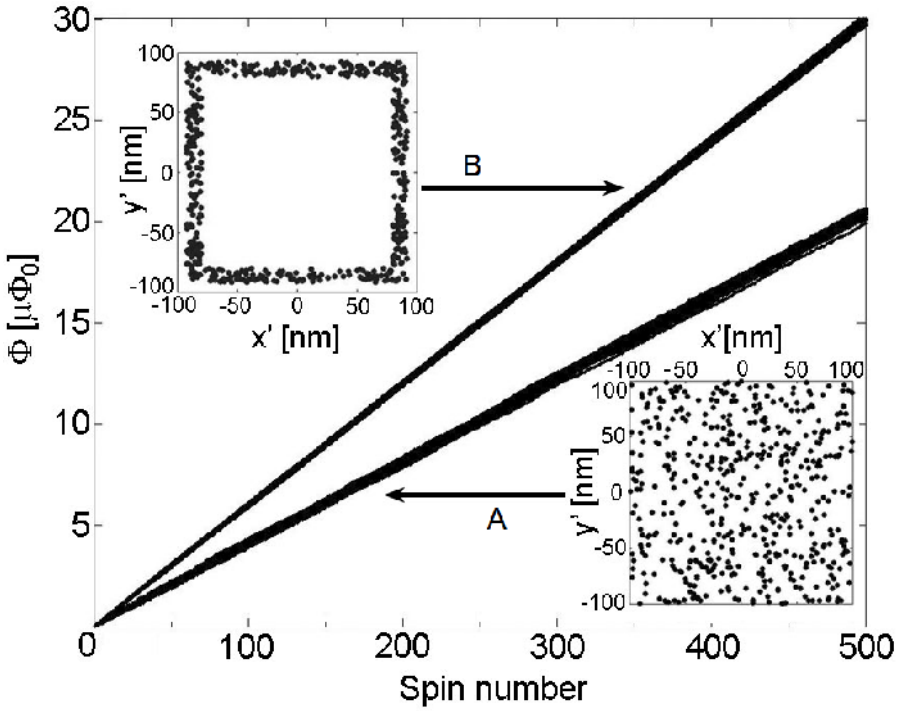

Fig.2.9. Magnetic flux produced by a spin cluster as a function of the spin number, arranged with different random distributions (configurations A and B) within the SQUID hole. The overall magnetic flux has been obtained by summing the flux contributions of each spin.

The insets of fig. 2.9 shows the two different spin distributions taken into account for a cluster of 500 spins. The overall magnetic flux is obtained by summing the flux contributions of each spin. The spatial coordinates of the spins relative to the two configurations have been provided by implementing two suitable random computing functions. As a result of the random nature of both distribution configurations, the spatial coordinate's changes every time that the generating function provides a coordinate's value set. Therefore, since the magnetic flux generated by a single spin depends on its position within the SQUID loop, the overall magnetic flux is expected to change every time and the calculation procedure is repeated. These calculations have been performed for a fixed spin number. The magnetic flux of the both cases as a function of the spin number is reported in fig.2.9.

As expected the magnetic flux corresponding to the edges distribution is higher than the other one, the flux ratio is about 1.5. So, if we are able to locate the magnetic nano-particles along a frame close to the sensor edges, a signal increase of about 50% can be gained. The average magnetic flux corresponding to the single spin for the two configurations (A and B), evaluated from the fig 2.9, is respectively $0.04\,\mu\Phi_0$ and $0.06\,\mu\Phi_0$.

The calculation procedure has been repeated one hundred times for both distribution configurations and the corresponding curves have been plotted in the same graph. This procedure corresponds to repeat the measurements on the same sample using every time a new generated coordinate distribution with a fixed spin number in order to determinate the experimental statistical errors. The thickness of the two curves (see fig. 2.9), are due to the overlapping of the several curves obtained by the iterative procedure. This means that the magnetic flux is affected by a statistical error, which, as evident in the figure 2.9 depends on the number of spin under consideration; in particular it increases as the spin number increases. As expected, the error is higher in the case of random distribution in the whole sensor area which corresponds to higher magnetic flux variations than another one.

This statistical error arises from an uncertain spin number, which can be useful to evaluate. In order to obtain a quantitative estimation of such statistical errors, the standard deviation of the magnetic flux σ_Φ has been computed for both configurations. The σ_Φ is given by the following formula:

$$\sigma_\Phi = \sqrt{\frac{\sum_{i=1}^{M}\left(\Phi_i - \overline{\Phi}\right)^2}{M-1}} \qquad (9)$$

where M is an integer that indicates the number of times the calculation is performed, Φ_i is the flux corresponding to the *i*-calculation and $(\overline{\Phi} = \Phi_1 + \Phi_2 + ... + \Phi_M / M)$ is the average magnetic flux. For each spin number the flux calculation has been repeated one hundred times (M=100).

Using the average magnetic flux corresponding to the single spin, it is possible to evaluate the standard deviation of the spin number σ_N which is reported in fig. 2.10 as a function of the spin number.

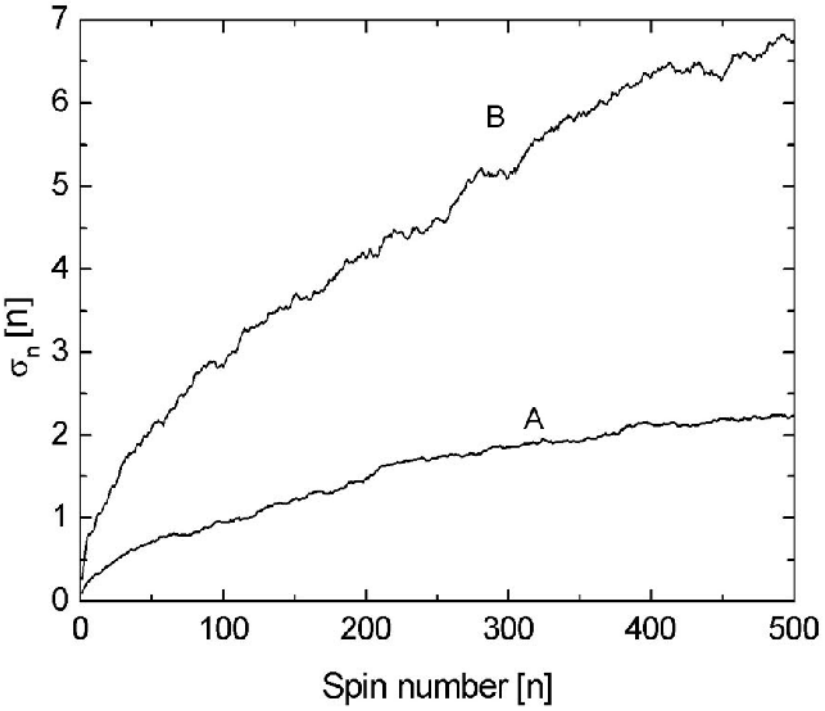

Figure 2.10 Standard deviations of the spin number σ_N, as a function of the spin number corresponding to two different spin arrangement (configurations A and B, shown in the inset of Fig.2.9). For each spin number the flux calculation has been repeated one hundred times.

For both configuration types, the standard deviation increases as the spin number increases, reaching for a cluster of 500 spins a value of about 7.5 and 2.5 spins for the configuration A and B respectively. Such values are comparable with the best spin sensitivity values reported in the literature. Hence, the spin number statistical errors should be taken into a consideration during the measurements performed with the current high sensitive nano-SQUIDs, especially in the case of spins distributed within the whole sensor area and for spin clusters containing a number of spins greater than 500.

2.5.3 Spin Sensitivity:

A relevant figure of merit of a nano-SQUID for the detection of small spin populations is the spin sensitivity or spectral density of the spin noise $S_n^{1/2}$ (the minimum detectable spin number per band unit).

Using the expression of magnetic flux due to the single spin (formula 8) and the spectral density of the flux noise $S_\Phi^{1/2}$, it is possible to obtain $S_n^{1/2}$ as a function of the spin position within the loop as given by

$$S_n^{1/2}(x',y',z') = \frac{S_\Phi^{1/2}}{\Phi(x',y',z')} \qquad (10)$$

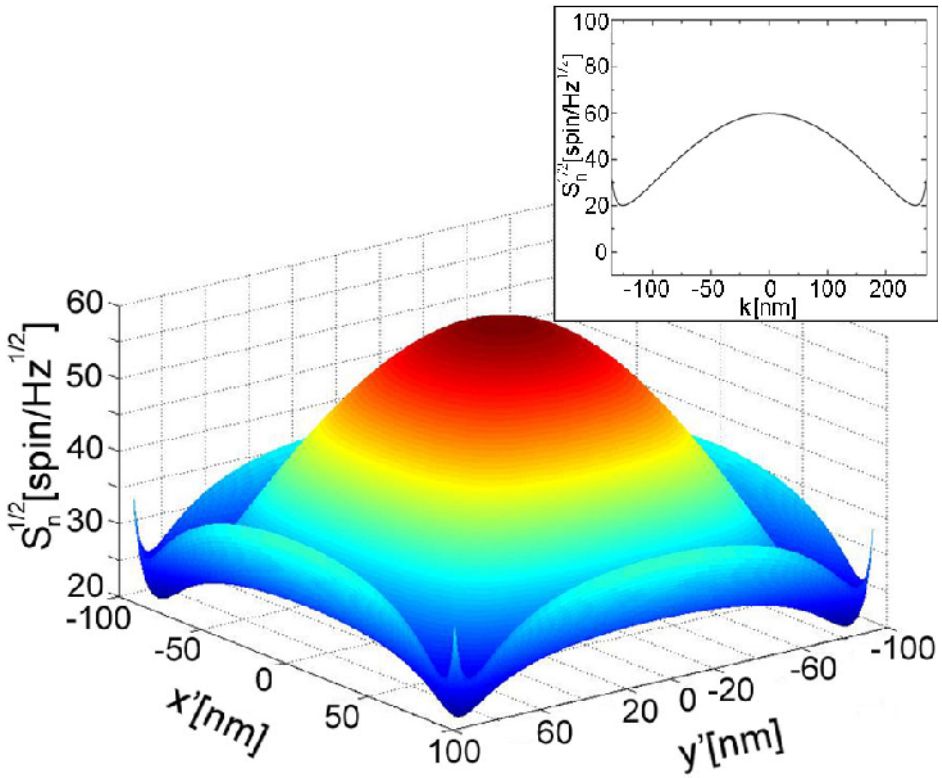

Fig.2.11. Spin noise spectral density $S_n^{1/2}$ of a square nanoSQUID as a function of the position within its loop. The setting parameters are: loop side length a=200 nm, distance of the spin from the sensor plane z'=10 nm and flux noise $S_\Phi^{1/2}$ = 1.5 $\mu\Phi_0 / Hz^{1/2}$. The inset shows $S_n^{1/2}$ computed along a diagonal of the sensor loop.

Fig. 2.11 reports $S_n^{1/2}$ relative to a square nanoSQUID as a function of the position within its loop. The setting parameters are: loop side length a=200 nm, z'=10 nm and flux noise $S_\Phi^{1/2}$ = 1.5 $\mu\Phi_0 / Hz^{1/2}$, which is best experimental value reported in literature by our group as compared to similar size [11]. The presence of a frame within the loop where the sensor is more sensitive, it is evident from figure 2.11.

The ratio between the minimum and the maximum value of the sensor sensitivity is about 3 as evaluated from the inset of the fig 2.11 showing $S_n^{1/2}$ evaluated along a diagonal of the square loop. Such a ratio sensitivity depends on the distance z' of the nano-particles from the sensor plane, in particular it increases as z' decreases. Fig. 2.12 (a) reports the spin noise spectral density $S_n^{1/2}$ of a square nanoSQUID as a function of the position within its loop computed along a diagonal of the sensor loop, calculated for different z values ranging from 10 nm to 35 nm.

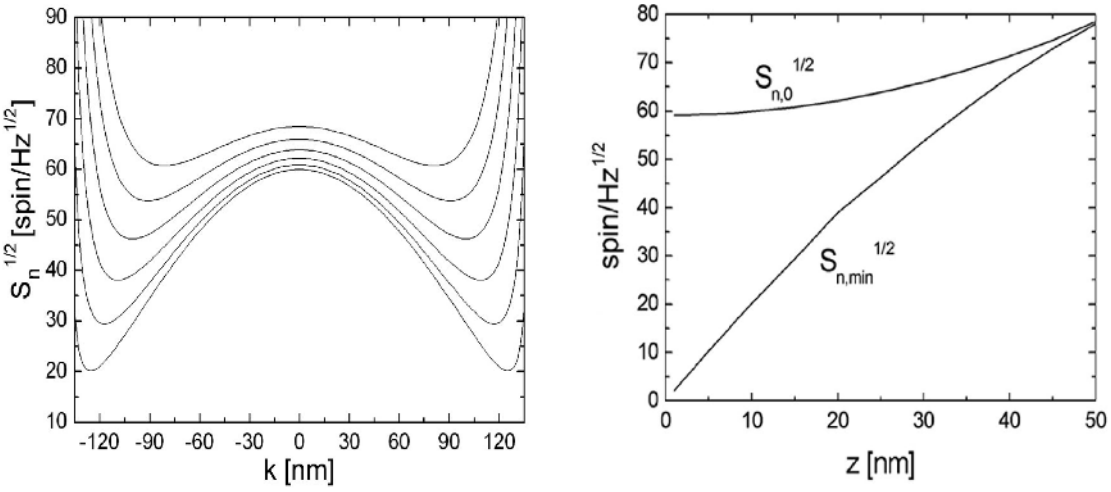

(a) *(b)*

Fig.2.12 (a). Spin noise spectral density $S_n^{1/2}$ of a square nanoSQUID as a function of the position within its loop computed along a diagonal of the sensor loop for different z values. Fig.2.12 (b). Behaviors of the sensitivities $S_{n,\min}^{1/2}$ and $S_{n,0}^{1/2}$ as a function of the distance z', evaluated at its minimum and at the center's sensor respectively.

In the fig. 2.12 (b), the sensitivities $S_{n,\min}^{1/2}$ and $S_{n,0}^{1/2}$ as a function of the distance z', evaluated at its minimum and at the center's sensor respectively, are reported. $S_{n,\min}^{1/2}$ value varies of about two magnitude orders in a z'- range of 50 nm, while $S_{n,0}^{1/2}$ only of a 20%. However, a large spin distance from the sensor plane, the spin sensitivities tend to the same value, indicating that they do not depend any longer on the spin position within the loop sensor.

References

1. Faucher M, Jubert P O, Fruchart O, WernsdorferW and Bouchiat V, *Supercond. Sci. Technol.* 22 064010 (2009)
2. Lam S K H, *Supercond. Sci. Technol.* 22 064005 (2009)
3. Fruchart O, Nozieres J-P, Wernsdorfer W and Givord D, *Phys.Rev.Lett.* 82 1305 (1999)
4. W Wernsdorfer, Supercond. Sci. Techno. 22, 064013, (2009)
5. Mailly D, Chapelier C and Benoit A, *Phys. Rev. Lett.* 70 2020 (1993)
6. Wernsdorfer W. "Micro-SQUID magnetometry to study the magnetisation reversal of single submicronic ferromagnetic particles" *PhD Thesis* Joseph Fourier University,Grenoble. (1996)
7. Lam S K H, *Supercond. Sci. Technol.* 19 963–967 (2006)
8. Troeman A G P, Derking H, Borger B, Pleikies J, Veldhuis D and Hilgenkamp H, *Nano Lett.* 7 2152–6 (2007)
9. Lam S K H, Yang W, Wiogo H T R and Foley C P,*Nanotechnology* 19 285303(2008)
10. Wu C H, Chou Y T, Kuo W C, Chen J H, Wang L M, Chen J C, Chen K L, Sou U C, Yang H C and Jeng J T, *Nanotechnology* 19 315304 (2008)
11. Granata C, Esposito E, Vettoliere A, Petti L and Russo M, *Nanotechnology*-19 275501 (2008)
12. Cleuziou J-P, WernsdorferW, Bouchiat V, Ondarcuhu Th and Monthioux M, *Nat. Nanotechnol.* 1 53 (2006)
13. Hao L, Macfarlane J C, Gallop J C, Cox D, Beyer J, Drung D and Schurig T, *Appl. Phys. Lett.*92 192507 (2008)
14. Troeman A G P, van der Ploeg S H W, IIIchev E, Meyer H-G, Golubov A A, Kupriyanov M Y and Hilgenkamp H, *Phys. Rev.* B 77 024509 (2008)
15. Awschalom D D and Flatt M M, *Nat. Phys.* 3 153–9, (2007)
16. Bogani L and Wernsdorfer W, *Nat. Mater* 73 179–86 (2008)

17. Hanson R and Awschalom D D, *Nature* 453 1043 (2008)

18. Hanson R, Dobrovitski V V, Feiguin A E, Gywat O and Awschalom D D, *Science* 320 352–5 (2008)

19. Rugar D, Budakian R, Mamin H J and Chui B W, *Nature* 430 329 (2004)

20. Wolf S A, Awshalom D D, Buhrman R A, Daughton J M, von Moln`ar S, Roukes M L, Chtchelkanova A Y and Treger D M, *Science* 294 1488 (2001)

21. Ketchen M B, Kopley T and Ling H, *Appl. Phys. Lett.* 44 1008–10 (1984)

22. Kirtley J R, Ketchen M B, Stawiasz K G, Sun J Z, Gallagher W J, Blanton S H and Wind S J, *Appl. Phys. Lett.* 66 115 (1995)

23. Hasselbach K, Veauvy C and Mailly D, *Physica* C 332 140–7 (2000)

24. Mooij J E, Orlando T P, Levitov L, Tian L, van der Wal C and Lloyd S, *Science* 285 1036 (1999)

25. Chiorescu I, Nakamura Y, Harmans C J P M and Mooij J E, *Science* 299 1869 (2003)

26. Rabaud W, Saminadayar L, Mailly D, Hasselbach K, Benoˆıt A and Etienne B, *Phys. Rev. Lett.* 86 3124 (2001)

27. Ketchen M B, Awschalom D D, Gallagher W J, Kleinsasser A W, Sandstrom R L, Rozen J R and Bumble B, *IEEE Trans. Magn.* 25 1212 (1989)

28. Gallop J C, Josephs-Franks P W, Davies J, Hao L and Macfarlane J C, *Physica* C 368 109 (2002)

29. Gallop J, *Supercond. Sci. Technol.* 16 1575 (2003)

30. N´eel L, *Ann. Geophys.* 5 99 (1949)

31. N´eel L, *C. R. Acad. Sci.* 228 664 (1949)

32. Wernsdorfer W, Hasselbach K, Mailly D, Barbara B, Benoit A, Thomas L and Suran G, *J. Magn. Magn. Mater.* 145 33 (1995)

33. Meier F, Levy J and Loss D *Phys. Rev. Lett.* 90 047901 (2003)

34. Francesco Giazotto, Joonas T. Peltonen, Matthias Meschke and Jukka P. Pekola Nature Physics, Vol.-6 DOI: 10.105/NPHYS154 (2010)

35. Wernsdorfer W, Bonet Orozco E, Hasselbach K, Benoit A, Mailly D, Kubo O, Nakano H and Barbara B, *Phys.Rev.Lett.* 79 4014, (1997)

36. Hao L *et al, Supercond. Sci. Technol.* 16 1479–82 (2003)

37. Freitag M, Tsang J C, Kirtely J, Carlsen A, Chen J, Troeman A, Hilgenkamp H and Avouris P, *Nano Lett.* 6 1425–33 (2006)

38. Troeman A G P, Nanosquid magnetometers and high resolution scanning SQUID microscopy *PhD Thesis* University of Twente (2007)

39. Watson A, *Science* 306 1308–9 (2004)

40. Hao L, Macfarlane J C, Gallop J C, Cox D, Hutson D, Josephs-Franks P, Chen J and Lam S K H, *IEEE Trans.Instrum. Meas.* 56 62–5 (2007)

41. Wernsdorfer W and Sessoli R, *Science* 284 133 (1999)

42. Mangin S, Marchal G, Wernsdorfer W, Sulpice A, Hasselbach K, Mailly D and Barbara B, *Europhys. Lett.* 6 675 (1997)

43. B.D. Josephson; Phys. Lett. 1, 251 (1962)

44. P.W. Anderson and A.H. Dayem, *Phys. Rev. Lett. 13, 195 (1964)*

45. W. Anderson and J.M. Rowell; Phys. Rev. Lett. 10, 230 (1963)

46. K.K. Likharev; Rev. Mod. Phys. 51, 101 (1979)

47. A.A. Golubov, M.Yu. Kupriyanov, and E. Il'Ichev; Rev. Mod. Phys. 76, 411 (2004)

48. Lam, S. K. H.; Tilbrook, D. L. *Appl. Phys. Lett*, *82*, 1078-1080 (2003)

49. Bouchiat V, Faucher M, Thirion C, Wernsdorfer W, Fournier T and Pannetier B, *Appl. Phys. Lett.* 79 123–5 (2001)

50. Amit Finkler et al., Nano. Letts. *10*, 1046–1049 (2010)

51. L.G. Aslamazov and A.I. Larkin; *JETP Lett. 9, 87 (1969)*

52. V.L. Ginzburg and L.D. Landau; *Zh. Eksp. Theor. Fiz. 20, 1064 (1950)*

53. K. K. Likharev and L.A. Yakobson; *Zh. Tekhn. Fiz. 45, 1503 (1975) [Sov. Phys. Tech. Phys. 20, 950 (1975)]*

54. S.S. Pei, J.E. Lukens and R.D. Lukens; *Appl. Phys. Lett. 36, 88 (1980)*

55. C. Granata, A. Vettoliere, P. Walke, C. Nappi and M. Russo, *Journal of Applied Physics*-106, 023925 (2009) Also published in *Virtual Journal of Application of Superconductivity* Vol.17, Iss.3 (1st Aug.09)

56. I.O. Kulik and A.N. Omelyanchuk; Pis'ma *Zh. Eksp. Teor. Fiz. 21, 216 (1975) [JETP Lett. 21, 96 (1975)]*

57. M.C. Koops, G.V. van Duyneveldt and R. De Bruyn Ouboter; *Phys. Rev. Lett. 77, 2542 (1996)*

58. M.Yu. Kupriyanov and V.F. Lukichev; *Fiz. Nizk. Temp. 7, 281 (1981) [Sov. J. Low Temp. Phys. 7, 14 (1981)*

59. A.G.P. Troeman et.al, *Phy. Rev. B 77, 024509 (2008)*

60. Jamet, M.; Wernsdorfer, S.; Thirion, C.; Mailly, D.; Dupuis, V.; Me´linon, P.; Pe´rez, A. *Phys. Re*V. *Lett*., *86*, 4676-4769 (2000)

61. Gallop, J.; Josephs-Franks, P. W.; Davies, J.; Hao, L.; MacFarlane, J. *Phys. C*, *368*, 109-113 (2002)

62. Dechert, J.; Krischker, K.; Go¨ddenhenrich, T.; Mu¨ck, M.; Heiden, C. *IEEE Trans. Appl. Supercond.*, *7*, 3143-3146 (1997)

63. Hasselbach, K.; Veauvy, C.; Mailly, D., *Phys. C, 332*, 140- 147 (2000)

64. Veauvy, C.; Hasselbach, K.; Mailly, D. *Re*V. *Sci. Instrum*., *73,*525-530 (2002)

65. Voss, R. F.; Laibowitz, B.; Ketchen, M. B.; Broers, A. N. *Superconducting Quantum Interference De*V*ices and Their Application*; Hahlbohm, H. D., Luebbig, H., Eds.; de Gruyter: New York, pp 365-50 (1980)

66. Claassen, J. H. *Appl. Phys. Lett*, *40*, 86-841 (1982)

67. Dilorio, M. S.; de Lozanne, A.; Beasley, M. R. *IEEE Trans. Magn.*, *MAG-19*, 308-311 (1983)

68. Rogalla, H.; David, B.; Ru¨hl, J., *J. Appl. Phys. 55*, 141-143.(1984)

69. G. J. Podd, G. D. Hutchinson, D. A. Williams, and D. G. Hasko, Phy. Rev. B 75, 11501 (2007)

70. K. Hasselbach, D. Mailly, and J. R. Kirtley, J. Appl. Phys. 91, 4432 (2002).

71. C. D. Tesche and J. Clarke, J. Low Temp. Phys. 29, 301 (1977)

72. P. Carelli, M. G. Castellano, K. Flacco, R. Leoni and G. Torrioli, Europhys. Lett., 6 (5), pp. 569-574 (1997)

73. V. Bouchiat, Superc. Sci. Technol., 22 064002 (2009)

74. Thess A *et al, Science* 273 483–5 (1996)

75. Gerdes S, Ondarcuhu T, Cholet S and Joachim C, Europhys. *Lett.* 48 292 (1999)

76. Javey A, Guo J, Wang Q, Lundstrom M and Dai H, *Nature* 424 654–7,(2003)

77. Mensah S L, Prasad A, Wang J and Yap Y K, *J. Nanosci. Nanotechnol.* 8 233–6 (2008)

78. T. A. Fulton, L. NN. Dunkleberger, and R. C. Dynes, Phys. Rev. B 6, 855 (1972)

79. A. Barone and G. Paterno, *Physics and Applications of the Josephson Effect* - Wiley, New York, p. 200 (1982)

80. D. L. Tilbrook, Superc. Sci. Technol., 22 064003 (2009).

81. L. Hao, J. C. Mcfarlane, J. C. Gallop, E. Romans, D. Cox, D. Hutson, and J. Chen, IEEE Trans. Appl. Supercond. 17, pp.742-745 (2007)

CHAPTER 3

Nanoscale DC-SQUID Fabrication

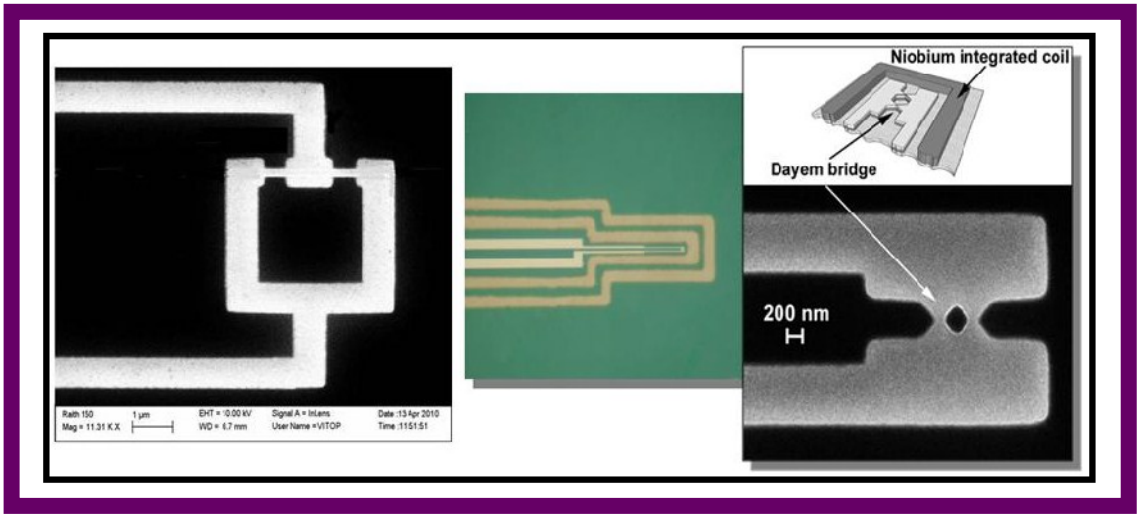

This chapter is devoted to fabrication technology used to fabricate convenient nanoscale SQUID device. The geometry of the device has high impact on its performance as described in the previous chapter. To fulfill the requirements for practical application towards small spin detection as well as nanomagnetism, the processes based on e-beam lithography have been used. Concerning e-beam lithography few important issues like its resolution; proximity effect with some possible corrections has been reported. Also the brief overview of DC-magnetron sputtering for thin film deposition, lift off, reactive ion etching process are presented. Successful fabrication process of two kinds of devices has been reported namely a single niobium layer device and niobium-aluminum bilayer device.

3.1 General Aspect of Electron Beam Lithography:

Current nanoscale device fabrication makes use of many techniques like electron beam lithography, optical lithography, ion beam lithography, x-ray lithography etc. The all kinds of the lithography work in similar manner despite what type of material or radiation is used. Each of these methods has advantages and disadvantages. Lithography has the advantage of being able to repeatedly create the same pattern by using the same mask. The resolution of the lithography is limited by the resolution of the mask, the wave size of the beam and the resolution capacity of the resist used.

The Electron beam lithography (EBL) is the best resolution technique among all lithographic techniques, which can create pattern of the 10-20nm resolution. Cumming et al. used e-beam lithography techniques to create nano-wires with width of 10 to 20nm, depending on the material of the wire. He has designed a technique to create 3nm width wires, cited by Guinness Book of World Records as the world's smallest wire [1]. However, these wires are limited in length and have a low yield of creation (3%). Ion beam and x-ray lithography both have resolutions on the order of 50 to 100nm, but are similar to electron beam lithography in most other respects.

In this chapter, brief introduction of the technological tools especially electron beam lithography and associated fabrication methods used for the nanoscale SQUID device are described.

3.1.1 Technical Electron Beam Lithography Set-Up:

A typical commercial EBL system including the column, chamber and control electronics is shown in the fig. 3.1. Underneath the column is a chamber containing a stage in order to move the sample around and services for loading and unloading the samples. A vacuum system associated with the chamber is required to maintain an appropriate vacuum level throughout the machine and also during load and unload cycles. A set of control electronics supplies power and signals to various parts of the machine. Finally, the system is controlled by the computer, which handles such diverse functions as setting up an exposure job, loading and unloading the sample, aligning and focusing the electron beam and sending pattern data to the pattern generator [2].

The Column is referred as the part of the EBL system that forms the electron beam. The EBL column typically consists of an electron source, two or more lenses, a mechanism for deflecting the beam, a blanker for turning the beam on and off, a stigmator for correcting any astigmatism in the beam, aperture for helping to define the beam, alignment systems for centering the beam in the column, and finally, an electron detector for assisting with focusing and locating marks on the sample. The optical axis is parallel to the electron beam and X and Y are parallel to the plane of the sample.

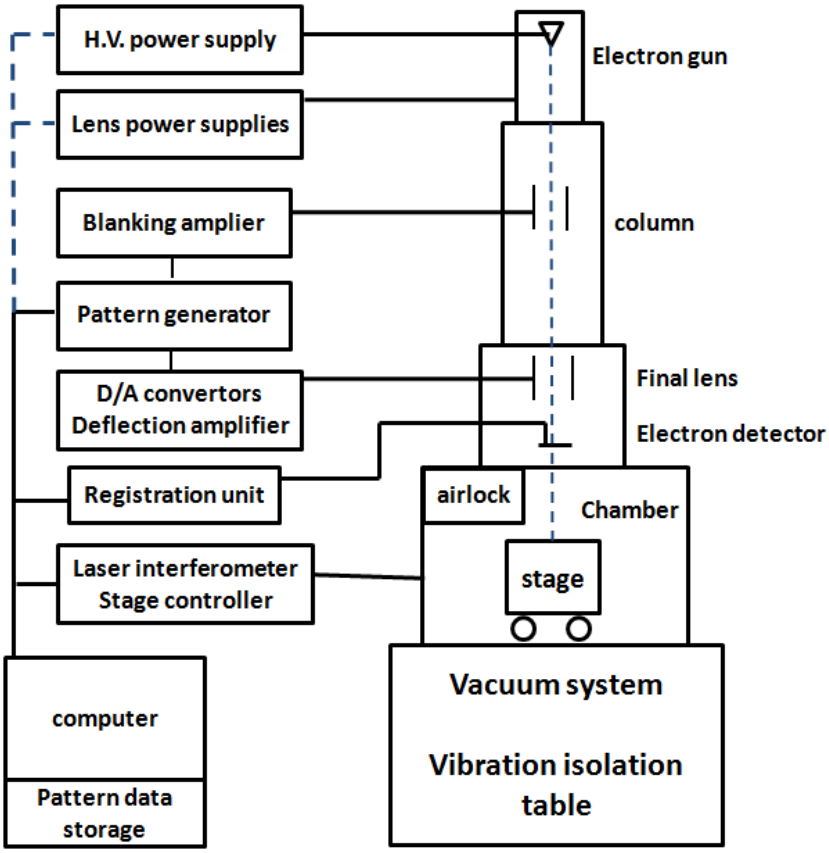

Fig. 3.1 Block diagram showing the major components of a typical electron beam lithography system.

Electron Sources: Emission of electrons from the conducting material can be achieved either by heating in to the point where the electrons have sufficient energy to overcome the work function barrier of the conductor (thermionic sources) or by applying an electric field sufficiently strong that they tunnel through barrier (field emission sources). The important parameters of the source are the source size, its brightness and the energy spread of the emitted electrons. The size of the source determines the amount of demagnification that has to be applied to have small spot at the target. The beam brightness is equivalent to intensity in conventional optics. A beam with a wide energy spread is similar to white light, while a beam with the narrow energy spread would be comparable to monochromatic light. The energy spread of the source is important corresponding to space charge interactions between electrons which further increases the energy spread of the beam as it moves down to the column. Usually, an electron source has two or more electrodes to control the emission properties. Table 2.1 summarizes the properties of the common sources.

Source Type	Brightness $(A/cm^2/sr)$	Source size	Energy spread (eV)	Vacuum required (Torr)
Tungsten thermionic	$\sim 10^5$	~ 25'	2-3	10^{-6}
LaB_6	$\sim 10^6$	~ 10'	2-3	10^{-8}
Thermal Field Emission (like heated W/ZrO_2)	$\sim 10^8$	$\sim 20nm$	0.9	10^{-9}
Tungsten & cold field emission	$\sim 10^9$	5nm	0.22	10^{-10}

Table 2.1 The properties of the electron sources commonly used in EBL tools.

Electron Lenses: Electron can be focused either by electrostatic forces or magnetic forces. Generally the electron lenses can be made only to converge, no diverge, except in some special cases. In term of aberrations, electron lenses have poor quality than optical lenses which restricts the field size and the convergence angle (or numerical aperture) that can be used. The spherical and chromatic aberrations are critical to EBL which can be minimized by reducing the convergence angle of the system so the electrons are confined to the center of the lenses, at the cost of greatly reducing beam current.

A magnetic lens consists of two circularly symmetric iron (or some other high permeability material) polepieces with the copper winding in-between. In focusing action, the divergence of the magnetic flux along the optical axis imparts a force on the electrons back towards the optical axis. The magnetic field causes a rotation of the electrons (and the image) about Z axis in a corkscrew fashion which does not affect the performance of the lens. But it does impact the design, alignment and operation of the system.

The electrostatic lenses usually produce higher aberrations, therefore magnetic lens are preferred to focus the beam. They are most often found in gun region as a condense lens consists of three consecutive elements like aperture, the outer two being at the ground potential and the inner at some other potential that controls the lens strength. The electric potentials set up by such a lens are liable to drag an electron back towards the axis which is traveling away from the optical axis, resulting in the focusing action.

Other optical elements include aperture, deflection systems, alignments coils, blanking plates and stigmators.

Aperture: The holes through which the beam transverses along the column are called apertures. There are several types of apertures. A beam limiting aperture has two effects, it sets the beam convergence angle [α] (measured as the half-angle of the beam at the target) through which electrons can pass through the system, controlling the effect of lens aberrations and thus resolution, and also sets the beam current. A beam limiting aperture is normally set in an X-Y stage to allow it to be centered, or aligned, with respect to the optical axis. It is best to have a beam limiting aperture as close to the gun as possible to limit the effects of space charge caused by electron - electron repulsion.

Apertures may be heated to help prevent the formation of contamination deposits, which can degrade the resolution of the system. Shaped beam systems also have one or more shaping apertures, which can be square or have more complicated shapes to allow the formation of a variety of beam shapes, such as triangles, etc.

Electron Beam Deflection: Deflection of the electron beam is used to scan the beam across the surface of the sample. As with lenses, it can be done either magnetically or electrostatically. The coils or plates are arranged so that the fields are perpendicular to the optical axis. Deflecting the beam off axis introduces additional aberrations that cause the beam diameter to deteriorate, and deviations from linearity in X and Y increase as the amount of deflection increases. These effects limit the maximum field or deflection size that can be used. As with lenses, magnetic deflection introduces fewer distortions than electrostatic deflection. However, electrostatic deflection can achieve much higher speeds. Some tools use multiple deflection systems, where high speed, short range deflection is done electrostatically while long range deflection is magnetic. In either case, the field size of the tool is limited by aberrations of the deflection system; some tools introduce dynamic corrections to the deflection, focus, and stigmators in order to increase the maximum field size, at the cost of additional complexity.

Beam Blanking: Blanking (or turning the beam on and off) is usually accomplished with a pair of plates set up as a simple electrostatic deflector. One or both of the plates are connected to a blanking amplifier with a fast response time. To turn the beam off, a voltage is applied across the plate which sweeps the beam off axis until it is intercepted by a downstream aperture. The blanking is arranged to be conjugate, so that the beam at the target does not move in first order while the blanking plates are activated. Otherwise, the beam would leave streaks in the resist as it was blanked. The simplest way to ensure conjugate blanking is to arrange the column so that the blanking plates are centered at an intermediate focal point, or crossover. In very high speed systems, more elaborate blanking systems involving multiple sets of plates and delay lines may be required to prevent beam motion during the blanking and unblanking processes [3].

Stigmatiors: A stigmator is a special type of lens used to balance for imperfections in the creation and alignment of the EBL column. These imperfections can result in astigmatism, where the beam focuses in different directions at different lens settings. As a result, the oblong shape creates due to beam rounding and the direction of the principal axis dependent on the focus setting forms smeared images in the resist. The stigmator cancels out the effect of astigmatism by recovering beam to its optimum shape. Stigmators may be either electrostatic or magnetic and consist of four or more poles (eight is typical) arranged around the optical axis. They can be made by changing the connections to a deflector. With appropriate mixing of the electrical signals, a single deflector may sometimes perform multiple functions, including beam deflection, stigmation, alignment, and blanking.

Other Column Components: A number of other components can be found in the column. They are irrelevant to the electron optics, however are significant to the system operation. In order to ensure the correct dose for resist exposure, a Faraday cage located below the final beam limiting aperture is used to measure the beam current. The column will have an isolation valve that allows the chamber to be vented for maintenance while the gun is still under vacuum and operational. All parts of an electron beam column exposed to the beam must be conductive or charging will cause unwanted displacements of the beam.

Finally, the system needs a method of detecting the electrons for focusing, deflection calibration, and alignment mark detection. Usually this is a silicon solid state detector similar to a solar cell, mounted on the end of the objective lens just above the sample. Channel plate detectors and scintillators with photomultiplier tubes may also be used. Unlike scanning electron microscopes, which provide image with low voltage secondary electrons, EBL systems normally detect high energy backscattered electrons since these electrons can more easily penetrate the resist film. The signal from low energy secondary electrons may be obscured by the resist.

3.1.2 Electron Interaction with Matter:

Although EBL tools are capable of forming tremendously fine probes, things become more complex as soon as the electrons hit the substrate. Since the electrons penetrate the resist, many small angle scattering measures (forward scattering), which tend to broaden the initial beam diameter. Also the electrons penetrate through the resist into the substrate, they occasionally undergo large angle scattering actions (backscattering). The backscattered electrons cause the proximity effect [4] where the dose that a pattern feature receives is affected by electrons scattering from other features nearby. During this process the electrons are continuously slowing down, producing a cascade of low energy electrons called secondary electrons.

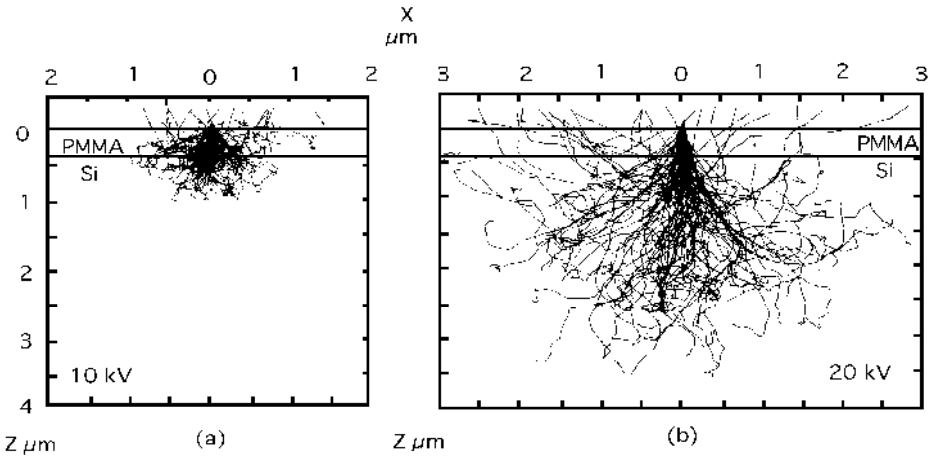

Fig.3.2 Monte Carlo simulation of electron scattering in resist on silicon substrate at a) 10 kV and b) 20 kV

Electron scattering in resists and substrates can be modeled with reasonable accuracy by assuming that the electrons continuously slow down as described by the Bethe equation [5], while undergoing elastic scattering, as described by the screened Rutherford formula [6]. Since the different materials and geometries make analytic solutions difficult, Monte Carlo techniques where a large number of random electrons simulation is commonly used. The ideal simulation of e-beam scattering in 100 nm thin PMMA resist on Si substrate is shown in fig.3.2.

Forward Scattering: When the electrons penetrate the resist, some fraction of them will undergo small angle scattering giving raises to a significantly broader beam profile at the bottom of the resist than at the top. The increase in effective beam diameter (in nanometers) due to forward scattering is given by the formula $d_F = 0.9(R_T / V_B)$ where R_T is the resist thickness in nanometers and V_B is the beam voltage in kilovolts. Forward scattering is minimized by reducing the resist thickness and the highest accelerating voltage.

It is better to avoid forward scattering effects though in some instances they may be used to advantage. It is possible to tailor the resist sidewall angle in thick resist by adjusting the development time [7]. As the time increases, the resist sidewall profile will go from a positive slope, to vertical, and eventually to a negative, or retrograde, profile, which is especially desirable for pattern transfer by liftoff.

Backward Scattering: Since the electrons continue to penetrate through the resist into the substrate, many of them will experience large angle scattering events. These electrons can return back through the resist at a significant distance from the incident beam, causing additional resist exposure. This is called the electron beam proximity

effect. The range of the electrons (a distance traveled by electron in the bulk material before losing all its energy) depends on both the energy of the primary electrons and the type of substrate.

The fraction of electrons that are backscattered, *e*, is roughly independent of beam energy, although it does depend on the substrate material, with low atomic number materials giving less backscatter. Typical values of *e* range from 0.17 for silicon to 0.50 for tungsten and gold. Experimentally, *e* is only loosely related to e_e, the backscatter energy deposited in the resist as modeled by a double Gaussian. Values for e_e tend to be about twice *e*.

3.1.3 Resolution Capability:

Electron beam widths can routinely go down to a few nm or atomic level which is mainly limited by aberrations and space charge. There are several factors that determine the resolution of an electron beam system.

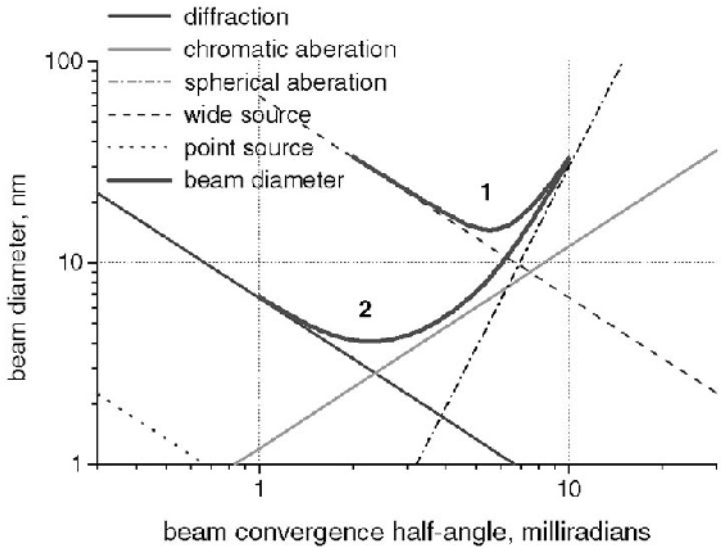

Fig.3.3 Diameter of the electron-beam lithographic tools as a function of beam-convergence half angle. 1: Wide source. 2: Point source. E_0 = 50 keV, ΔE = 1.5 eV, C_c = 40 mm, C_s = 60 mm.

The resolution can generally be improved by using small beam limiting aperture, at expense of reduced beam current as well as increasing demagnification. Fig. 3.3 shows the source contribution in typical column. In the system with thermionic sources, spherical aberrations tend to be the limiting factor for the beam diameter, while chromatic aberrations dominate in field emission system. For given beam current, optimum combination of convergence angle and system demagnification occurs. However, the feature resolution limit is determined not only by the beam size but also

by forward scattering (or effective beam broadening) in the photoresist while the pitch resolution limit is determined by secondary electron travel in the photoresist. The higher energy electrons or thinner photoresist may decrease the forward scattering, but the generation of secondary electrons is inevitable.

Resolution can generally be improved in most systems by using a smaller beam limiting aperture, at the expense of reduced beam current and throughput. In systems where the demagnification can be varied, increasing the demagnification will also improve resolution, at the expense of reduced beam current.

3.1.4 Proximity Effect:

As discussed the net result of the electron scattering in the previous section, the dose delivered by the electron beam tool is not confined to the shapes that the tool writes, resulting in pattern specific linewidth variations known as the proximity effect. For example, a narrow line between two large exposed areas may receive so many scattered electrons. Hence a small isolated feature may lose its dose due to scattering results by incomplete patterning.

Many different schemes have been formulated to minimize the proximity effect. If a pattern has fairly uniform density and linewidth, all that may be required is to adjust the overall dose until the patterns come out in the proper size. Using higher contrast resists can help minimize the linewidth variations. Multilevel resists, in which a thin top layer is sensitive to electrons and the pattern developed in it is transferred by dry etching into a thicker underlying layer, reducing the forward scattering effect, at the cost of an increase in process complexity.

Higher beam voltages (from 50 kV to 100 kV or more) also minimize forward scattering, although it can increase the backscattering [9]. Conversely, by going to very low beam energies, where the electron range is smaller than the minimum feature size, the proximity effect can be eliminated [10]. The defect is that the thickness of a single layer resist must also be less than the minimum feature size so that the electrons can expose the entire film thickness. The electron-optical design is much harder for low voltage systems since the electrons are more difficult to focus into a small spot and are more sensitive to stray electrostatic and magnetic fields [11]. A technique that can be used in conjunction with this approach in order to increase the usable range of electron energy is to place a layer with a high atomic number, such as tungsten, underneath the resist. This has the effect of further limiting the range of the backscattered electrons.

The most common technique of proximity correction is dose modulation, where each individual shape in the pattern is assigned a dose such that (in theory) the shape prints at its correct size. The calculations needed to solve the shape-to-shape interactions are computationally very time-consuming. Although the actual effect of electron scattering is to increase the dose received by large areas, for practical reasons proximity correction is normally thought of in terms of the large areas receiving

a base dose of unity, with the smaller and/or isolated features receiving a larger dose to compensate.

Fig.3.4 Picture of Raith E-beam system available in (CNR-ICIB) Institute of Cybernetics, CNR, NA, Italy

PARAMETERS of RAITH e-Beam system	
Electron Source	Thermal Field emitter ZrO/W
Beam Energy Range	200 eV to 30 keV
Beam Current Range	5pA-5nA
Beam Size	1.6 nm @ 20kV and 2.5nm@1kV
Step Size	Minimum 1nm
Writing Speed	2Hz to 10MHz pixel
Exposure of all type of arbitrary shaped area in fast vector scan mode with singe pixel lines and dot arrays.	

Table 3.2 The parameters of electron beam system used in ICIB-CNR.

3.2 Design Norm and Circuit Layout:

Prior to design SQUID device, one should consider the geometrical parameters which affects on device performance. As discussed in the earlier chapter, the bridge dimension dependence CPR characteristics plays key role [11, 17]. Considering the Josephson bridge design, it should be taken into account that the current modulation depth of a bridge-based SQUID increases by decreasing the ratio between the bridge length l and the film coherence length $\xi(T)$ at T = 0 K [11].

We have used niobium as material of choice for device because of its high critical temperature. The limitation of using niobium is its short coherence length which put restriction on size of the junction. We have designed and fabricated both hysteretic and non hysteretic devices. The hysteretic current voltage characteristics of SQUID based on a Nb nanobridges are occur either due to thermal hysteresis where the energy dissipated in the nanobridge which heats the entire SQUID loop [12,14] or the phase slippage of the superconductor order parameter in the structure [13]. To overcome this difficulty, either a normal-metal thin film acting as a shunt resistor is deposited onto the Nb film [15-17] or the SQUID critical current is lowered in order to obtain a single-valued CPR [13]. Here we have used first consideration to produce non-hysteretic device by using Al thin film as shunt resistor. So, due to two thin layers one over other it may called bilayer device.

Large coils around SQUID to supply magnetic fields for the device calibration and to identify the flux state of the sensor insufficient to fulfill the requirements, due to the occurrence of Joule heating of the coil. Therefore integrated superconducting coil very close to sensor in order to modulate, tune and operate at its high resposivity point has been introduced. The integrated coil shows a high mutual inductance for effective characteristics.

The superconducting loop has been created in a washer shape in order to enhance the heat dissipation during the working operations when the sensor is current biased in resistive mode. We have designed washer in two configurations such as parallel and series where parallel configuration achieved by insertion of two junction in same side of SQUID loop (see fig.3.8 (a)) and series configuration is achieved by arranging two junctions on two parallel sides (see fig.3.8(b)). Furthermore, we have fabricated hysteretic device i.e. single niobium layer device containing washer in parallel configuration (as shown in fig.3.14), as well as non-hysteretic device i.e. bilayer niobium-aluminum device contain washer in series configuration (see in fig. 3.12). In the bilayer/ non-hysteretic device, the nano-junctions constitute the two lateral arms of the loop; therefore the SQUID structure is quite different with respect to a standard series configuration of washer loop, where the Josephson junctions are located on the

outer edge of the square loop, away from the higher field region at the center square hole [17, 18].

The total inductance turns out to be same for both configurations though the noise parameters of both configurations are considerable. The parasitic capacitance in parallel configuration is four times larger than series configuration. Furthermore large washer opening in parallel configuration significantly increase flux capture area of the SQUID. This means large screening current may lead to flux trapping in junctions contributes to noise in SQUID. The flux capture area in series configuration is small, leads less susceptible to flux trapping. The small size of loop, small thickness and the narrow lines or junctions make SQUID insensitive to flux trapping and field penetration.

The layout of whole device as shown in fig. 3.5 consisting of integrated coil [fig.3.6)] and nanoSQUID has been developed in CNR-ICIB. A good compromise is reached using dimensions length and/or width and thickness of the bridge ranging from 50 to 150nm and 20 to 50nm respectively incorporated into device having various loop diameters ranging from 200 nm to 2μm.

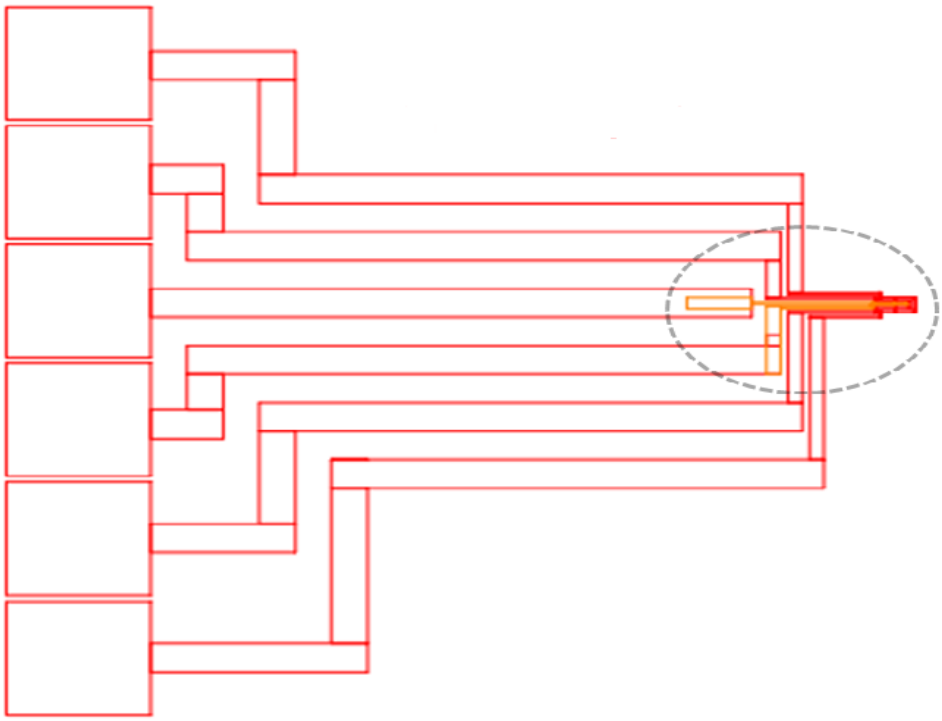

Fig.3.5 Layout out of the complete SQUID illustrates area below circle (yellow color) is sensitive region where SQUID loop is located with dayem nanobridges surrounded by (Dark red color region) integrated coils. Rest of the part is wiring and contact pads.

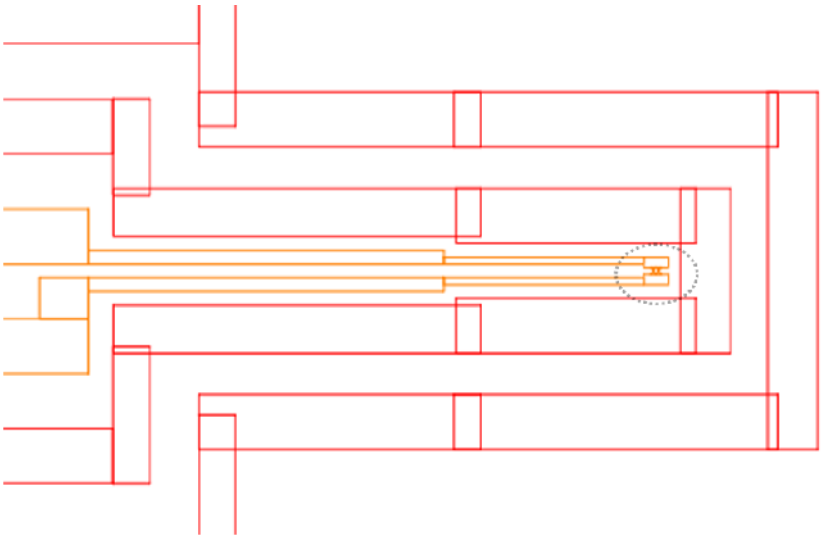

Fig.3.6 The maximized circled area in fig.3.5 shows the layout of SQUID loop with dayem bridges (yellow color) illustrated under blue circle surrounded by (red color) integrated coils.

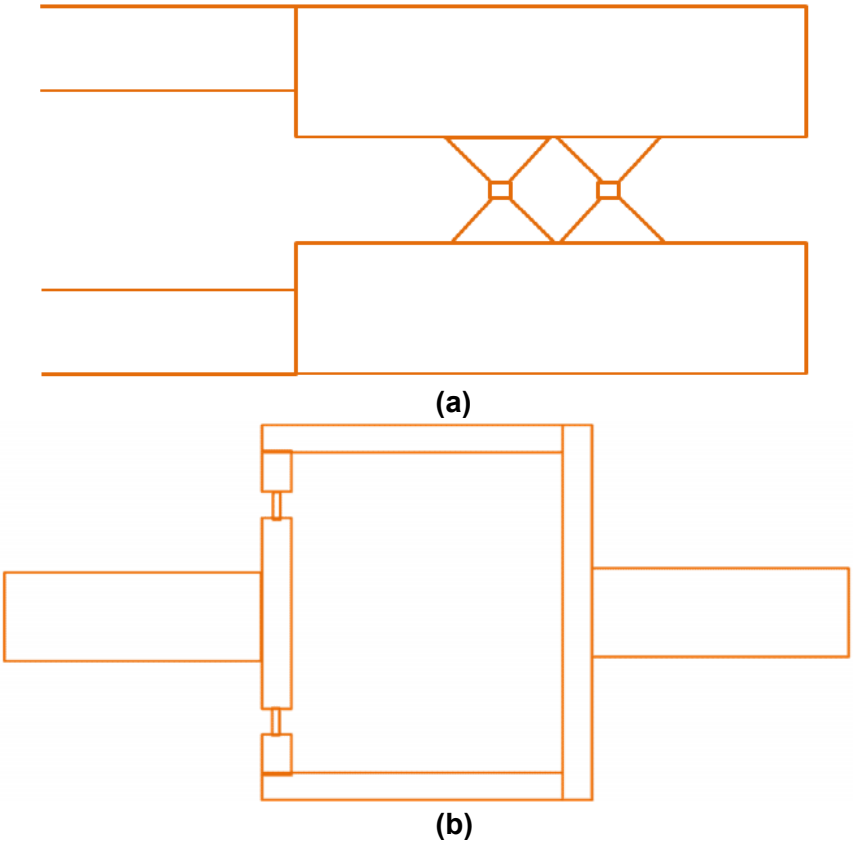

Fig.3.7 The maximized part of circled area of fig.3.6 contains (a) either upper part shows series configuration washer shape loop or (b) lower part shows parallel configuration washer loop where two dayem nanobridges located on same arms of SQUID.

Fabrication Process of Bilayer Device:

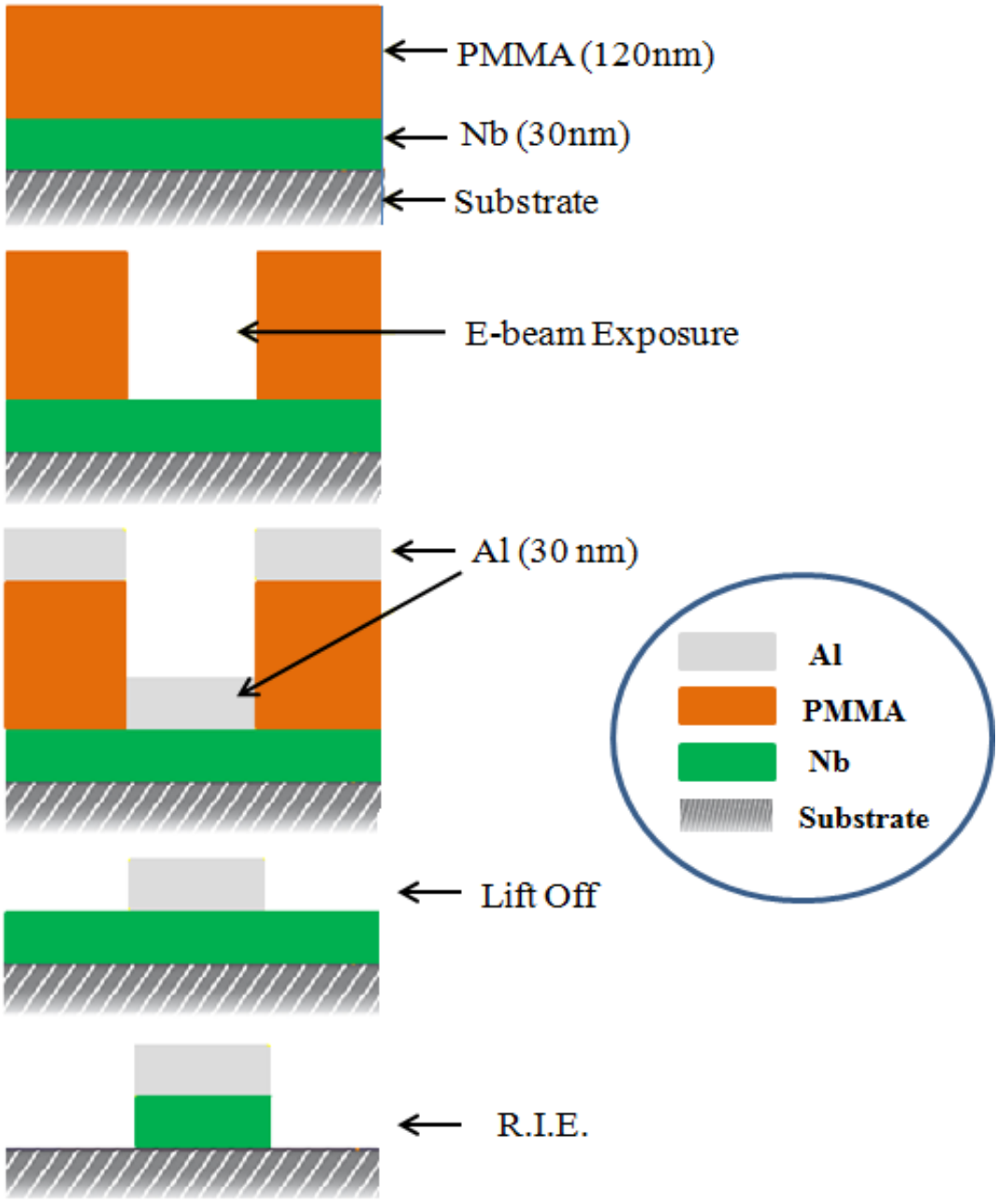

Fig.3.8 Schematic presentation of steps involves in fabrication of the nanoSQUID based on niobium dayem nanobridges.

Thin Film Deposition: DC Magnetron Sputtering

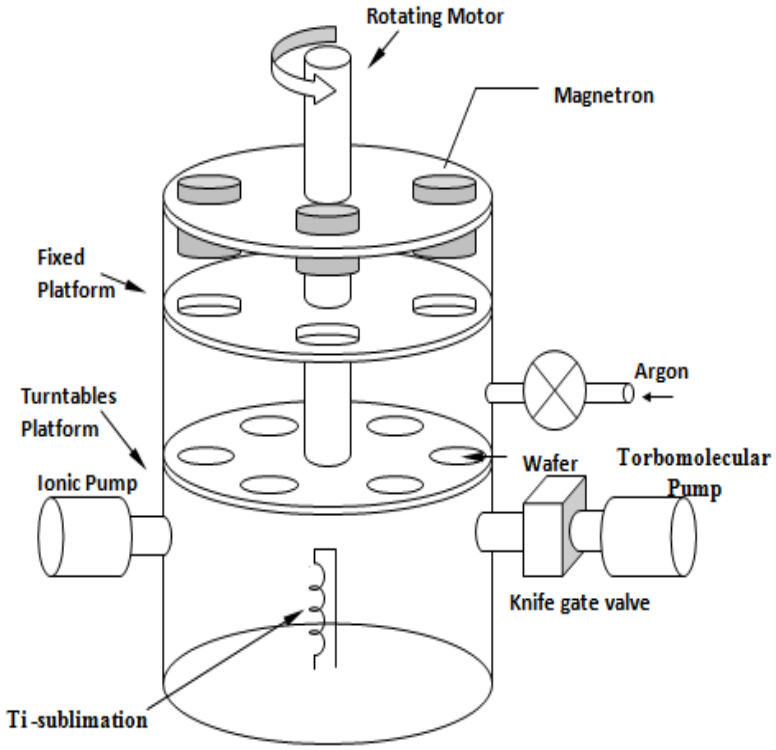

Fig. 3.9 Schematic appearance of the deposition chamber

Ultra vacuum deposition technique is needed, because of Nb small coherence length that makes the superconducting properties much dependent on chemical contamination as well as on reticular deformations.

The deposition of the layer takes place in an ultra vacuum chamber as schematically shown in fig.3.9, with three planar magnetron sources (5 cm of diameter) powered by a DC generator whose maximum power is 550W. Two of these magnetron were mounting Nb targets (99.8% pure), while the third one was an Al target (99.9% pure). Inside the chamber, the wafers are placed on a six-position tunable computer-controlled platform so that, in every moment, only one wafer is actually under the selected target.

The deposition technique adopted in the ICIB-CNR laboratories is the magnetron sputtering. Argon ions, Ar+, are accelerated by a potential between the cathode (the target) and the anode (the silicon substrate where the deposition takes place). In the collision with the cathode, the Ar+ ions must have energy sufficient to extract the target atoms; for that reason, high accelerating power (100-300W) and good vacuum conditions are needed. The extracted target atoms will then move in the chamber and, in part, will be deposited on the substrate in a quite uniform layer. To

increase the extraction rate, the Ar+ ion cloud is collimated by a magnetron producing a toroidal field near the target. In the case of metallic target, DC voltage generators are used, while for dielectric target (like SiO) RF voltage generators are needed. In order to reach the correct deposition pressure three different pumping systems are required. A turbomolecular pump (Blazer TVP 9000), capable of removing 260 l/s and reaching the vacuum pressure of 10^{-9}Torr, leaves the deposition chamber filled mainly by hydrogen, water vapour, and hydrocarbides. These gases were eliminated by using an ionic pump (Varian) with pumping velocity of 400 l/s and vacuum pressure of 10^{-11}Torr. Its working mechanism is similar to a triode: a thermoionic filament generates electrons which, accelerated by a positively charged grid, ionize the residual gases. The produced positive ions are then chemically adsorbed by the cathode up to complete saturation. The last pump, a Ti sublimation one, is instead used to eliminate the chemically active gases (HO_2 vapors etc.) The pressure in the chamber can be read by two Varian ionizing probes, which operate respectively in the low vacuum regime (10^{-1}-10^{-4}mbar) and in the ultra vacuum one (10^{-4}-10^{-12}mbar). During the sputtering deposition, the pressure is monitored by a Baraton capacitive probe.

Moreover, the system has three input lines, for Ar, O_2, and N_2. The deposition process consists of two steps: presputtering and sputtering. The presputtering is needed to remove the target's superficial layer, Ar gas is introduced in the chamber up to a pressure of 3.5 x 10^{-3}Torr and accelerated toward the Nb target with a power of 250 W by constant voltage between the cathode and the anode. Presputtering lasts for 180s, and the extracted target atoms deposit on a blank wafer used only during presputtering operations; then the platform carrying the wafers is turned so that the correct substrates can be deposited.

In the sputtering process some parameters standardize the deposition:The gas pressure, that determines the concentration of Ar atoms and so the number of ions incident on the cathode and their mean free path; The deposition time, which determines the layer thickness under a given voltage and pressure; The voltage between cathode and anode, which determines the energy with which the Ar+ ions collide the target. With the parameter of 3.5 x 10^{-3}Torr used for argon pressure, and a power of 300 W, we obtained a deposition rate for the base Nb layer of $15\,\mathring{A}/s$. The typical base layer thickness, sufficient to the correct growth of niobium grains to form a homogeneous crystallographic structure, is $300\,\mathring{A}$, corresponding to approximately 20s of deposition time. Also with same parameters for Al deposition, we obtain deposition rate about $7\,\mathring{A}/s$ corresponding to 43s deposition time. Initially, we deposited 30nm thick Nb film on oxidized silicon wafer. Later, after e-beam patterning on resist layer, we deposited 30 nm Al film on patterned PMMA resist-Nb film.

Resist Deposition and E-Beam Patterning:

In the simplest positive resist, electron irradiation breaks the polymer backbone bond, leaves fragments of lower molecular weight. A solvent developer selectively washes away the lower molecular weight fragments, thus forming a positive tone pattern in the resist film. Polymethyl methacrylate (PMMA) is a standard positive e-beam resist and one of the highest resolution (less than 10nm) resists available.

Following steps are involved in this process:

- The 30nm niobium layer is deposited on the oxidized Si substrate by magnetron sputtering as mention above.
- Substrate with Nb layer is cleaned with propanol, acetone and then blown with dry nitrogen. PMMA (having molecular weight 950K, 2% in anisole) is spun with spinning rate 2500rpm for 60sec. onto the substrate and baked in oven at 180^0C for half hour. Thickness obtained after baking is 120nm.
- Exposed PMMA in e-beam system at 10kV, with dose between 100-140 μC/cm^2
- After exposure, Substrate develops for 30sec. in 1:3 MIBK: IPA (methyl isobutyl icetone: isopropyle alcohol). Rinse in IPA, in order to remove burnt resist and blown dry nitrogen.
- Pattern on the resist can be recognized by SEM or optical microscope after each step as schematically shown in fig. 3.10(1).

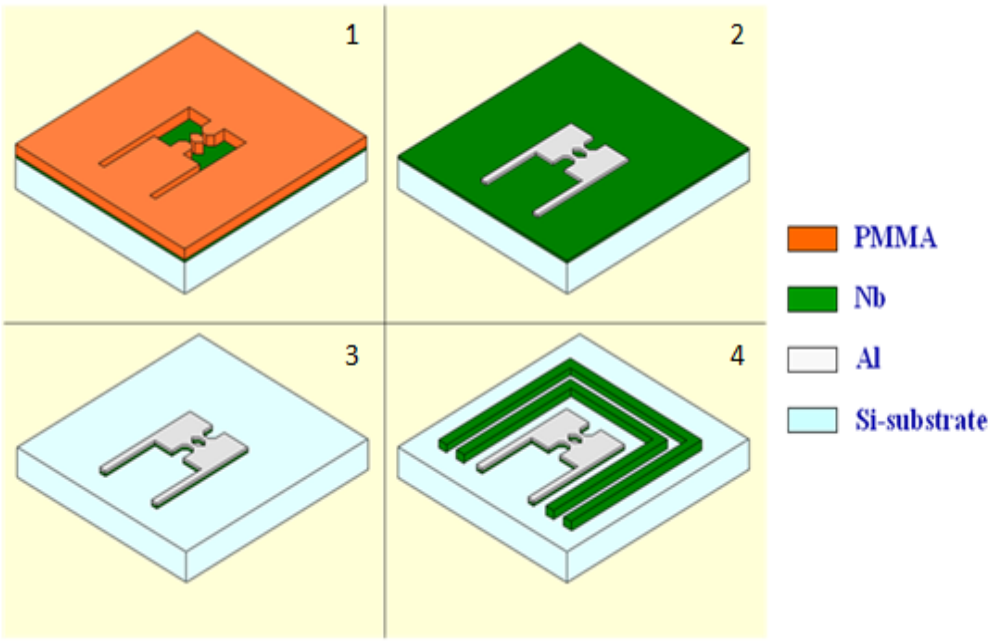

Fig.3.10 3-D Sketch of the fabrication process of the nanoSQUID based on niobium Dayem nanobridges.

Pattern Transfer by Lift Off and R.I.E. process:

After exposing the PMMA resist, the 30nm thick Al film was deposited on the substrate by dc magnetron sputtering after soft ion beam cleaning process as shown in fig. 3.10(2). Shaping of Al is carried out by Lift Off process, in which we used acetone as best solvent for PMMA as shown in fig. 3.10(3). Following are steps involve in Lift Off.

- Kept substrate 1-2 hour into acetone.
- Ultrasonicate it for 1-2 minute and washed into propanol, deionised water and acetone then blown with dry nitrogen simultaneously.
- Clean surface by O_2 plasma under oxygen pressure about $500x10^{-2}$ Torr for 10 minutes. Inspect pattern under optical microscope.
- If inner hole of SQUID is not opened, then use cotton flogs with acetone and smoothly wipe the substrate in order to open loop. (This step is very tricky) Finally inspect the pattern.

Al offers several advantages with respect to other materials; in fact it ensures a good nanometric definition for the lift-off processes, it shows a low resistivity (only 20% higher than gold), and it is insensitive to the RIE etching with CF_4. However, if the experiments were to require temperatures lower than 1.2K, the aluminum can be replaced by other materials (Au, Au–In), preserving the effectiveness of the process. The definite shape Al film acts as resistive shunt as well as self aligned mask for RIE process. Finally pattern is transferred to Nb layer by reactive ion etching process. The parameters used for the RIE process are tabulated as below:

GAS used 1) CF_4 2) O_2	Partial Pressures 48 mTorr 2 mTorr
Radio Frequency power	30 W
Etching Rate	15 nm/ min.

After two and half minutes etching, substrate was inspected to see pattern which is shown in fig. 3.10(3). Due to the poor aspect ratio of RIE processes, there is a small undercut in the Nb layer of the order of 20 nm. The bridge width dimension of 80 nm is referred to the Nb layer.

The SEM image of our fabricated device having 200nm SQUID washer loop where the Josephson junctions are located on the outer edge of the square loop has been shown in fig. 3.11.

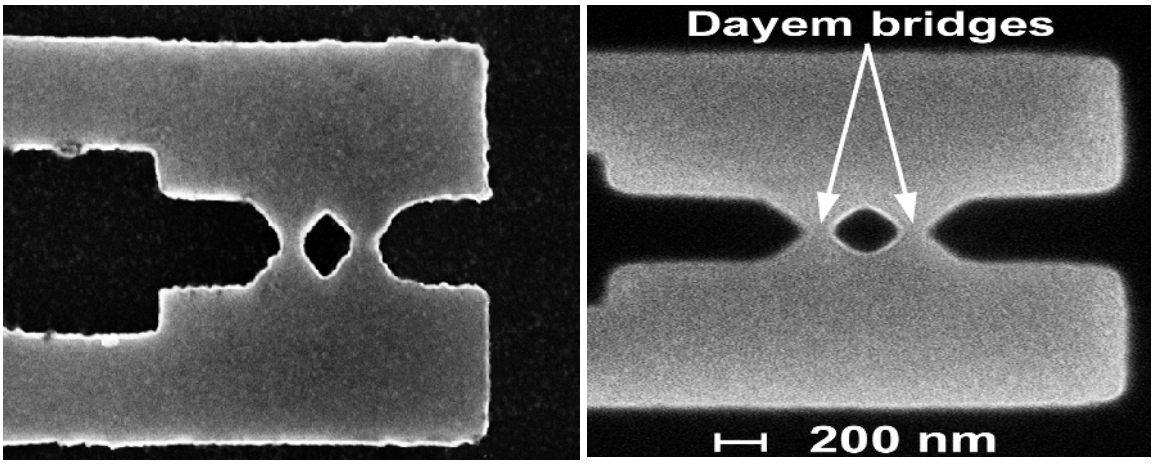

Fig. 3.11 SEM image of SQUID having washer loop of 200nm consisting two dayem bridges located at the outer edge of loop.

Integration of Coil and Wiring:

It is also importance to stress that the integration of EBL and optical lithography is useful; in fact, the integrated modulation/calibration coils must be more than 200nm thick and 3μm width coil, in order to sustain the suitable current value (about 100 mA) and to acquire the *V*–Φ characteristics to tune the sensor. To fulfill this requirement, the deposition of photoresist on substrate is first step of this process. By using a spinner for 30s at 5000rpm, an uniform layer of 1μm of photoresist (AZ 5214-E Hoecst) is applied on the wafer surface, and then baked at 90^0C for 30 min, to let the photoresist solvent evaporate and to strengthen the photoresist itself. Then the wafer is exposed under an UV Hg lamp for 14s, having applied the realized base photomask prepared by EBL. Our mask aligner is capable of an alignment of upper layers of the order of micron.

After the exposition, by immersing the wafer in a deionized water and potassium hydroxide (KOH), only the exposed photoresist could be selectively removed, but we proceeded to an inversion of the photoresist by means of another baking at 120^0C for 10min. and a subsequent flood exposition (without the photomask) for 30sec. Through this negative photolitographic technique, the doubly exposed photoresist is made insoluble, and we were able to remove the resist only in correspondence to the desired (negative) geometry. Before the development, the wafer is immersed for 3min. in chlorobenzene, which modifies the photoresist profile, tilting it of approximately 20^0. This process makes possible to correctly remove photoresist, after the deposition.

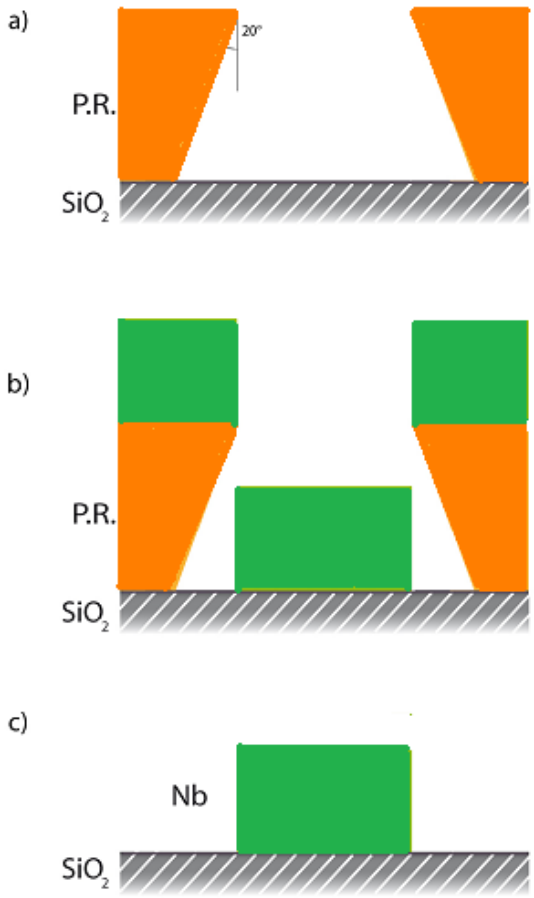

Figure 3.12: Steps of the lift-off process in the coil and wiring pattern deposition: a) Photoresist (P.R.) on silicon substrate. b) Deposited Nb layer c) Sample after Lift-Off process

The two integrated coils (3μm wide) and the SQUID contact pads (wiring) are patterned by this standard optical lithography technique (Fig.3.9 (4), fig.3.13, fig. 3.14). The coils are defined by lift-off after a deposition of a 200nm thick Nb film by dc-magnetron sputtering as explained in previous section. In order to ensure a clean contact between the Nb lines leading to the SQUID and the Nb contact pads, both a wet etching of Al and an ion etching for cleaning are performed before the wiring deposition.

Passivation:

Passivation is the final stage of the manufacturing process and is covered with a layer of photoresist (KTFR), this particularly resistant to thermal stress.

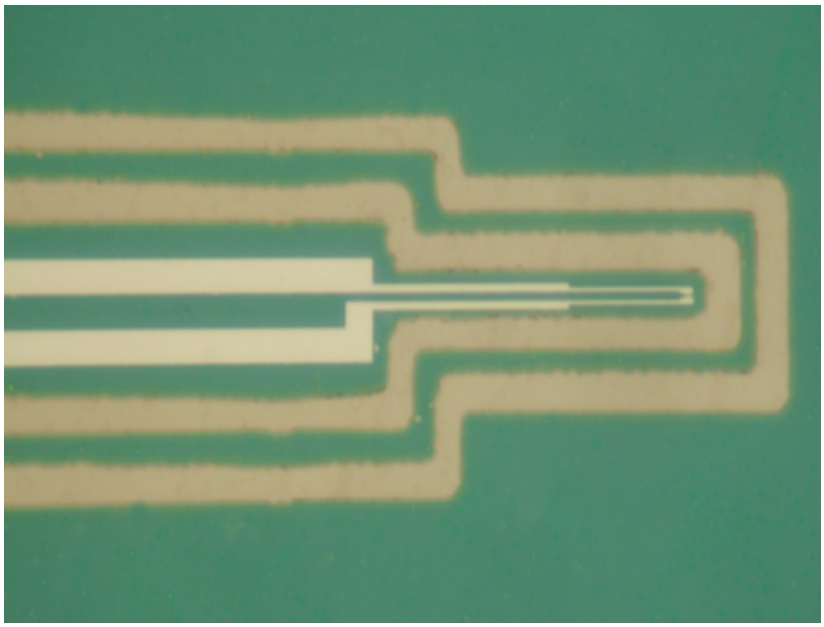

Fig. 3.13 optical image of two integrated niobium coils (orange color stripes) located around SQUID loop.

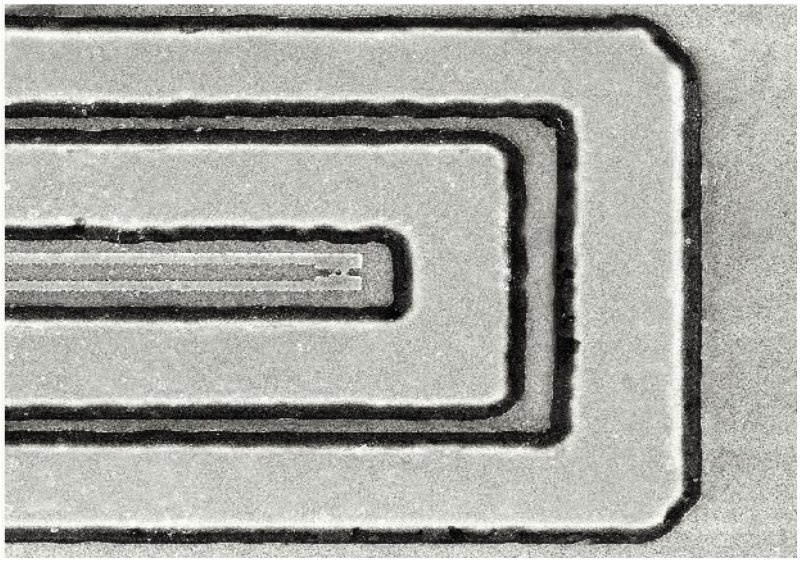

Fig. 3.14 SEM image of two integrated niobium coils showing larger thickness and width around SQUID loop.

3.3 Fabrication Process of Single Layer Device:

Single layer device has been fabricated using design shown above with EBL patterning and lift off process. This device has been formed in few steps and has advantage of simple and reproducible fabrication.

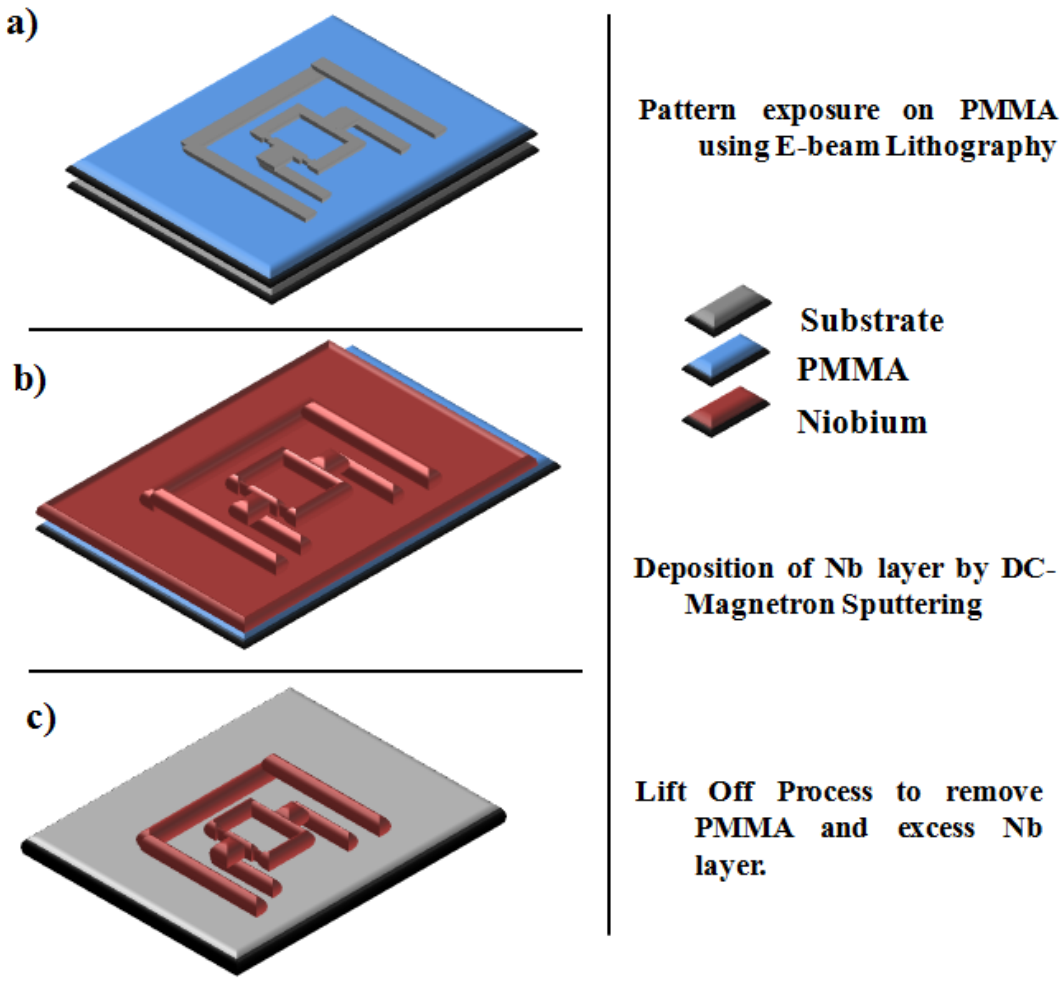

Fig.3.15 Sketch of fabrication process of nanoSQUID consists of two symmetric nanoscale dayem bridges as well as two integrated coils around SQUID.

The fabrication process involves e-beam exposure, deposition of Nb Layer and lift off as shown schematically in fig. 3.15. Initially, 120nm thick polymethyl methacrylate resist (PMMA) is deposited on Si substrate by spin coating and baked it for 30 min. at 180^0C. Then the devices are patterned by e-beam lithography with beam of 10kV on to the PMMA resist layer in order to pattern the image of both the Josephson nanobridges

consisting washer loop and the SQUID with integrated coils (fig.3.15 (a)). Later the Nb thin-film is deposited on Si substrates having pattern exposed PMMA layer in a dc sputtering system with a vacuum base pressure ~10^{-8} mbar (fig.3.15 (b)). The 20nm thick Nb films is used for the fabrication of junctions, SQUIDs and integrated coil. The excess Nb and PMMA are removed by simple Lift off using acetone as significant solvent. Since the Nb film is viewing pattern of SQUID (fig.3.15 (c)).

The scanning electron microscopic image of the device having the loop diameter is 0.75 and 2μm with the nanobridge junctions of 120nm wide and 250nm long as shown in fig. 3.16.

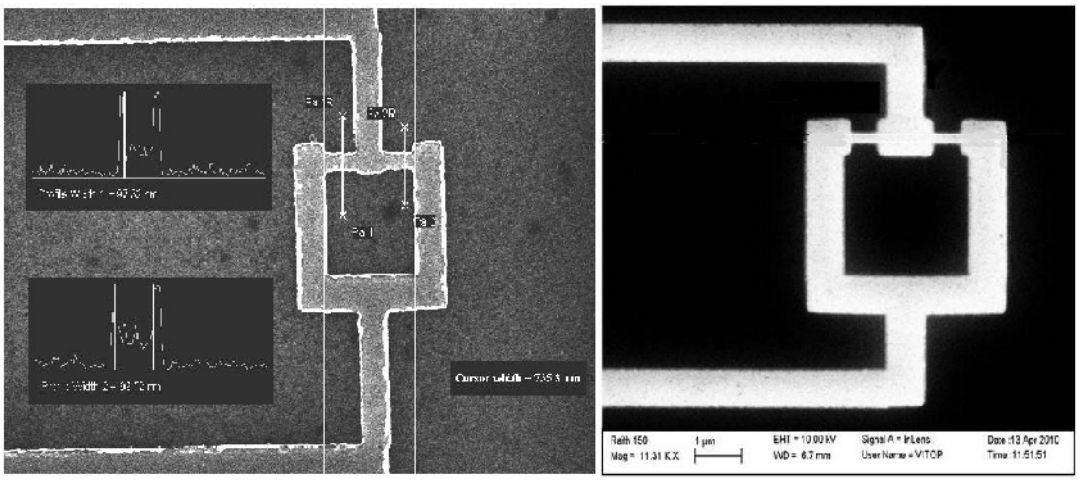

Fig. 3.16 Scanning Electron Microscopic image of SQUID device having 0.75 and 2 μm SQUID loop consists of 120 X 250 nm^2 nano-dayem bridges.

The SEM image of SQUID with its surrounded coils is shown in fig.3.17. Single layer devices can be reproduce easily with respect to bilayer devices due to its limitations of arranging one layer over other. Only Liff off process should be definite, to get distinct pattern as expected.

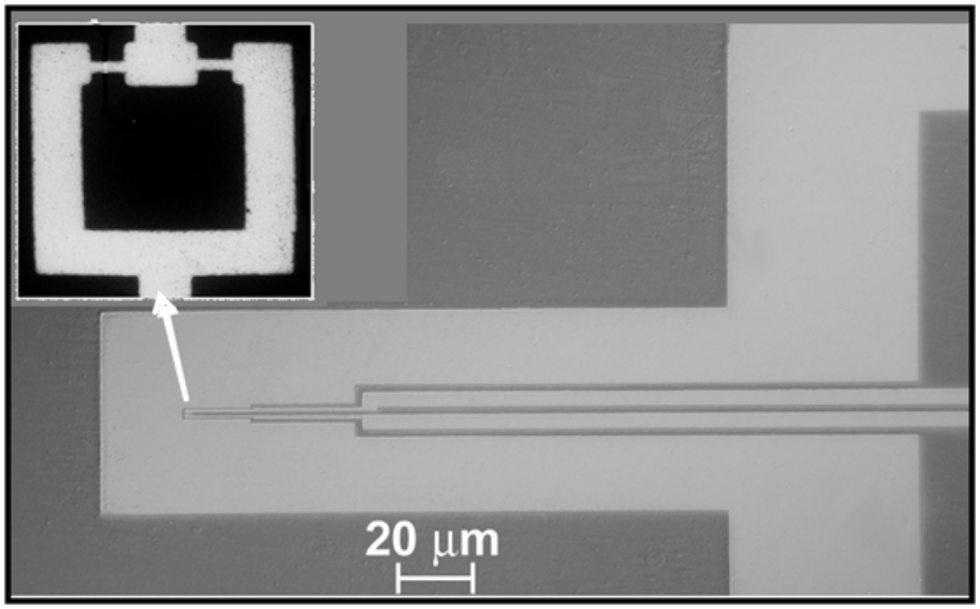

Fig.3.17 SEM image of integrated coil patterned by EBL around the SQUID loop. The inset of figure shows SEM of SQUID loop in parallel washer shape having two bridges.

The production of nanoscale device using EBL is very tricky and complicated; however there may be failure or defects during patterning in some regions. So, we have produced sequence of devices on single chip during same EBL exposure which gives probability to have many successfully fabricated devices at moment.

References

1. D. R. S. Cumming, S. Thoms, J. M. R. Weaver and S. P. Beaumont. Microelectronic Engineering Vol 30. pp 423-425 (1996)
2. McCord, M. A.; M. J. Rooks, *SPIE Handbook of Microlithography, Micromachining and Microfabrication* (2000)
3. P. Grivet, *Electron Optics*, Elsevier, Oxford, Pergamon imprint (1965)
4. T. H. P. Chang, J. Vac. Sci. Technol. 12, 1271-1275 (1975)
5. R. Birkhoff, in Handbuck der Physik, E. Fluegge, ed., Springer, Berlin and New York, 53 (1958)
6. K. Murata, D. Kyser, and C. Ting, J. Appl. Phys. 52, 4396-4405 (1981)
7. M. Hatzakis, "Recent developments in electron-resist evaluation techniques," *J. Vac. Sci. Technol.* 12 (6), 1276-1279 (1975)
8. C. R. K. Marrian *et al., J. Vac. Sci. Tech.* 10 (B): 2877–2881(1992)
9. K. K. Christenson, R. G. Viswanathan, and F. J. Hohn, "X-ray mask fogging by electrons backscattered beneath the membrane," *J. Vac. Sci. Technol.* B8(6), 1618-1623 (1990)
10. Y. Yau, R. F. W. Pease, A. Iranmanesh, and K. Polasko, "Generation and applications of finely focused beams of low-energy electrons," *J. Vac. Sci. Technol.* 19(4), 1048 (1981)
11. M. A. McCord and T. H. Newman, "Low voltage, high resolution studies of electron beam resist exposure and proximity effect," *J. Vac. Sci. Technol.* B10(6), 3083-3087 (1992)
12. Podd G J, Hutchinson G D, Williams D A and Hasko D G, *Phys. Rev.* B 75 134501 (2007)
13. Troeman A G P, van der Ploeg S H W, Il'Ichev E, Meyer H-G, Golubov A A, Kupriyanov M Y and Hilgenkamp H, *Phys. Rev.* B 77 024509 (2008)
14. Hasselbach K, Mailly D and Kirtley J R, *J. Appl. Phys.* 91 4432 (2002)
15. Lam S K H, *Supercond. Sci. Technol.* 19 963 (2006)
16. Lam S K H and Tilbrook D L, *Appl. Phys. Lett.* 82 1078 (2003)
17. Granata C., Esposito E., Vettoliere A., Petti L. and Russo M., Nanotechnology 19 (2008)

CHAPTER –4

Characterization of NanoSQUID and Preliminary Nanoparticle Magnetization Measurements

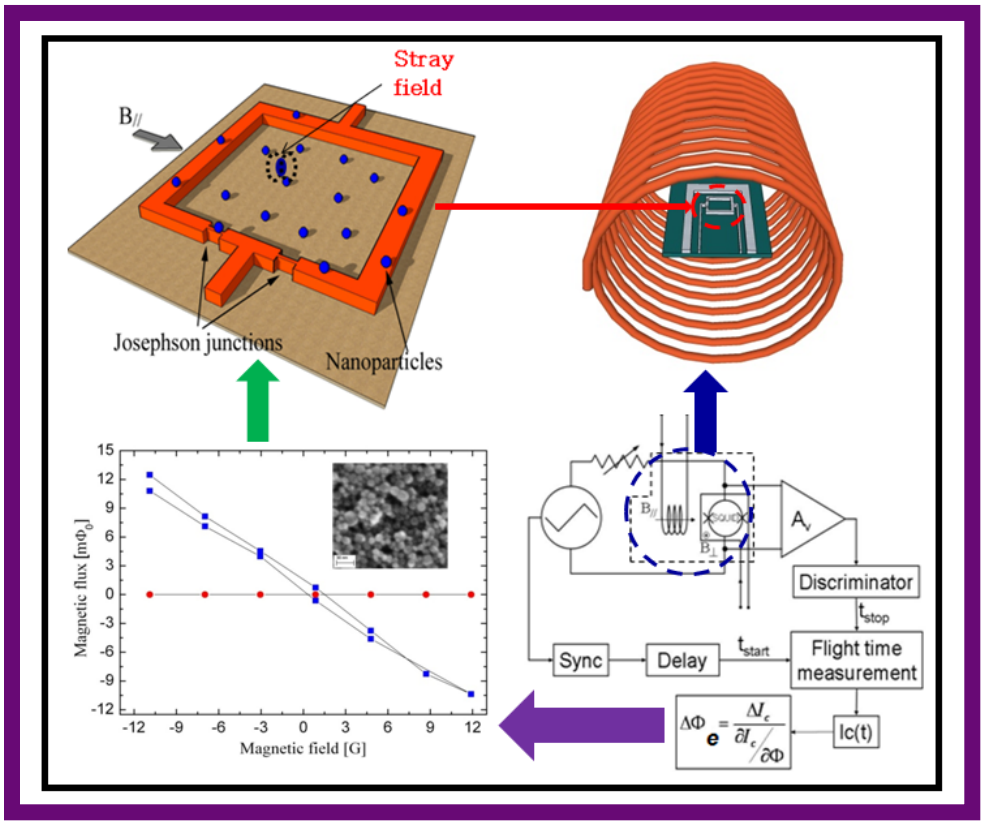

Recent interest in the development of nanoscale superconducting quantum interference devices has been motivated by the applicability of small spin detecting system in nanometer scale. There are stimulating challenges for SQUID sensor to detect the single or few electron spins and the study of the magnetization reversal of nanoobjects. This chapter is presented in two sections. First section reports the experimental performance of both non-hysteretic and hysteretic nanoSQUIDs like current-voltage characteristics, voltage–flux characteristics, flux to voltage transfer factor (responsivity), noise properties, critical current distribution measurement etc. The experimental data concerning the critical current switching probability which provide the useful information about intrinsic dissipation are illustrated. Finally in the last section, the preliminary measurements of iron oxide nanoparticles magnetization have been reported.

4.1 Characterization of SQUID:

The nanoscale SQUID performance can be evaluated from its characteristic features such as responsivity and current-magnetic flux, voltage-magnetic flux, noise characteristics. The measurements were performed in a liquid helium transport Dewar for both hysteretic and non-hysteretic SQUID. The devices were shielded by a lead/cryoperm coaxial double can, and all the electrical connections to room temperature were radio frequency filtered. The cryogenic insert and the readout electronics employed for characterization are briefly described as follow.

4.1.1 Cryogenic Insert:

To enable characterization of the sample at liquid helium temperature and its connection with the electronic instrumentation, the special insert is used commonly described as below. It consists of a steel tube which is nonmagnetic and low thermal conductivity as it moves enameled copper wires for electrical contacts. A thin bakelite support placed at the bottom containing positions or slots to anchor eight devices as represented in fig.4.1 and additionally solenoid wound around it to generate a magnetic field normal to the plane of the sensor. In this system, the block is fixed concentrically i.e. hollow cylinder on which solenoid has wound. The sample can be glued by KTFR on a support vetronite which equipped with a special copper tracks that provide the link between the contacts of the device and those of the offspring as shown in fig. 4.2. The electrical connections of the sample support are made through a thin aluminum wire (25μm) through an ultrasonic welding "Wedge Bonder (Kulik & Breath). The support is then pasted into one of the slot chambers by a descendant cryogenic adhesive layer and connected by normal soldering to measuring electronics.

Fig.4.1 Picture shows end of special insert where SQUID containing chip mounted. The strip has 4 SQUID positions at both sides.

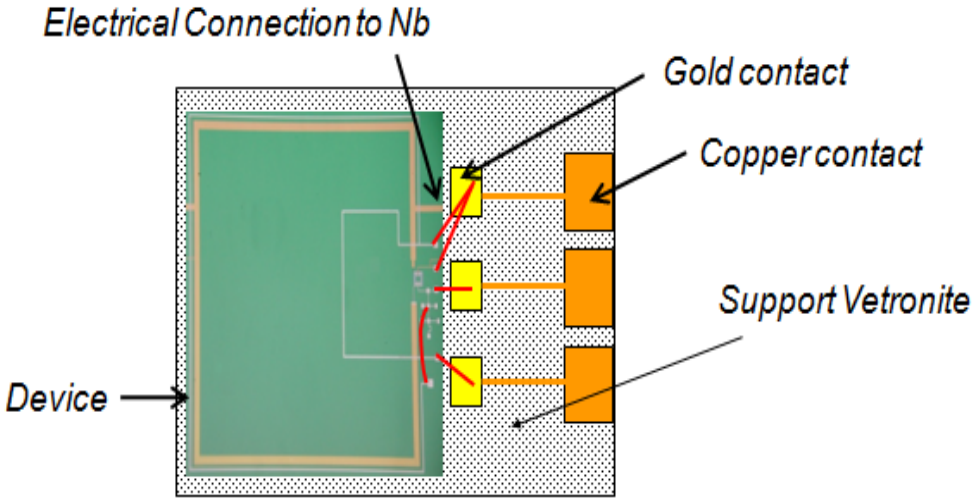

Fig.4.2 Schematic drawing of Vetronite support for device and electrical connections

4.1.2 SQUID Electronic Readout:

Current Voltage (I-V) Readout:

All the measurements are performed by using low-noise electronics organized at ICIB-CNR [1-4] and battery-powered to reduce the noise signals coming from the power lines. The used electronic has capacity to work up to 100Hz. This electronic allows measuring the I-V characteristic by biasing the SQUID with a current I_{bias} and measuring the drop-voltage V by using low noise 4-contacts technique. With this technique, it is possible to decouple the wires used for the bias from the wires used for the voltage, so that the resistance value for the measured device is obtained without considering the wire contributions. In order to perform measurements, it has been necessary to pass through the cryogenic insert all the necessary lines to bias the circuits.

A new Labview "Virtual-Instrument" has been developed to exploit the performances and the accuracy of a new National Instrument 6281 DAQ, capable of 18 bit sampling at a frequency of 500KS/s in multichannel configuration and having the range between -100 mV and 100 mV, an accuracy of 28 μV and a sensitivity as high as 0.8 μV. Great care was placed in the development and testing of the Virtual Instrument, in the effort of integrating and automatizing a vast number of functions and sub-instruments in the same working panel, without losing its usability and efficiency.

In order to read the voltage drop at the SQUID, two stages are used. The first one has a fixed gain and second one has a variable gain selectable between 2-6-20-100 times.

So, the voltage drop can be finally amplified up to 500 times. Moreover, there is a switch “short-open", in order to decouple the SQUID and the readout electronics. The voltage and the current are sent, respectively, to two of the 16 inputs of a NI 6281.

Noise Characterization:

We have seen that a dc-SQUIDs are used as flux voltage converters as result of their special characteristics i.e. $V-\Phi$ trends are periodic and therefore appears to be nearly linear only around a very small point $(n+1/4)\Phi_0$. To increase the slope in the region of linearity, usually dc SQUID is inserted in a feedback circuit coupling flow, called "Flux-Locked-Loop (FLL) [5]. Typically a flow is applied outside the SQUID and its voltage V across it is amplified, integrated, and its current sent through a feedback loop i.e. a coil whose effect is to maintain the flow in the SQUID at a constant level. The measured voltage across the feedback resistor is proportional to the applied external flow. The technical realization of the circuit reading “FLL” is used in the production of most applications that usually require a high "range" dynamic linearity.

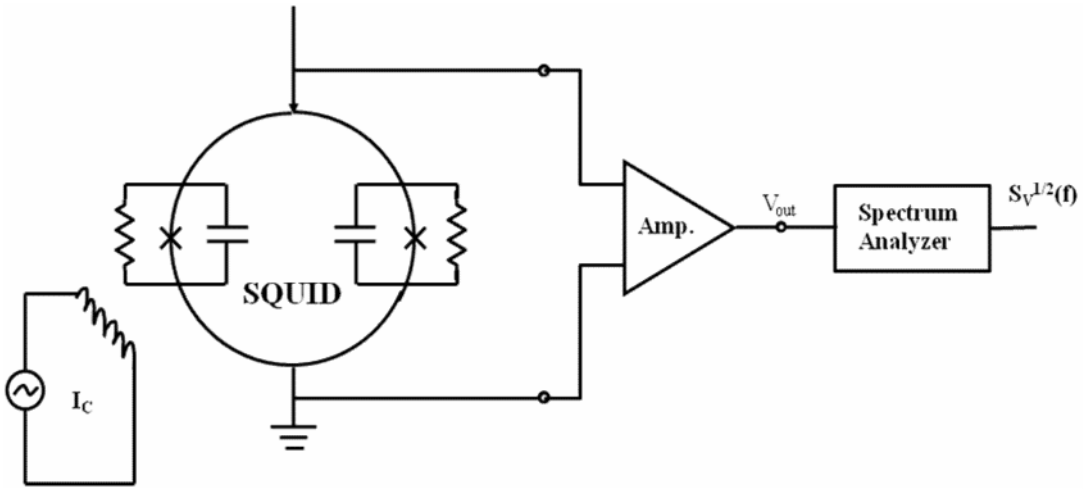

Fig.4.3 Experimental set up for measurement of voltage noise spectral density by means of spectrum analyser.

The simplified circuit is depicted in fig.4.3. The SQUID is directly connected to an ideal low-noise preamplifier. If the signals to measure are small, it is possible to employ the sensor in small signal mode. In this case the sensor is biased around $(n+\frac{1}{4})\Phi_0$ where the $V-\Phi$ is linear. The individual circuit elements are sized, so that the external flux which concatenates with the SQUID is offset by the flux generated

through a coil. The voltage $V_{n,amp}$ (noise source) of spectral density $S_{v,amp}(f)$ provided input to the preamplifier, it summarizes the noise voltage including the contribution of the Nyquist noise of the resistors in the preamplifier itself.

The current noise of the preamplifier is linked by:

$$\Delta S_{V,amp}\left(f\right) = S_{I,amp} \cdot R_{dyn}^2 \tag{4.1}$$

where R_{dyn} is the dynamic resistance of the SQUID at the working point.

The effective spectral density of flux noise $S_{\Phi,t}(f)$ of the system is given by [6]:

$$S_{\Phi,t}(f) = S_{\Phi}(f) + \frac{S_{V,amp}(f)}{V_{\Phi}^2} \tag{4.2}$$

where the first term of the sum is the spectral density of the intrinsic noise of the SQUID in flux and the second is the contribution of flux noise preamplifier. Consistent with the previous equation, a typical SQUID with a white noise in flow of about $10^{-6}\,\Phi_0$/ $(Hz)^{1/2,}$ and a transfer coefficient of 100 $\mu V/\Phi_0$, the noise voltage is about 0.1 nV/$(Hz)^{1/2}$ the typical noise level of an amplifier, however, is about 1 nV/$(Hz)^{1/2}$. So one must increase its rate of transfer at least one order of magnitude to achieve comparable levels of noise. However for nanoSQUID based on dayem bridge, it is possible to obtain V_{Φ} as high as 1-2 mV/Φ_0, reducing the equivalent flux noise of the amplifier to a tolerable value.

4.2 Comparison between Hysteretic and Non-Hysteretic SQUID:

The origin of hysteresis in dayem bridge based SQUID has been discussed in previous chapters. The hysteretic SQUID gives noisy characteristic which ultimately diminishes the sensitivity of the SQUID. Generally, the noise level of the non-hysteretic SQUID is about $10^{-6}\Phi_0$ and in case of hysteretic SQUID, it is about $10^{-4}\Phi_0$. The noise characteristic clearly indicates less sensitivity of hysteretic SQUID than non-hysteretic one. Also the non-hysteretic SQUID can be operated in standard readout electronic like flux locked loop configuration for large scale measurements. So it becomes easy to use and faster in operation. On the other hand, hysteretic SQUID cannot operate in standard flux locked loop. The hysteretic SQUID has advantages over non-hysteretic one such as; it has non-dissipative characteristics and simple fabrication. It can work as a trigger in cold mode too.

We have fabricated many devices in different configurations using e-beam lithography techniques as explained in previous chapter. Apart from quantitative data, the qualitative results obtained from convenient devices are reported here. The dimension of devices are playing crucial role in its performance and applications. From our experimental evaluation, a good compromise is reached using the dimensions (lengths/widths) and thickness of the bridges ranging from 50 to 150 and 10 to 50 respectively.

4.4.1 Non-Hysteretic Device:

Here the characterization of a nano-SQUID shunted by an aluminum film is reported. The sensor, having a washer shape with a hole of 200 nm and two Josephson–Dayem nanobridges of 80nm ×100 nm, consists of a Nb(30 nm)/Al(30 nm) bilayer is presented.

Current Voltage Characteristics:

As expected, the I-V characteristics of an integrated nano-SQUID based on niobium Dayem bridge junctions (80nm×100nm) interrupting 200nm loop shunted by an aluminum are non-hysteretic in nature. In presence of magnetic field, the change in current-voltage characteristics occurs due to variation in magnetic flux threading SQUID loop. *I–V* characteristics of a nano-SQUID at a magnetic flux $\Phi = 0$ and $\Phi_0 / 2$ threading the sensor hole are shown in figure 4.4.

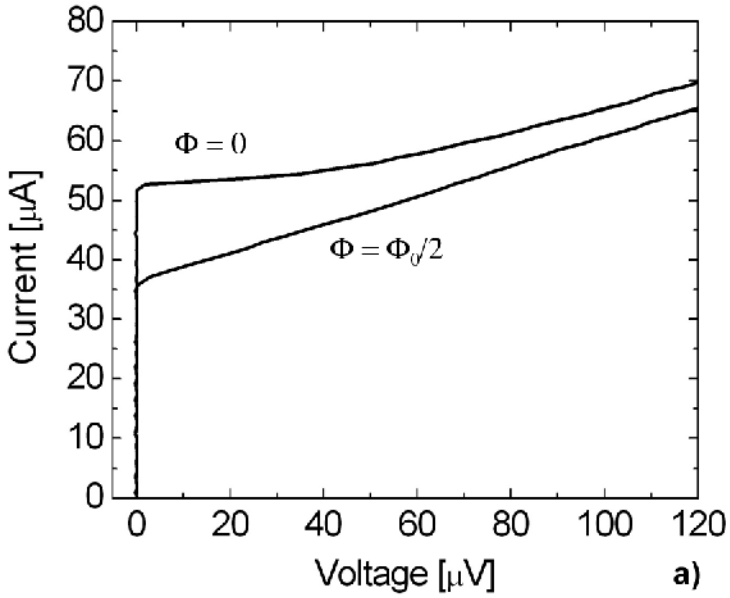

Figure 4.4 Current–voltage characteristics of a nano-SQUID sensor measured at liquid helium temperature with a magnetic flux $\Phi = 0$ *and* $\Phi_0 / 2$ *threading the sensor hole.*

Since the external magnetic flux was applied by sending a dc current in the closest integrated niobium coil, 21 mA current is required to obtain an applied half flux quantum. The non-hysteretic behavior of the *I –V* characteristics allows us to use the SQUID sensor as a standard flux-to-voltage transducer. An adequate current modulation depth $\Delta I_0 = 18\mu A$ corresponding to 35% of the maximum critical current ($I_0 = 2I_C = 50\mu A$) is measured from experimental curves.

Using a value of $\Delta I_0 / 2I_C = 0.35$ and a device inductance parameter $\beta = 2LI_C / \Phi_0 < 1$ where total inductance $L = L_k + L_h$ is the effective inductance of the SQUID, and I_C is the critical current of the single weak link, an effective bridge length of about $6\xi_0$ (ξ_0 being the coherence length of the niobium film at *T* = 0 K) can be evaluated on the basis of the one-dimensional micro-SQUID model [7]. A normal resistance $R = 6\Omega$ is measured from the *I –V* characteristics (figure 4.4).

We know that the dynamic resistance R_{dyn} close to the zero voltage state for $\Phi = 0$ is much greater than the normal one. As expected, it evidently decreases for $\Phi = \Phi_0 / 2$. High dynamic resistance together with a large current modulation depth produces a large SQUID voltage swing ($(\Delta V \propto R_{dyn}\, \Delta I_0)$ and a high responsivity. A further significant increase of I_0 or R_{dyn} causes hysteresis in the *I –V* curves or unstable and noisy characteristics. If a direct-coupled readout is used, high R_{dyn} has to be avoided since the flux noise due to preamplifier current noise ($(S_{I,A} R_{dyn} / V_\Phi)$ may not be negligible [8-9].

Responsivity i.e Current- Flux and Voltage-Flux Characteristics:

In figure 4.5, the critical current as a function of the external magnetic flux is reported. As expected, the critical current I_0 is a periodic function of the flux threading the SQUID loop; so it is possible to easily deduce the flux variation in the SQUID loop by measuring the critical current variation.

However, a non-hysteretic SQUID sensor is typically used as flux to- voltage transducer [10], obtaining a better flux sensitivity and a simpler operation. Therefore a relevant factor of merit for a SQUID device is the voltage–flux transfer coefficient obtained from the $V - \Phi$ characteristics.

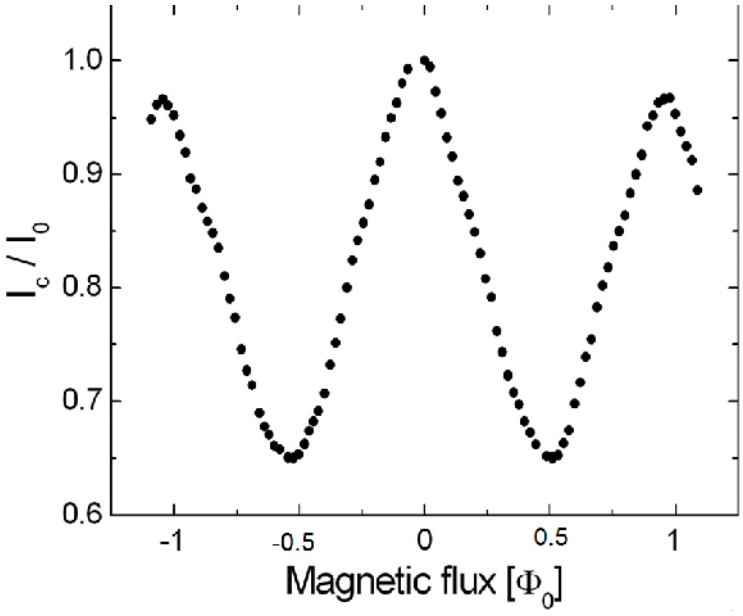

Fig. 4.5 The periodic oscillation of critical current as a function of the magnetic flux.

In figure 4.6, $V-\Phi$ characteristics measured by feeding an ac triangular current signal (10 Hz) of about 100 mA peak-to-peak in the closest integrated coil by a standard waveform signal generator.

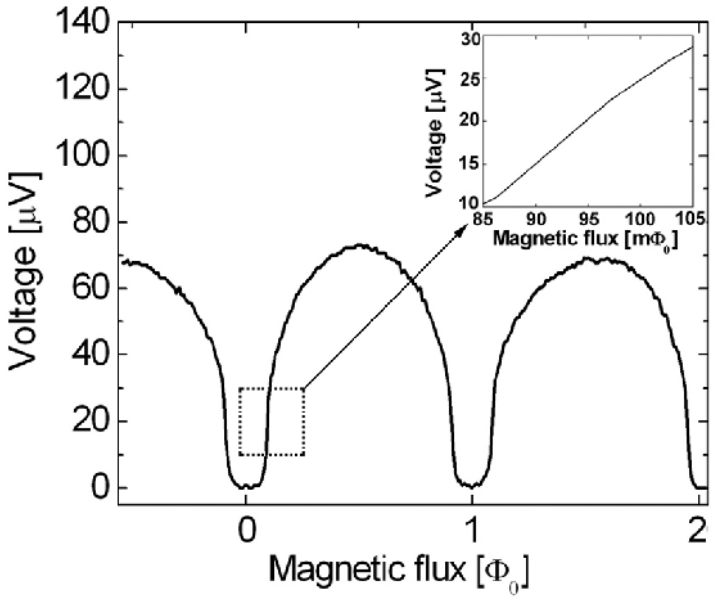

Figure 4.6 Voltage–magnetic flux characteristics of a nanodevice. A maximum voltage–flux transfer coefficient as high as $1mV/\Phi_0$ is evaluated from the linear side of the characteristics reported in the inset.

Due to the integrated coils, it has been possible to measure up to three flux quanta. An intrinsic voltage swing as high as $75\mu V$ is estimated from experimental curve. The maximum responsivity i.e. voltage flux transfer coefficient $1mV/\Phi_0$ is evaluated from linear side of $V-\Phi$ *curve indicated in inset of fig.4.6.*

Measuring the dc current flowing in the coil for the drift of a flux quantum, a current–flux transfer factor I_Φ of 42 mA corresponding to a mutual inductance between the coil and the SQUID $M=\Phi_0/I_\Phi=49\,fH$ has been obtained. As expected, the same measurement using the outer coil showed a lower mutual inductance (about 3 times).

Noise Characteristics:

The spectral density of the flux noise was measured in small signal mode. It has been obtained by dividing the measured spectral density of the voltage noise $S_V^{1/2}$ by V_Φ which corresponds to the dc magnetic flux bias during the voltage noise measurements shown in fig 4.3. The best noise performance is typically obtained by biasing the SQUID at its maximum V_Φ value, which is detected by maximizing a small signal while both the bias current and the dc magnetic flux bias are varied.

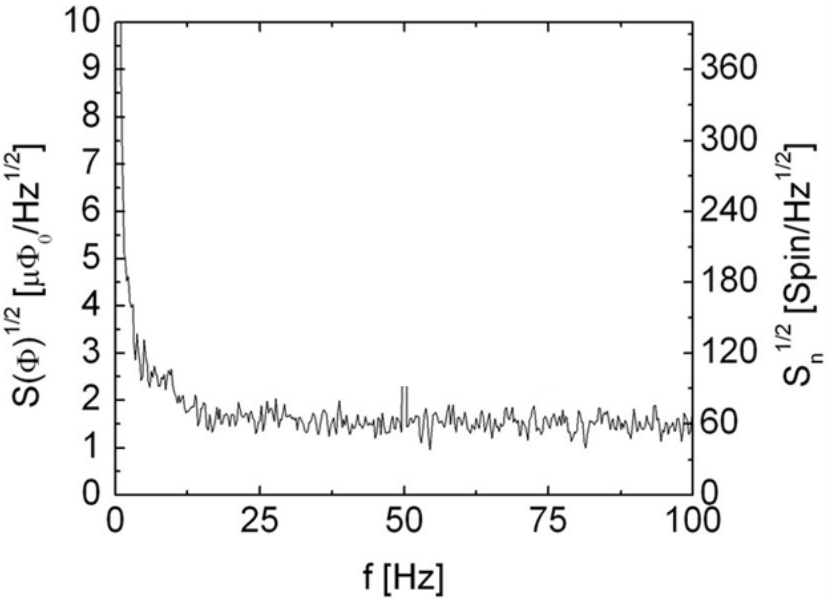

Figure 4.7 Sensor magnetic flux spectral density measured in liquid helium in the open-loop mode, using a direct coupling scheme with low-noise readout electronics. The SQUID was biased with a dc magnetic flux at its maximum responsivity point.

Figure 4.7 shows the low-frequency spectral density of the magnetic flux noise of a nano-SQUID device measured in open-loop (small-signal) mode biasing the sensor with a dc magnetic flux at its maximum responsivity point. Our interest is focused on the characterization in small signal mode, because the magnetic flux coupled into device is expected to be much smaller than Φ_0. In fact, such devices are designed to measure very small magnetic fields arising from a local nanoobject.

The sensor exhibits a magnetic flux noise level of $1.5\,\mu\Phi_0 / Hz^{1/2}$ in the white region corresponding to a spin noise, in unit of Bohr magneton, of

$$S_n^{1/2} = \frac{2aS_\Phi^{1/2}}{(\mu_B \mu_0)} \sim 60\, spin / Hz^{1/2} \qquad (4.15)$$

where *a* is the radius of the SQUID loop, μ_0 is the magnetic vacuum permeability and μ_B = 9.27 × 10^{-24} J/T.

However the above formula is based on a pessimistic assumption for the coupling, if an optimal one is taken into account a spin sensitivity value as low as $20\, spin / Hz^{1/2}$ is obtained. This value is comparable with the best value reported in the literature [10]. The excess low-frequency noise for frequencies less than 10 Hz could be due to the trapping and the subsequent hopping of electrons in defect states in the niobium film [11].

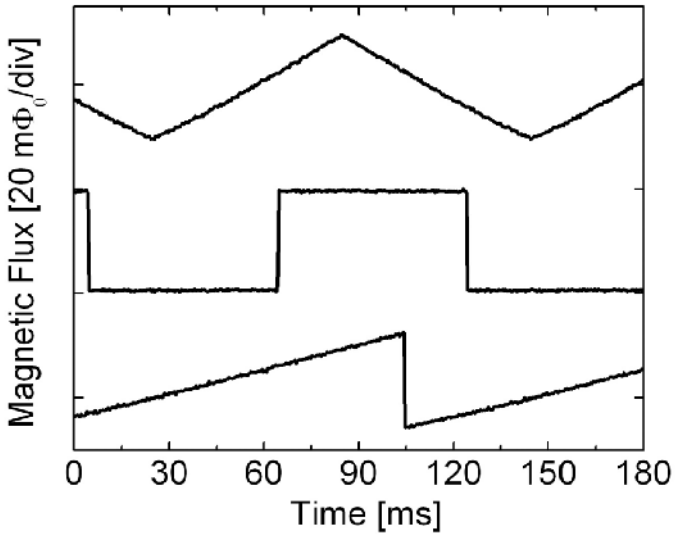

Figure 4.8 The nano-SQUID response in the small-signal mode produced by three different waveforms sent into the integrated modulation coil. For signals up to 0.02 Φ_0 nonlinearity effects are not evident.

The nano-SQUID output responses in open loop mode for three different input signals as shown in fig.4.8 (triangular, step and saw-tooth) are reported. They were obtained by sending the input signals into an integrated coil and flux biasing the sensor at its maximum responsivity.

Hence these sensors show a wide linear region in the $V-\Phi$ characteristics; the nonlinearity effects are not evident up to $0.02\Phi_0$, so in small-signal mode they reach a dynamic linear range of about $10^4 Hz^{1/2}$.

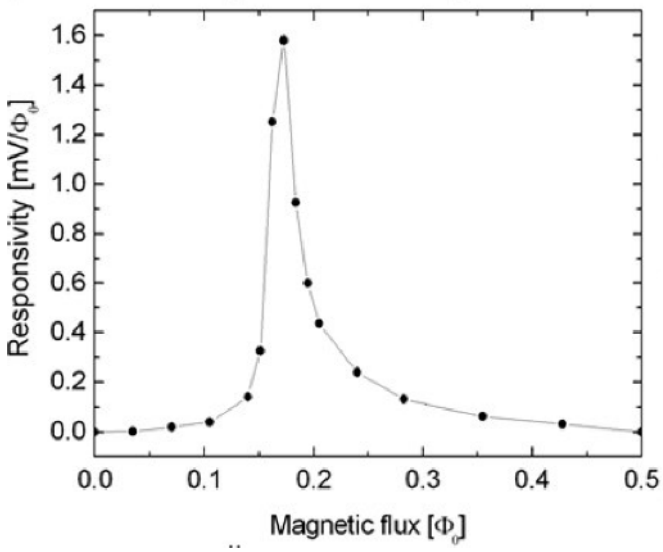

Fig.4.9 SQUID responsivity as a function of applied magnetic flux.

The fig. 4.9 shows the flux-to-voltage transfer factor as a function of the applied magnetic flux. It has been obtained by taking the derivative of the $V-\Phi$ curve in the range from $\Phi=0$ to $\Phi=\Phi_0/2$. A maximum V_Φ value as high as $1.6\,mV/\Phi_0$ for an applied flux 0.2 Φ_0 can be evaluated from the curve.

The asymmetry of the curve with respect to the maximum is due to the different curve slopes of the $V-\Phi$ characteristic in proximity of the minimum and maximum. The high responsivity is due to the large values of both critical current modulation depth and the dynamical resistance R_{dyn} close to the zero voltage state (20Ω). A high value of V_Φ reduces the amplifier noise contribution to a tolerable level i.e. the preamplifier contribution to the magnetic flux noise is less than 5%.

Taking into account a SQUID area of $4\times10^{-14}\,mm^2$, the magnetic field noise results in being $S_B^{1/2}=S_\Phi^{1/2}/A_{eff}\simeq 8\,nT/Hz^{1/2}$. The comparison between the measured flux noise and that predicted by the standard noise theory for resistively shunting tunnel junction based SQUIDs [5] is not plausible because of the different

behavior of the long $(L \gg \xi_0)$ nanobridge weak links with respect to the tunnel Josephson junctions. In any case, the excessively large magnetic noise with respect to a standard SQUID ($S_\Phi^{1/2} \approx \left[(16K_bTL^2)/R\right]^{1/2}$ for β = 1) could be due to the large R_{dyn} value close to I_0, which, on the basis of the small signal analysis [12,13], contributes to the overall spectral density of the voltage noise S_V with the term $2R_{dyn}^2 i_n^2$ (i_n is the SQUID current noise).

4.4.2 Hysteretic SQUID Devices:

The sensors, having two Dayem bridges of 90 nm x 250 nm and loop areas of 4, 1 and 0.55 μm^2, consist of a single 20nm niobium layer are designed for nanoparticles magnetization measurement. The SQUIDs having a hysteretic current-voltage characteristic can be used as a magnetic flux-current transducer. The sensor characterization is based on the measurements of current-voltage characteristics, switching current distributions and critical current as a function of the external magnetic field. All these measurements are carried out in a liquid helium bath at 4.2 K.

Current Voltage (I-V) Measurements:

The current-voltage (I-V) characteristics of nanoSQUID based on niobium dayem bridges having 1micron washer loop consisting of two dayem bridges (90nm x 250nm) is reported in fig. 4.10.

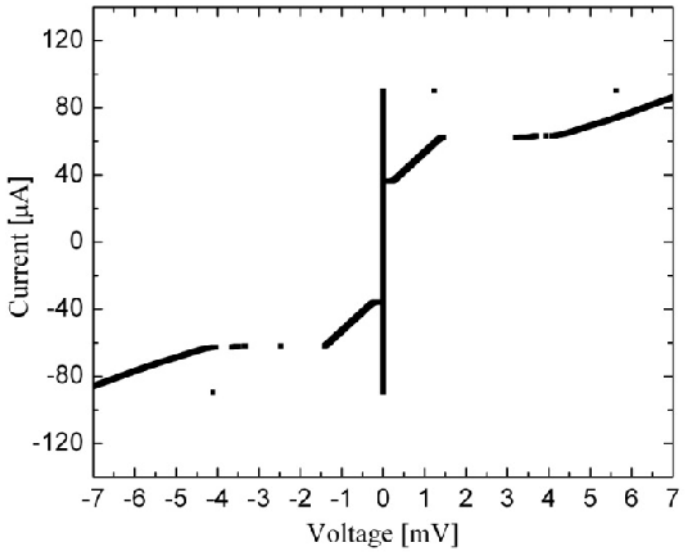

Fig. 4.10 *Current-voltage characteristic measured a T = 4.2 K relative to a nanoSQUID having a loop area of 1μm^2 and two Dayem nanobridges of 90 nm × 250 nm.*

The SQUID was current biased with a triangular-shaped waveform and a computer controlled DAQ acquired the typical I-V curve reported in Fig. 4.10. As expected, hysteresis is occurred due to large bridge dimension i.e. $L/\xi > 3.5$.

The SQUID is in the zero voltage state up to a current value (critical current I_C) about 90 μA in fig.4.10. Above I_C the nanobridges became resistive and dissipation will start increasing the local temperature. If the current is further increased, the whole SQUID will become normal conducting and the dissipation can induce thermal instabilities. On the backsweep, the device remains in the resistive state until a current much lower than the critical current of the SQUID is reached about 40 μA as shown in fig.4.10.

The modulation of critical current is elucidated from current voltage characteristics as function of applied field. The fig.4.11 shows the result obtained from the SQUID having 0.75 micron loop diameter.

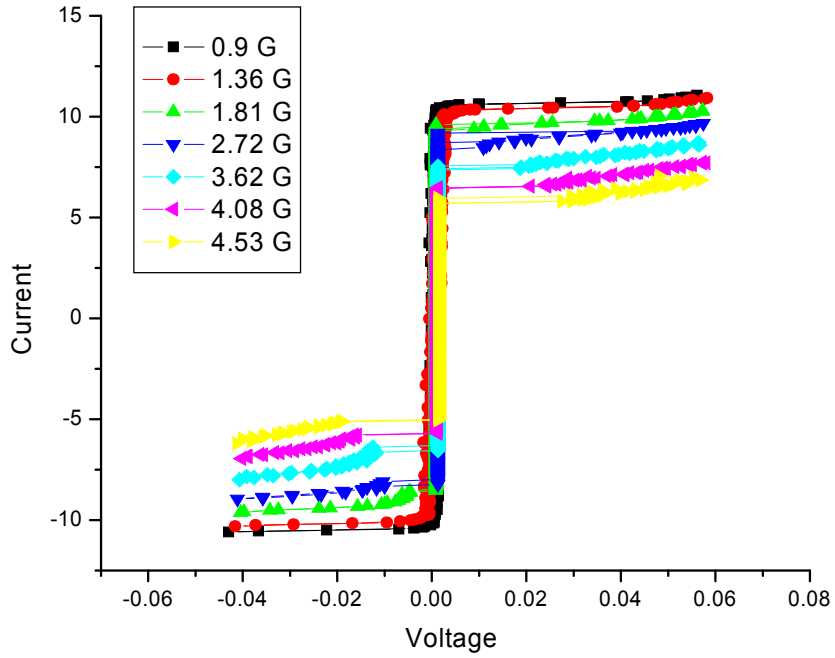

Fig.4.11 A nanoSQUID having 0.75 micron loop is showing the modulation in current-voltage characteristic with magnetic field.

A SQUID device based on a Nb nanobridge cannot work with the standard current biasing scheme because it shows hysteretic current–voltage (*I*–*V*) characteristics which could be due to either the energy dissipated in the nanobridge which heats the entire SQUID loop (thermal hysteresis) [14,7] or the phase slippage of the superconductor order parameter in the structure, as reported by Troeman *et al* [15]. To overcome this

difficulty, a normal-metal thin film acting as a shunt resistor is deposited onto the Nb film [16,17].

Critical Current Measurement:

The use of standard SQUID electronics or lock-in amplifier to read out the SQUID is unable due to its hysteretic I-V characteristics. Therefore, the simplest method to measure the switching current of the SQUID was developed by Benoit *et al.* [18,19].
The field dependence maximal supercurrent (switching or critical current) I_c predicts overall flux modulation of the SQUID is followed by

$$I_c = \sqrt{(I_{c1} - I_{c2})^2 + 4 I_{c1} I_{c2} \cos^2(\pi \Phi_e / \Phi_0)} \qquad (4.16)$$

Here, I_{c1} and I_{c2} are the critical currents of each Josephson junction. I_C is considered as upper experimental value of switching current by neglecting effects caused due to temperature, electronic noise, quantum effects etc. The field modulation depths are maximal as I_{c1} and I_{c2} of device are comparable.

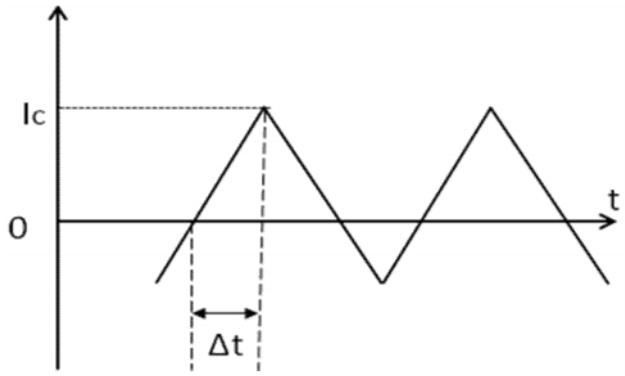

Fig.4.12 Schematic representation of critical current measurement by time difference between zero current and switching current at constant current sweep is shown.

Unfortunately it is not possible to neglect the effect of temperature on the value of critical current. As reported in chapter 1, the SQUID in the superconducting state is in a well potential. The height of the barrier is related to the bias current and goes to zero for $I = I_{C0}$ resulting on $V \neq 0$. The thermal fluctuations induce the $V \neq 0$ state at the current value lower than I_{C0}; to study the effect of thermal fluctuations by means of critical current fluctuations, there are two different ways:

One method consists of applying a fixed bias current $I < I_c$ to the SQUID and measuring the time between the application of the current and the appearance of a voltage across the junction [20,21].

In the other method, historically used at the ICIB-CNR laboratories, the bias current applied to the junction is ramped up at a constant rate dI/dt, and the current I at which the SQUID switches from the zero-voltage to a finite voltage state is recorded [18]. The switching current is determined by measuring the time between the zero crossings of the bias current ramped up at a constant rate and the switching of the SQUID to the finite voltage state as shown in following fig. 4.12.

Standard Fly Time Technique:

The standard scheme used for switching current measurement as function of time described above is generally known as fly time technique which is represented in fig.4.13.

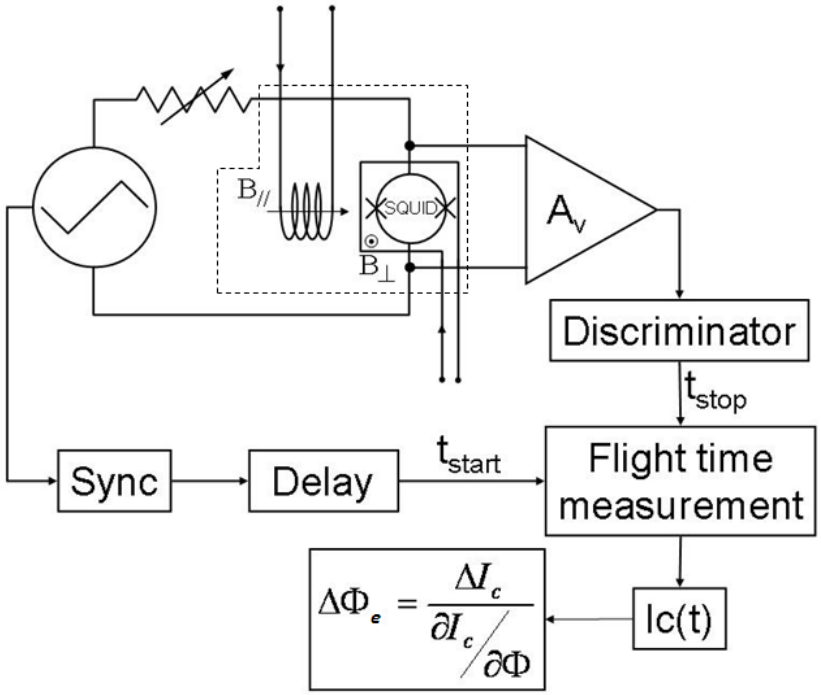

Fig. 4.13 Experimental set up for the switching current measurements based on a time of flight technique. The resolution of the critical current measurements is about 1 part in 10^4. The dashed box indicates the cold area shown in fig.4.15 (T = 4.2 K).

The SQUID is current biased with a linear slope at 100Hz starting from zero. The synchronism of the ramp generator is sent to start the internal clock of a time acquisition board having a time resolution of 12.5 ns. The SQUID voltage is amplified and sent to a discriminator that provides the stop signal at the time of the switching out of the zero voltage state. The critical current values are obtained multiplying the current ramp slope dI/dt (measured after each measurement run) with the interval time Δt measured by the time acquisition board.

The discriminator serves also to stop the ramp generator to set the current to zero (in order to reduce heating) and after a short delay to start a new ramp for next acquisition. The estimated measurement resolution of the critical current is about 1 part in 10^4, which is essentially limited by the stability of the synchronism signal and of the measurement of the current slope.

Switching Current Probability Distribution $\mathrm{P(I)}$:

The process of the escape from the superconductive state is a stochastic process and it has a well established theory in thermal and quantum regime. The escape probability as function of bias current $\mathrm{P(I)}$ at 4.2 K is shown in fig. 4.14. Starting from the probability curve, it is possible to define a mean value and a standard deviation sigma (σ).

The switching current from the voltage state to the zero voltage state occurs randomly following a certain distribution $P(I)$, related to escape rate $\Gamma(I,T)$ by the following relation [5,22]:

$$P(I) = \Gamma(I)\left(\frac{dI'}{dt}\right)^{-1} \exp\left[-\int_{I_0}^{I(t)} \Gamma(I')\left(\frac{dI'}{dt}\right)^{-1} dI'\right] \qquad (4.18)$$

The $P(I)$ is related to escape rates Γ and sweeping rate of bias current i.e. dI/dt. The fluctuation in critical current can be acquired accurately using low sweep rate as well as low temperature [2-4].

The switching current probability distribution $P(I)$ can be obtained by accumulating a large number of switching currents I and a histogram generated from SQUID having one micron loop size is shown in fig.4.14

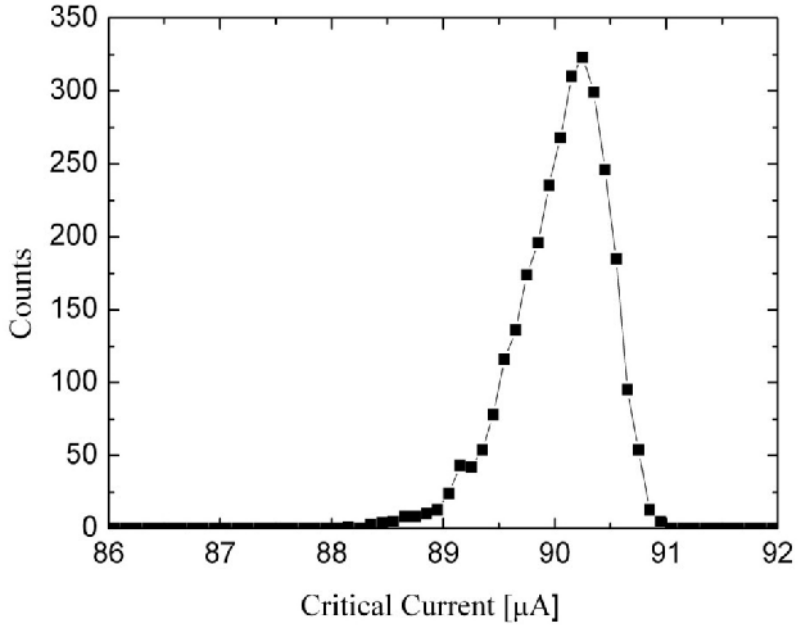

Fig.4.14 Critical current switching distribution as a function of the bias current of a hysteretic nanoSQUID measured at T=4.2K. A σ value of about 0.4 μA can be evaluated.

In these measurements, the $P(I)$ curve is obtained by recording 10000 switching events using standard fly time technique as described earlier. Starting from the probability curve, it is possible to define the mean value I_{CM} and the standard deviation sigma (σ). When performing a single critical current measurement, an "arbitrary" value is extracted from the probability curve and the error is of the order of σ.

Responsivity: Current- Magnetic Flux Characteristics:

The most important property of hysteretic SQUID is the modulation of the critical current as a function of the magnetic flux concatenated to the SQUID loop. The critical current modulation allows determining the responsivity of the SQUID, defined as the variation of the critical current as a function of the external magnetic flux variation $\partial I_C / \partial \Phi$. After the imposed number of switching events recorded, a new magnetic field is set to adjust the current flowing in the integrated coil or in the solenoid.

When performing a single critical current measurement an "arbitrary" value is extracted from the probability curve and the error is of the order of σ. When performing more

enough measurements, we exclude the P (I) curve and it is possible to define a mean value and a standard deviation sigma (σ). Thus a single value of critical current in presence of particular magnetic field or magnetic flux is the mean value of all counts which gives added accuracy in the experimental data.

In these measurements, we have used two coils located near to SQUID device as shown in fig.4.15 and whole assembly was kept in cryogenic Dewar to perform measurement at 4.2K as represented by dotted box in fly time measurement scheme in fig. 4.13.

The integrated superconducting excitation coil fabricated very close to SQUID loop (as shown in central part around loop in fig.4.15) is generating the magnetic field perpendicular to SQUID in order to tune, modulate SQUID to high respositivity. Another external solenoid copper coil around the SQUID is generating the magnetic field parallel to SQUID plane as schematically shown in fig.4.15.

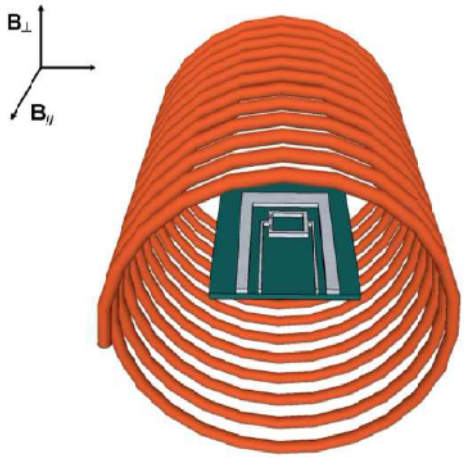

Fig.4.15 The sketch of the chip having SQUID with integrated coil which is inserted in the external solenoid which provides the magnetic field in the same plane of the SQUID loop.

When the magnetic field is applied along the SQUID plane using the solenoid, the mean critical current changes in a random way within the experimental error which indicates that the magnetic flux through SQUID loop remains zero, though the dayem bridge based SQUIDS are insensitive to magnetic field parallel to SQUID loop.

The typical magnetic pattern is reported in fig.4.16 for SQUIDs having a loop side of 1 (blue color), 2 (red color) microns. The integrated superconducting coil supports about 20 mA dc current and generates the magnetic field orthogonal to the SQUID loop plane to obtain current-flux modulation pattern fig.4.16

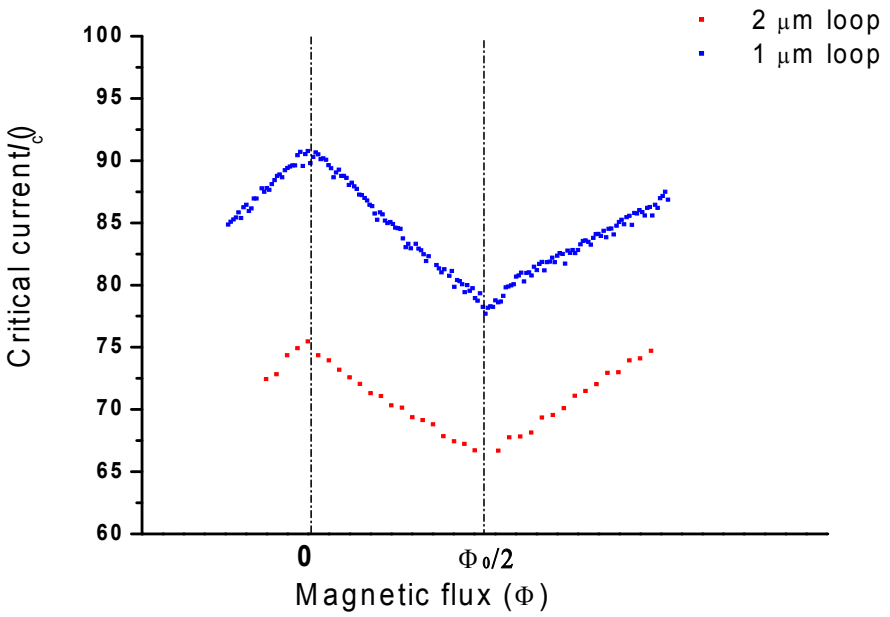

Fig. 4.16 Critical current as a function of external magnetic field threading the sensor loop of 1 micron (blue dots) and 2 micron (red dots) respectively. The magnetic field has been provided by integrated coil around the sensor. The critical current values have been obtained by a single switching measurement.

Due to the magnetic flux quantization in superconducting loop, the pattern results periodic and the period is the quantum flux Φ_0 ($\Phi_0=h/2e=2.07\text{x}10^{-15}$ Wb) and the magnetic field required to couple a flux quantum in the SQUID is inversely proportional to the loop area. The maximum magnetic flux coupled to the 2 and 1 micron loop size are about 4 and 1 Φ_0 respectively whereas for the 0.75 micron loop it is less than $\Phi_0/2$, as consequence it is not possible to determine the magnetic flux concatenate into the loop. In order to use loop size smaller than 1 micron a complex fabrication process should be adopted and the integrated coils should be fabricated in an additional step using standard optical lithography. These single switching measurements have been used to evaluate the intrinsic magnetic flux resolution of the sensor as given by

$$\Delta\Phi = \frac{\sigma}{2\dfrac{\partial I_C}{\partial\Phi}} \qquad (4.19)$$

The experimental results obtained by using current responsivity value of 30 $\mu A / \Phi_0$ are presented in fig.4.16. It is possible to evaluate an *intrinsic magnetic flux resolution as 0.01 Φ_0.*

All magnetic patterns reported in fig.4.16 are obtained by a single measure of the critical current, resulting in an apparent noise curve due to the thermal fluctuations. The error on each point is of order σ which is about 0.4 μA

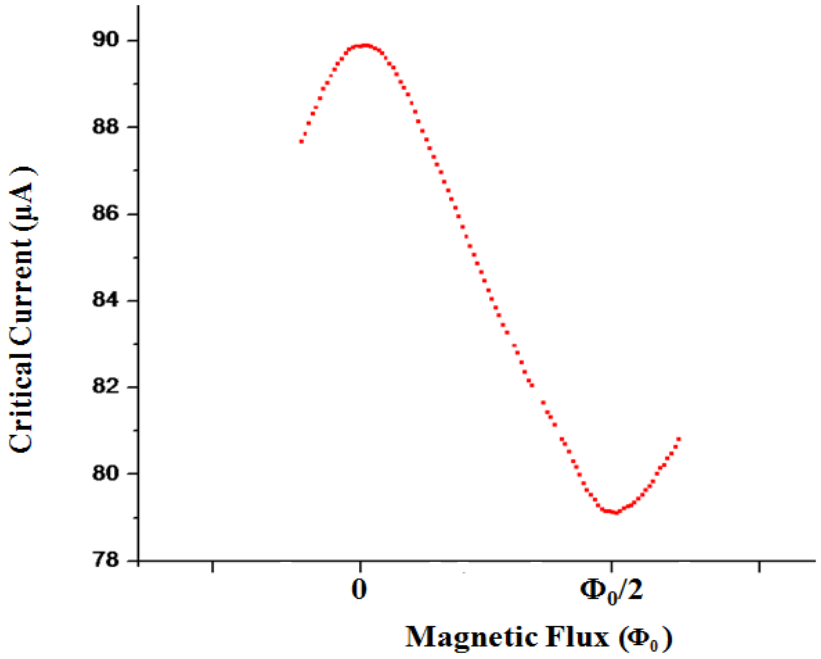

Fig.4.17 Critical current as a function of external magnetic field threading the sensor loop relative to the nanoSQUIDs having an area of 4 μm^2 obtained by P(I) measurements.

Each data point for the pattern of 1 micron SQUID loop reported in the fig.4.17 are obtained by measuring the P(I) curve with 10^4 independent measurements of critical current and plotting only the mean critical current resulting in a much more accurate curve.

We can estimate the total change in flux with respect to change in critical current by knowing the rate of change of flux to critical current is given by (eq. 4.17)

$$\Delta\Phi_e = \frac{\Delta I_C}{\partial I_C / \partial \Phi} \qquad (4.17)$$

The magnetic pattern allows determining the responsivity of the SQUID, defined as the variation of the critical current as function of the external magnetic flux variation $\partial I_C / \partial \Phi$; a resolution of about $0.3 m\Phi_0$ in the highest responsivity point is obtain.

The experimental values such as critical current modulation, critical current and calculated resistance obtained from SQUID devices having 1, 2 and 0.75 micron loop diameters are tabulated as follows:

SQUID loop size (μm)	Critical current values (μA)	Resistance calculated (Ω)	Critical Current modulation range
2	76	61	10-11%
1	90	45	14-15%
0.75	10.8	34	More than 40 % (Pattern upto 2V and quench at 1.4V coil)

Hence the modulation of fabricated and usable SQUIDs ranges from 10 to 20%. Applying the one-dimensional micro-SQUID model [14], we obtain a value of about 10 for the ratio l / ξ (l is the nanobridge length and ξ is the coherence length of niobium film which could not exceed the film thickness of 20nm) which is in fair agreement with our design.

4.5. Preliminary Magnetic Nanoparticle Magnetization Measurements:

Due to its reproducibility and simple fabrication, hysteretic SQUIDs are significant and greatly demanded for practical applications. Our main intention is employment of hysteretic SQUID for nanoparticles magnetization measurements. We have employed hysteretic nanoSQUIDs for preliminary iron oxide nanoparticle magnetization measurements. The detailed scheme and measurements explained in subsequent section is confirming its successful employment.

The dayem bridge based SQUIDs are insensitive to magnetic field parallel to SQUID plane. This basic principle is used during nanoparticle magnetization measurements.

To test the capability of our devices towards magnetization of iron oxide nanoparticles, we have deposited iron oxide nanoparticles by drop coast of a diluted solution on chips

containing characterized sensors. The scanning electron microscopic (SEM) image of iron oxide nanoparticle having average diameters around 15-16 nm is shown in fig. 4.18(b). When the solution gets dry, the nanoparticles stick on the chip due to the van-der Waals forces. Using SEM, it is possible to identify the suitable particle–sensor configurations. Generally in order to improve the location accuracy of the nanoparticles, an atomic force microscope and a scanning tunnel microscope (STM) tip can be used. There are many techniques available to deposit nanoparticles very close or perfectly inside the nanoSQUID loop [23,24].

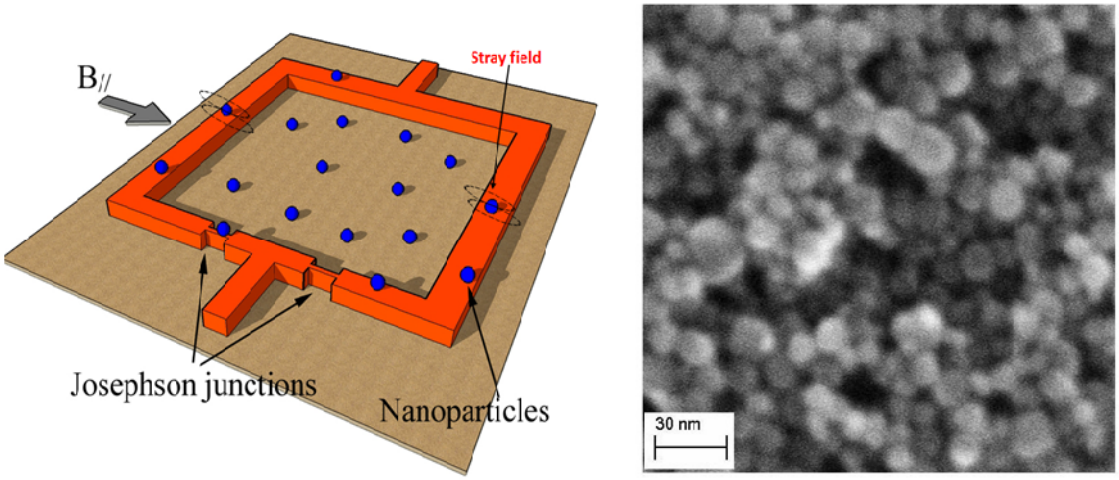

Fig.4.18 (a) Sketch of the nanoparticles placement inside the SQUID loop. The external field is applied parallel to the SQUID loop. Thus the SQUID is only sensitive to the flux induced by the stray field of the sample's magnetization. (b) Scanning Microscopic image of iron oxide nanoparticles having 15-16 nm average diameter.

The known responsivity of particular device can transfer the change in critical current into flux change as described in earlier section. In absence of iron oxide particle, change in magnetic field parallel to SQUID plane does not change critical current of SQUID. It indicates that the change in parallel magnetic field will not contribute to the flux change into the SQUID. On the other hand, in presence of nanoparticle, change in critical current is obtained with parallel magnetic field variation. Hence the critical current modification with respect to parallel field applied in SQUID plane occurs only due to stray field associated with nanoparticles as shown schematically in fig.4.18 (a). Thus, the magnetic flux in the loop is originated by the magnetization of magnetic nanoparticles and it is possible to convert the magnetic flux variation to magnetization by knowing the coupling factor of SQUID and sample.

Iron Oxide Nanoparticle Magnetization Measurements:

Herein we have reported the measurement performed of iron oxide nanoparticles with the device having 1-micron loop. The presence of iron nanoparticles did not change appreciably the magnetic pattern obtained using the integrated coil (magnetic field normal to the SQUID plane), however the presence of nanoparticle was evident by the critical current measurement performed with magnetic field generated using the external solenoid (magnetic field parallel to the SQUID plane). In this case the SQUID critical current showed a variation well above the experimental error.

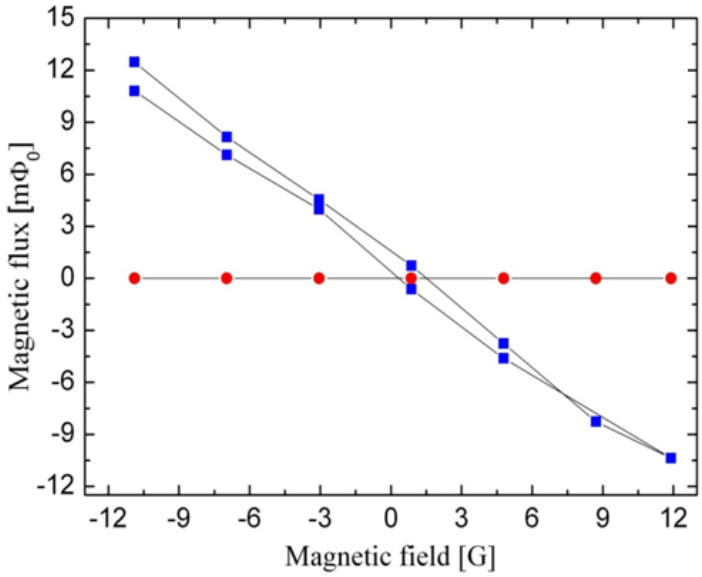

Fig.4.19 Magnetic flux (SQUID output) as a function of the external magnetic field applied in the plane of the SQUID with (blue square) and without (red circle) iron oxide nanoparticles. The presence of magnetic nanoparticles induces a variation of the magnetic flux coupled to squid loop that can be effectively detected.

The experimental results are illustrated in fig.4.19. In absence of iron oxide nanoparticle, when the magnetic field is applied along the SQUID plane using the solenoid, as expected the mean critical current changes in a random way within the experimental error (about 10nA) indicating that the magnetic flux through to SQUID loop remains zero. This result is shown in fig. 4.19 by the red dot.

Using the measured responsivity for this particular device ($27\,\mu A/\Phi_0$) the critical current variation was converted to magnetic flux variation and plotted as blue square in fig.4.19. Of course the magnetic flux in the loop is originated by the magnetization of iron oxide nanoparticles and it is possible to convert the magnetic flux to magnetization

if the coupling factor is known or using a procedure similar to the one used by Volkov et al [25].

It is very important to take into account that there are two different starting points of measurements; one can either start with zero magnetic field or fix magnetic field where particles are already magnetized. There is noticeable difference in both the measurements due to stimulated nanoparticle magnetization. The measurements exposed above are performed in presence of constant magnetic field starting from a magnetic field of -11G, reaching 12G and coming back to -11G which was the maximum fields obtainable using our copper solenoid.

The data points are the average of 10^4 measurements of the critical current via standard time of flight techniques and the small hysteresis present in the curve is probably due to relaxation as shown in the fig. 4.20.

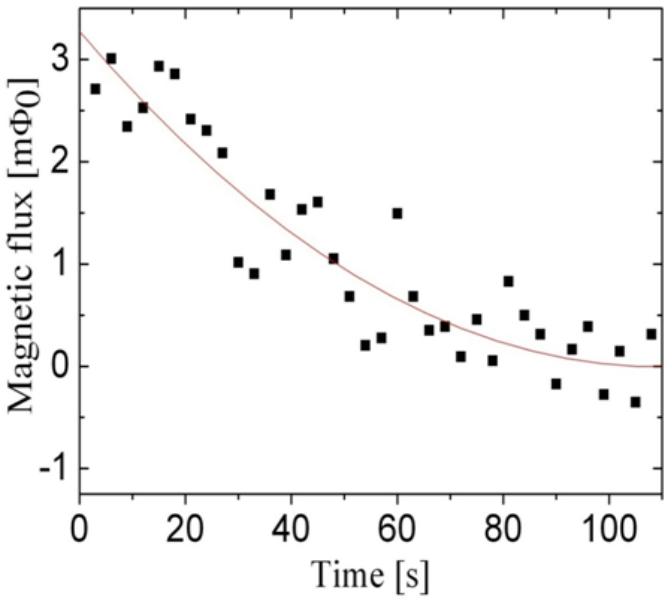

Fig.4.20 The figure shows the time dependence of the magnetic flux (SQUID output) after switching off the external magnetic field in presence of the iron oxide nanoparticles located on the chip. As expected it is possible to observe a magnetic relaxation which is completed in about 100 s.

It is worth to note that with the present electronic at 100Hz to acquire 10^4 measurements it takes about 100s. This time is comparable with that needed to reach equilibrium as shown in fig.4.19. Each point in the fig.4.20 is the results of the average of 300 measurements acquired after having switched off the magnetic field from -11G. Due to the low data averaging, the data seem noisy; however the behavior of a typical

magnetization relaxation can be observed with time duration in agreement with prior experiments on similar nanoparticles [25].

There are two instant improvements required: first a faster electronic is needed to perform even more accurate measurements and second, to better investigate the relaxation phenomenon, a superconducting coil is needed to perform measurements at higher magnetic field without inducing thermal instability.

References:

1. B. Ruggiero, C. Granata, V. G. Palmieri, A. Esposito, M. Russo and P. Silvestrini, Phy. Rev.-B, Vol. 57- 1(1998)
2. C. Granata, A. Vettoliere, R. Russo, E. Esposito, M. Russo, and B. Ruggiero, Appl. Phys. Lett. 94, 062503 (2009)
3. B. Ruggiero, C. Granata, E. Esposito, V. G. Palmieri, M G Castellano C Cosmelli, M. Russo and P. Silvestrini, IEEE Trans. App. Supercond. Vol. 9-2 (1999)
4. P. Silvestrini, V.G. Palmieri, B. Ruggiero and M. Russo, Phy. Rev. Lett. Vol. 79-16 (1997)
5. Teshe C D and Clarke J, *J. Low Temp. Phys.* 27 301 (1977)
6. Drung D., NATO ASI (1996) Clarke J., NATO ASI, F59 (1989)
7. Hasselbach K, Mailly D and Kirtley J R, *J. Appl. Phys.* 91 4432 (2002)
8. Drung D and Muck M "*The SQUID Handbook* vol I*: Fundamentals and Technology of SQUIDs and SQUID Systems"* ed J Clarke and A I Braginski (Weinheim: Wiley–VCH) p 127 (2004)
9. Fagaly R K, *Rev. Sci. Instrum.* 77 101101 (2006)
10. L. Hao, J. C. Macfarlane, J.C. Gallop, D. Cox, J. Beyer, D. Drung, and T. Schurig, Appl. Phys. Lett., 92, 192507 (2008)
11. Koch R H, Di Vincenzo D P and Clarke J, *Phys. Rev. Lett.* 98 267003 (2007)
12. Voss R F, Laibowitz R B and Broers A N, *Appl. Phys. Lett.*37 656 (1980)
13. Voss R F, Laibowitz R B, Ketchen M B and Broers A N "*Superconducting Quantum Interference Devices and theirApplication"* ed H D Hahlbohm and H Luebbig (New York: de Gruyter) p 365 (1980)
14. Podd G J, Hutchinson G D, Williams D A and Hasko D G, *Phys. Rev.* B 75 134501 (2007)
15. Troeman A G P, van der Ploeg S H W, Il'Ichev E, Meyer H-G, Golubov A A, Kupriyanov M Y and Hilgenkamp H, *Phys. Rev.* B 77 024509 (2008)
16. Lam S K H, *Supercond. Sci. Technol.* 19 963 (2006)
17. Lam S K H and Tilbrook D L, *Appl. Phys. Lett.* 82 1078 (2003)
18. Mailly D, Chapelier C and Benoit A *Phys. Rev. Lett.*70, pg.2020 (1993)

19. Chapelier C, El Khatib M, Perrier P, Benoit A and Mailly D, SQUID 91 *Superconducting Devices and Their Applications* ed H Koch and H Lbbig (Berlin: Springer) p 286 (1991)
20. Devoret M.H., Martinis J.M., Esteve D., Clarke J., Phys. Rev. Lett. 53, 1260 (1984)
21. Han S., Yu Y., Chu X., Wang C. S. and Z., Science 283, 1457(2001)
22. F. C. Wellstood, C. Urbina and J. Clarke, *Appl. Phys. Lett. 54, 2599 (1989)*
23. Lam S K H, YangW, Wiogo H T R and Foley C P Nanotechnology 19 285303(2008)
24. Faucher M, Jubert P O, Fruchart O, Wernsdorfer W and Bouchiat V, Superc. Sci. Technol.,22: 064010 (2009)
25. Volkov I, Chukharin M, Snigirev O et al, J. Nanopart. Res. 10:487-497 (2008)

Conclusions

In this work, I have reported the design, the fabrication and the performance of an integrated magnetic nano-sensor based on niobium dc-SQUID (**S**uperconducting **QU**antum **I**nterference **D**evice) for measurements of small local magnetic signals arising from small atomic or molecular populations. Both hysteretic and non-hysteretic devices are presented, in which the integrated modulation and calibration coils allow a more accurate sensor characterization and an easier tuning and employment. The superconducting loop has a washer shape in order to enhance the heat dissipation during the working operations.

The non-hysteretic device is obtained by shunting the niobium layer by means of Al layer. The device consists of the side length of the square detection area (washer hole) is 200nm while the length and width of the nano-bridge are 100nm and 80nm respectively. The intrinsic responsivity of the sensor is so high ($1\,mV/\Phi_0$) that it is possible to use simple readout electronics without appreciable noise degradation. Due to a wide linear region in the $V-\Phi$ characteristics, the sensors showed an open-loop linear dynamic range as high as $10^4\,Hz^{-1/2}$. A magnetic flux noise level as low as $1.5\,\mu_0\,Hz^{-1/2}$ is obtained, corresponding to a spin noise of 60 spin $Hz^{-1/2}$ better than the values reported for devices with a comparable size. Based on this estimation, the application of such a device for the detection of small magnetic clusters would be an attractive option.

In view of the nano-SQUID employments in the detection of small spin populations, we have calculated the spin sensitivity and the magnetic response relative to the single spin, as a function of its position within the SQUID hole. The results show that the SQUID response depends strongly on the spin position. Due to the recent successful efforts devoted to finely arrange the nano-particles within the sensor loop, the information provided here is very useful to optimize the sensor performance in view of most nano-magnetism applications.

We have successfully employed the hysteretic nanoSQUID for magnetization measurement of iron oxide nanoparticles. The device is fabricated using a single 20nm thick niobium layer and is shaped by lift-off. The SQUIDs were designed to have a hysteretic current-voltage characteristic and therefore they are employed as a magnetic flux-current transducer. A current-magnetic flux transfer coefficient (responsivity) of $30\,\mu A/\Phi_0$ and an intrinsic magnetic flux resolution less than $1\,m\Phi_0$ have been obtained. The performed measurements with iron oxide nanoparticles on one micron SQUID loop show that the presence of magnetic nanoparticles can be easily detected and the magnetic relaxation curve measured is indicating that the sensor can be effectively used in nano-magnetism applications.

List of Publications

Thesis Publications

C. Granata, A. Vettoliere, **P. Walke**, C. Nappi and M. Russo, "Performance of nano-Superconducting quantum interference devices for small spin cluster detection*"* ; *Journal of Applied Physics*-**106**, 023925(2009) Also selectively published in *Virtual Journal of Application of Superconductivity* Vol.**17**, Iss.3 (1st Aug.09)

C. Granata, A. Vettoliere, **P. Walke,** E. Esposito, C. Nappi, P. Silvestrini, B. Ruggiero, and M. Russo, "NANO-SQUIDs BASED ON NIOBIUM DAYEM BRIDGES FOR NANOSCALE APPLICATIONS"; *J. Phys.: Conf. Ser*. 234 042010 (2010)

A.Vettoliere, C. Granata, E. Esposito, **P. Walke**, B. Ruggiero and M. Russo*, "*SQUIDs sensors for high spatial resolution magnetic imaging and nanoscale application*" Springer Book - Sensors and Microsystems, AISEM 2009 Proceedings***,*** Vol. **54.** Springer Publ. (2010) (ISBN: 978-90-481-3605-6)

R. Russo, **P. Walke,** C.Granata, A. Vettoliere, E. Esposito and M. Russo, "SQUID based magnetic sensor for detection of magnetic nanoparticles"; *Journal of Nanoparticle Research*. (Submitted Manuscript-2010)

Other Publications

Bhaskar R. Sathe, **Pravin S. Walke**, Imtiaz S. Mulla, Vijayamohanan K. Pilla*, "*Effect of Fe3O4 on Morphology of Fe-SnO2 Hyperbranched Heterostructures*"; Chemical Physics Letters*, volume **493**, Issue 1-3 (2010) pages 121-125.

Bhaskar R. Sathe, Mrudula Patil, **Pravin S. Walke**, J. P. Vivek, Ashish Lele, Vijayamohanan K. Pillai. I. S. Mulla*,*"Synthesis of Sb-doped SnO2 Nanowires and Hyperbranched Structures"; *Sci. Adv. Mater***.** 1, 38–43, 2009

Mukta V. Vaishampayan, Rupali G. Deshmukh, **Pravin Walke** and I.S. Mulla, *"*Fe-doped SnO2 nanomaterial: A low temperature hydrogen sulfide gas sensor" *Materials Chemistry and Physics***,** Volume **109**, Issues 2-3, (2008) *Pages 230-234*

Ashok Bhise, Dattatray Late, **Pravin Walke**, Mahendra More, Imtiaz Mulla, Vijayamohanan Kunjukrishna Pillai and Dilip S Joag "A single In-doped SnO2 submicron size wire as a field emitter" *J. Phys. D: Appl. Phys*. **40** (2007) 1

Ashok B. Bhise, Dattatray J. Late, **Pravin S. Walke**, Mahendra A. More, Vijayamohanan K. Pillai, Imtiaz S. Mulla, Dilip S. Joag* , "Sb-doped SnO2 wire: highly stable field emitter"; *Journal of crystal growth* **307** (2007) 87–91

Abbreviations

Abbreviation	Expansion
Al	Aluminum
AFM	Atomic Force Microscope
BCS	Bardeen, Cooper, and Schrieffer
CNT-SQUID	Carbon Nanotube Superconducting Quantum interference Devices
CAD	Computer-Aided Design
CPR	Current Phase Relationship
dc-SQUID	Direct current Superconducting Quantum interference Devices
EBL	Electron Beam Lithography
FIB	Focus Ion Beam Lithography
IPA	Isopropyl Alcohol
LASI	LAyout System for Individuals
MIBK	Methyl Isobutyl Icetone
Nano-SQUID	Nanoscale Superconducting Quantum interference Devices
Nb	Niobium
N-I-S	Normal Metal-Insulator-Superconductor
NMR	Nuclear Magnetic Resonance
PMMA	Polymethyl Methacrylate
RCSJ	Resistively Capacitatively Shunted Junction
RIE	Reactive Ion Etching
S1-I-S2	Superconductor 1-Normal Metal-superconductor2
S-S'-S	Superconductor-Superconducting link-Superconductor
S-I-S	Superconductor-Normal Metal-superconductor
SEM	Scanning Electron Microscopy
Si	Silicon
SPD	Single Photon Detector

SQUID	Superconducting Quantum Interference Device
SQUIPT	Superconducting Quantum Interference Proximity Transistor
SSM	Scanning SQUID Microscopy
STM	Scanning Tunneling Microscopy
UV	Ultraviolet, electromagnetic waves with a wavelength between 3 nm and 400 nm
W	Tungsten